A Mechanistic Understanding of the Postantibiotic Effect and Treatment Strategies

by

Jaydeep K. Srimani

Department of Biomedical Engineering
Duke University

Date:_____
Approved:

_____
Lingchong You, Supervisor

_____
Charles Gersbach

_____
Brenton Hoffman

_____
Katia Koelle

_____
John Neu

Dissertation submitted in partial fulfillment of
the requirements for the degree of Doctor
of Philosophy in the Department of
Biomedical Engineering in the Graduate School
of Duke University

2017

ABSTRACT

A Mechanistic Understanding of the Postantibiotic Effect and Treatment Strategies

by

Jaydeep K. Srimani

Department of Biomedical Engineering
Duke University

Date:_____
Approved:

_____
Lingchong You, Supervisor

_____
Charles Gersbach

_____
Brenton Hoffman

_____
Katia Koelle

_____
John Neu

An abstract of a dissertation submitted in partial
fulfillment of the requirements for the degree
of Doctor of Philosophy in the Department of
Biomedical Engineering in the Graduate School of
Duke University

2017

Copyright by
Jaydeep K. Srimani
2017

Abstract

Although antibiotics have proven to be one of the great achievements of modern medicine, their efficacy has dramatically decreased over the past several decades. This is due, in part, to the rapid pace of natural bacterial evolution, but also to the overuse and misuse of antibiotics in general. This often selects for drug-resistant pathogens, and allows them to flourish in the face of antibiotic treatment. In addition to the emergence of genetic resistance, bacteria often utilize a number of population-level behaviors to survive antibiotic treatment. This is referred to as collective antibiotic tolerance (CAT). Taken together, antibiotic resistance and tolerance have led to the re-emergence of infectious diseases throughout the world. In general, there are two strategies to combat this risk: develop novel antibiotics, and/or use existing drugs more effectively, so as to minimize the chance of resistance emergence. Novel drug development is a time- and resource-intensive process, and pharmaceutical companies are not financially incentivized to develop these types of drugs. Therefore, it is of increasing importance to understand the population dynamics underlying various bacterial survival mechanisms, and exploit this knowledge to design better antibiotic treatment protocols.

My dissertation research focuses on a prevalent phenomenon called the postantibiotic effect (PAE), which refers to the transient suppression of bacterial growth

following antibiotic treatment. Although PAE has been empirically observed in a wide variety of antibiotics and microbial species, heretofore there has not been a definitive mechanistic explanation for this pervasive observation.

In this work, I use a combination of high-throughput microfluidic experiments and computational modeling to examine the relationship between dosing parameters and the degree of bacterial inhibition, quantified by population recovery time. I found that recovery time is a function of total antibiotic, regardless of how the dose profile. Moreover, a minimal model of transport and binding kinetics was sufficient to recapture this trend, suggesting a unifying explanation for historical observations of PAE in a variety of contexts. I validated this modeling using both *in silico* and *in vitro* perturbation studies.

Moreover, I showed that efflux inhibition, a common strategy in antibiotic treatment, is effective in certain dynamic-dependent situations. This work puts forth a possible mechanism for PAE, which could serve as a clinical aid in selecting effective antibiotic/adjuvant combinations, as well as in designing periodic antibiotic treatments.

Dedication

To my family, particularly my parents, for their love and support since the very beginning.

Contents

Abstract iv

List of Tables xi

List of Figures xii

Acknowledgements xxii

1. Introduction 1

1.1 Antibiotics and resistance: a brief history 1

1.2 Mechanisms of antibiotic resistance 4

1.3 Phenotypic persistence 7

1.4 Population-level behaviors 7

1.4.1 Antibiotic-mediated altruistic death 8

1.4.2 Quorum sensing (QS) and biofilm formation 11

1.4.3 Bistable inhibition of the replication machinery 12

1.4.4 Mixed strategies 14

1.4.5 Social Interactions 16

1.4.6 Density dependent survival leads to faster recovery from antibiotic treatment 18

1.5 Implications for antimicrobial treatment strategies 19

1.5.1 Timing in antibiotic dosing 20

1.5.2 Molecular interventions to disrupt CAT 21

1.5.3 Treatment considerations 26

1.6 Mathematical modeling in systems biology 29

1.7 Microfluidic approaches to antibiotic resistance 32

1.8 Conclusions 34

1.9 Acknowledgements 35

2. Introduction 36

2.1 Postantibiotic effect (PAE): definition and prevalence 36

2.2 Premise 39

2.3 Results 40

2.3.1 A microfluidic platform for high throughput quantification of PAE 40

2.3.2. Quantification of PAE in E. coli cells in response to streptomycin treatment. 42

2.3.3 Partial population death and phenotypic selection do not account for PAE ... 44

2.3.4 A minimal model of antibiotic action 49

2.3.5 Model validation: perturbation studies 55

2.3.6 Efficacy of efflux inhibition to diverse antibiotic mechanisms of action 60

2.3.6.1 Computational modeling approaches 62

2.3.6.2 Experimental validation 67

2.4 Discussion 70

2.5 Conclusions 71

3. Linear population allocation by bistable switches in response to transient stimulation 73

3.1 Bistability 73

3.2 Decision making in biological systems 75

3.3 Premise 79

3.4 Results 81
3.4.1 A positive feedback circuit 81
3.4.1.1 Model development 86
3.4.1.2 Deriving and analytical solution for activation probability 89
3.4.2 A toggle switch model 93
3.4.2.1 Model development 95
3.4.3 A bistable Myc-Rb-E2F model 96
3.4.3.1 Model development 98
3.4.5 Initial lag in the toggle-switch and Myc-Rb-E2F models 100
3.4.6 Advantages of linear activation 101
3.4.7. Discussion 106
3.4.8 Materials and methods 108
3.4.8.1 Noise implementation and stochastic simulation algorithm (SSA) 108
3.4.8.2 Linear advantage simulations 109
3.5 Conclusions 110
3.6 Acknowledgements 110
4. Postantibiotic effect: implications for treatment design 111
4.1 Introduction 111
4.2 Premise 112
4.3 Results 113
4.4 Future directions 115
References 118

Biography 137

List of Tables

Table 1: Full ODE model parameter values 52

Table 2: Simplified ODE model parameters..... 64

Table 3: Parameter values for a mutual inhibition toggle switch 96

List of Figures

Figure 1: Left panel shows a timeline of antibiotic development and subsequent emergence of resistance. The placement of antibiotics above the timeline corresponds to the year each was deployed, while the placement below the time corresponds to the year resistance was first observed. Here, it is important to note that observation of resistance does not necessarily imply loss of all clinical utility. Right panel shows the frequency of antibiotic prescriptions (per 1000 people) on a state by state basis. Figure reproduced with permission from[11]. 2

Figure 2: Antibiotic tolerance mechanisms and collective antibiotic tolerance (CAT). A. Bacteria can survive antibiotic treatment through a variety of mechanisms, either on the individual or population level. Often, multiple mechanisms are at play. B. Collective antibiotic tolerance (CAT) is defined as a population density-dependence at intermediate antibiotic concentrations. For example, at low concentrations, populations are able to withstand treatment regardless of density. Conversely, at high antibiotic concentrations, populations are inhibited regardless of density. However, at intermediate concentrations, population fate depends on initial density. C. CAT is characterized by a transition in population fate as a function of initial density. 5

Figure 3: Diagrammatic description of various CAT mechanisms. A. In PAD populations, cells produce a beneficial molecule e.g. a drug-degrading enzyme, often termed public good, intracellularly. In response to antibiotic stress, a fraction of cells lyse, releasing the intracellular public good to the global environment, where surviving cells benefit (hence "altruistic). B. QS populations synthesize a signaling molecule, often an N-acyl homoserine lactone (AHL), that is secreted to the global environment. These signaling molecules diffuse into local cells and act as a proxy for local cell density. When the local signal concentration exceeds a critical threshold, downstream gene expression (e.g. production of an antibiotic-degrading enzyme) leads to population survival. C. Antibiotics diffuse into individual cells, where they inhibit ribosome function and protein synthesis. At sufficiently high population densities, the intracellular antibiotic concentration is sub-inhibitory, leading to population survival. D. These mechanisms often act in parallel to enable antibiotic tolerance. E. Moreover, the metabolic burden of gene/protein expression is often shared in multi-species consortia. This can lead to social interactions, e.g. mutualism, commensalism, and others. 9

Figure 4: CAT, compared to persistence or genetic mutation, enables rapid population recovery. A. The mechanism by which bacteria survive antibiotic treatment can significantly influence the speed of their recovery. Here, previously published models

are used to compare the recoveries of populations dependent on different forms of CAT or persistence[24,25,76,77]. The three CAT populations (QS, ribosome inhibition, and PCD) recover significantly faster than the persister-dependent population. B. The recovery times (defined as the time required for a population to double following treatment) decrease as the initial population density increases. Populations surviving by enzyme-dependent CAT actively degrade antibiotic; thus, the antibiotic concentration is quickly reduced to sub-inhibitory levels, enabling recovery. In the case of bistable ribosome inhibition, at high cell densities, the intracellular antibiotic concentration is insufficient to overcome the positive feedback in ribosome synthesis, again leading to rapid recovery. Conversely recovery via persisters requires a relatively long time period due to the dependence on the slow, intrinsic removal of the antibiotic and the low frequency of persister formation. 19

Figure 5: Treatment strategies to inhibit CAT. CAT mechanisms can be attenuated via a number of specific strategies; inhibiting the synthesis or function of antibiotic-degrading enzymes and/or signaling molecules (A-B), increasing ribosome inhibiton (C), or inhibiting specific mechanisms/interactions in consortia (D-E). 22

Figure 6: Mathematical representations of cellular networks. Mathematical models can be based on interactions alone (blue panel), constraints (purple panel), or mechanisms (green panel). Interaction-based models consist of various components (hubs) and their correlations (edges); constraint-based models consist of flux distributions calculated from reaction pathways; mechanism-based models track the time series evolution of components of interest. These three types of models fall on a continuum, progressively sacrificing scope/complexity in favor of detail/accuracy. Figure redrawn from[118]. 30

Figure 7: (Left panel) Recovery time is defined as the time required for a population (red line) to double in response to a transient antibiotic treatment (red shading). (Right panel) The postantibiotic effect (PAE) induced by an antibiotic treatment refers to the additional time required for a population to recover (red line) in comparison to the untreated control (black line). 39

Figure 8: A high throughput microfluidic platform for quantifying bacterial population dynamics. A. Each PDMS-fabricated chip consists of six independent experiments, one of which is shown, from top view (top row). Green circles indicate media inflow; red circle indicates outflow. Bacteria are manually loaded in inflow ports and are trapped in individual culturing chambers (gray circles), the height of which ensures that bacteria are imaged in a monolayer (second row schematic). Growth conditions (e.g. antibiotic dose profile) are precisely controlled via externally programmable syringe pumps. B.

Fluorescent images show representative growth of a monolayer of *E. coli* BW25113 cells constitutively expressing GFP over four hours. 41

Figure 9: Population recovery time is a function of total antibiotic. A. Representative time series fluorescence data showing dose-dependent population recovery in response to transient streptomycin treatment. Here, time zero is relative to the end of treatment (120 minutes). Trajectories show mean and standard deviation for five replicates; colors indicate increasing antibiotic concentration (2, 4, 6, 8, 10, 12 µg/mL). Population fluorescence values are normalized to time zero; dotted line indicates a 2-fold increase, corresponding to the recovery time for each population. B. Population recovery time is an exponentially increasing function of total antibiotic treatment. Inset shows recovery time as a function of dose duration for increasing streptomycin concentrations (as in panel C). When plotted against total antibiotic (calculated as $\int_0^{\tau_0} A(t)dt$), all recovery time values collapse onto a single exponential function (black line, $R^2 = 0.83$). 43

Figure 10: Partial population death does not account for antibiotic dependent recovery time. A. Concentration dependent streptomycin killing rates were determined in the absence of population growth. Overnight cultures were diluted 10-fold and grown in M9 media to a high density. Cells were then incubated in minimal media with the indicated antibiotic concentration for increasing durations. Population viability decreased exponentially with dose duration. The control population showed negligible growth/death in these conditions, indicating that decrease in viability is due to cell killing. All data points show mean and standard deviation of 6 replicates. B. Correcting for partial population death results in a lower effective recovery time (purple data points); however, recovery time remains dependent on total antibiotic. 46

Figure 11: Successive doubling times suggest no phenotypic selection. A. Successive doubling times are defined as the time intervals over which a population increases 2-fold, and can be calculated from individual recovery trajectories, relative to the end of the dose (red shading). Here, the nth doubling time is denoted RT_n. Thus, RT_1 is identical to the recovery time data presented in Figure 1D. The extent of RT_n is limited by the size of the growth environment and data acquisition. B. Convergence of RT_n suggests the presence or absence of antibiotic-dependent selection effects. In the absence of selection, RT_n would converge to zero slope, indicating that treatment history had no effect on growth dynamics after detoxification; after recovery from antibiotic treatment, populations were indistinguishable from untreated control (left panel). In the presence of antibiotic selection, successive RT_n would converge to slope greater than zero, indicating a physiological "memory effect", aka selection. C. – E. Successive doubling times following streptomycin (C) chloramphenicol (D), and streptomycin treatment in

0.05% w/v casamino acid media converge to a flat line, suggesting that the effect of antibiotic selection is insignificant. 47

Figure 12: The timescale of intracellular antibiotic efflux dictates individual and population recovery. A. A minimal model of antibiotic action. Antibiotic is transported between the intracellular and extracellular environments (A_{in} and A_{out}) by influx and efflux rates (k_{in} and k_{out}). A_{in} reversibly binds to target ribosomes C to form the complex CA, with binding and dissociation rates k_f and k_b, respectively. This complex can then be degraded through the intermediate CA'. These intracellular dynamics influence the overall population recovery rate; the maximum growth rate μ is dependent on the ribosome concentration C. Thus, recovery can be quantified both on the individual level, as a function of C, or on the population level, in terms of cell density. B. Concurrent antibiotic transport and ribosome inhibition dictate recovery dynamics. During treatment, $A_{out} >> A_{in}$, and the intracellular antibiotic concentration can be linearly approximated by $A_{in}(D) = k_{in}A_{out}D$, where A_{out} is assumed to be constant and D represents the treatment duration (leftmost schematic and panel 1). Antibiotic influx is greater than efflux; A_{in} binds to target ribosomes and strongly inhibits the upregulation of ribosome synthesis. When extracellular antibiotic is removed, A_{in} decreases (middle and rightmost schematics and blue shading and panels 2-3), and ribosome synthesis is dictated by positive feedback and efflux (panel 3). C. A_{in} accumulates linearly with treatment duration for sufficiently short treatment durations (panel i). After the removal of A_{out}, efflux and inhibition dynamics combine to delay the synthesis of ribosomes in a concentration-dependent manner (panel ii). Colors indicate increasing antibiotic concentration, as shown in panel ii. D. Antibiotic efflux timescale sets intracellular recovery RT_{cell}. Regardless of the antibiotic treatment history, the relationship between intracellelular antibiotic A_{in} and ribosome concentration C approaches the same asymptote, indicating that the timescale of individual detoxification sets the timescale of ribosome synthesis. Colors indicate increasing antibiotic concentration, as in Figure 2C-D; for these representative trajectories, treatment duration was set to 120 minutes. E. Population recovery time is dictated by total antibiotic delivered. Lower right inset shows that RTpop is an increasing function of dose duration; these data collapse onto a single relationship as a function of total antibiotic (main figure). Moreover, RT_{pop} and RT_{cell} are strongly correlated (upper left inset). 50

Figure 13: Recovery time remains a function of total antibiotic delivered, regardless of dose profile. Here, I simulated triangular (A) and exponentially decaying dose profiles

(B), over the same range of treatment conditions. Population recovery times collapsed reliably as a function of total antibiotic. 55

Figure 14: Key parameter perturbations confirm model validity. A. Modeling indicates that decreasing the ribosome degradation rate leads to shorter recovery times in response to equal amounts of total antibiotic. B. Modeling indicates that decreasing the antibiotic efflux rate leads to longer recovery times in response to equal amounts of total antibiotic. C. Modeling indicates that increasing the ribosome synthesis rate leads to shorter recovery times in response to equal amounts of total antibiotic. D. Streptomycin treatment (closed data points, $R^2 = 0.83$), which induces heat shock response (HSR) and rapid ribosome degradation, results in significantly longer recovery times than chloramphenicol treatment (open data points). Here, the two responses are statistically significant ($p<0.05$ by ANOVA). E. The addition of efflux pump inhibitor (CCCP) (closed data points, $R^2 = 0.91$) increases population recovery time in response to chloramphenicol treatment (open data points, $R^2 = 0.80$). Here, CCCP was added at subinhibitory concentrations (3μg/mL); in the absence of antibiotic treatment, CCCP alone did not inhibit population recovery. The CCCP-mediated increase in recovery time is statistically significant ($p < 0.01$). F. The ribosome synthesis rate was increased by enriching the casamino content of the media from 0.01% w/v (closed data points) to 0.05% w/v (opendata points). Faster synthesis resulted in lower recovery times ($p<0.001$). In each of these panels, the color scheme indicates increasing antibiotic concentration, as in Figure 1C. 56

Figure 15: [CCCP] inhibits efflux pump activity in a dose-dependent manner. A. Dose response for carbonyl cyanide m-chlorophenyl hydrazine (CCCP). Seven logarithmically spaced concentrations were chosen, in addition to 0. Growth rates were calculated by log-transforming time series data and calculating the slope of the longest linear segment. Data points are the average of three replicates; black line shows the best fit Hill function ($IC_{50} = 3.87$μg/mL). B. CCCP increases ethidium bromide (EtBr) accumulation, and inhibits antibiotic efflux, in a dose-dependent fashion. A previously published protocol was used to measure the effect of CCCP on efflux pump activity, in the absence of growth. Intracellular EtBr, which acts as a general efflux pump substrate, can be measured via population fluorescence; accumulation is increased in the presence of increasing CCCP concentrations. 59

Figure 16: Antibiotics inhibit a variety of intracellular targets, including ribosome function and protein synthesis (e.g. aminoglycosides, amphenicols, and macrolides), DNA gyrase (e.g. fluoroquinolones) and penicillin-binding proteins (β-lactams).

Previous studies have described PAEs to all of these classes of antibiotics, although some drugs induce minimal transient growth inhibition. 62

Figure 17: Populations are more sensitive to decreases in antibiotic efflux rate in conjunction with rapid target degradation and strong positive feedback in target synthesis. A. Sensitivity is defined as the total change in recovery time in response to a change in the antibiotic efflux rate. B-C. Each trajectory corresponds to one value of the target degradation rate (B, black arrow shows the direction of increasing parameter value) or feedback nonlinearity (C, arrow shows increasing direction). Sensitivity increased with high degradation and feedback nonlinearity, corresponding to the left motif in Figure 11A. 63

Figure 18: Efflux inhibition is an effective co-treatment strategy for certain antibiotics. A. Three general motifs of intracellular antibiotic action. Left and middle motifs correspond to ribosome-inhibiting antibiotics that induce rapid and minimal ribosome degradation, respectively. In these motifs, the target molecule is subject to nonlinear positive feedback (i.e. transcription and translation, in the case of ribosomes). Right motif corresponds to antibiotics that inhibit other targets that are not subject to positive feedback, e.g. β-lactams. In each case, recovery time is a function of total antibiotic, and is significantly lengthened by efflux inhibition. B. Populations are more sensitive to decreases in antibiotic efflux rate in conjunction with rapid target degradation and strong positive feedback in target synthesis. Sensitivity is defined as the total change in recovery time in response to a change in the antibiotic efflux rate (top panel). In panels i-ii, each trajectory corresponds to one value of the target degradation rate (panel i, black arrow shows the direction of increasing parameter value) or feedback nonlinearity (panel ii, arrow shows increasing direction). Sensitivity increased with high degradation and feedback nonlinearity, corresponding to the left motif in Figure 11A. 66

Figure 19: Determining IC_{50} values for various antibiotics. IC_{50} values were calculated from long-term dose responses in 96-well plates. For each antibiotic, seven logarithmically concentrations were tested, using serial dilution. Initial cell density was 100-fold dilution of overnight culture (~2e7 CFU/mL). Growth curves extending up to early stationary phase were collected; maximum growth rates were extracted by log-transforming the data and iteratively determining the longest linear portion. Each data point corresponds to the average of three technical replicates. IC50 values were determined by fitting growth rates to a Michaelis-Menten equation (dashed line), and are shown in each panel (μg/mL). Antibiotics tested are as follows: Chloramphenicol (panel A), carbenicillin (B), tetracycline (C), spectinomycin (D), gentamicin (E),

streptomycin (F), cefotaxime (G), penicillin G (H), norfloxacin (I). IC50 values for each antibiotic are labeled in parentheses. 68

Figure 20: Inhibiting antibiotic efflux with CCCP significantly increased population recovery time in response to a wide variety of antibiotics (penicillin G (PenG), spectinomycin (Spec), gentamicin (Gent), streptomycin (Str), chloramphenicol (Cm), tetracyclin (Tet), and carbenicillin (Carb)). Here, the particular antibiotic concentrations used have been scaled by their respective IC_{50} values (solid points and open circles show response with no efflux inhibition and 2μg/mL CCCP, respectively)..... 70

Figure 21: Bistability results in systems assuming one of two stable states. A. Bistability can arise through a number of mechanisms/motifs, including nonlinear positive feedback (top), wherein a species of interest catalyzes its own synthesis, or mutual negative feedback (bottom), wherein two species each inhibit the synthesis of the other. In each of these cases, a sufficiently strong external stimulus can shift the system from one state to another, e.g. from low A to high A (positive feedback), or high A/low B to low B/high A (mutual negative feedback). B. The transition between bistable states can be visualized in terms of potential energy; stable states correspond to local minima, separated by an unstable intermediate state. If the stable states are of unequal depth, the system will default to the more stable default. C. Hysteresis is a property of bistable systems that refers to the fact that different stimulus histories (e.g. increasing vs decreasing) will result in different response curves and state transition points. Specifically, in the bistable region, the system state is dependent on the stimulus history. 74

Figure 22: Stimulation of a bistable network by a pulse input. A. A pulse input can be specified by its intensity (S) and duration (D). Stimulation of a stochastic bistable network in an isogenic population using this pulse results in the emergence of two distinct subpopulations (e.g. OFF and ON). B. If the activation is deterministic, there exists a critical pulse duration beyond which all individuals in a population will transition between the two steady states (e.g. from OFF to ON) (top panel). Presence of noise will result in variability in the critical duration: different individuals will be activated at different thresholds (middle panel). For a short duration, a fraction of a population will be allocated to either steady state. Here, I aim to investigate this population activation, which I term "activation probability", as a function of both pulse intensity and duration (bottom panel). 80

Figure 23: Response of a positive-feedback model to pulse inputs. A. A minimal positive feedback motif consists of some gene of interest (GOI) which drives its own synthesis by

activating its promoter *P*. Nonlinear feedback is often achieved through cooperative binding, leading to a sensitive response dependent on the initial concentration of the GOI. B. The effect of autocatalysis. In the absence of stimulus (dotted line), the emergence and relative placement of steady states in the non-dimensional model can be tuned with the autocatalytic parameter "c". For low values of this parameter, the only steady state is at 0. However, with sufficiently strong positive feedback, two nonzero steady states emerge. C. Potential energy landscapes as a function of stimulus intensity. If the autocatalysis parameter "c" is chosen such that nonzero steady states are attainable, the potential energy landscape forms two wells corresponding to OFF and ON. Increasing stimulus intensity simultaneously leads to a shallower well at c_{off} and a deeper well at c_{on}. This trend corresponds to an overall shift in the population from OFF to ON with increasing stimulus. Here I used $c = 1.45$, $\epsilon = 0.005$, and $D_e = 0.01$. D. Schematic shows the evolution of a population of cells carrying a bistable switch (blue) in response to a pulse input (red). Potential energy landscapes are shown in black. In the absence of stimulus (1), the population is in the OFF state. When stimulus is applied (2), the potential energy landscape shifts in favor of the ON state, driving the population toward the ON state. When the stimulus is removed (3), the potential energy landscape reverts to its initial state, splitting the population into two subpopulations (OFF and ON). 82

Figure 24: A. Simulation (open circles) vs. theoretical prediction (solid lines) of activation probability as a function of pulse duration. The black arrow indicates increasing stimulus intensity. The activation probability increases linearly with the duration, when the latter is small. Inset shows intermediate signal transformation function. B. The transition rate dictates the linear dependence, and increases with increasing stimulus intensity. Open circles and lines indicate theoretical and numerical predictions, respectively. C. The pulse strength can be monotonically scaled upstream of the bistable decision module without affecting the characteristic activation property. Here, I use a Hill function with coefficient $n = 2$ as the transformation function (shown in inset). 85

Figure 25: Response of a toggle-switch to pulse inputs. A. A toggle switch consisting of two molecules (A and B) inhibiting each other. With sufficient nonlinearity, the system is bistable, with either A or B dominating. Our analysis assumes that all cells are initiated at state A. A pulse input is applied to drive them into state B. B. Simulated dependence of the activation probability on pulse duration. For sub-saturating durations, the dependence exhibits an approximately threshold-linear property: there is no activation until the pulse duration is above a threshold; then the activation probability increases linearly (as shown by solid lines, R2>0.9) until saturation. Black arrow indicates direction of increasing stimulus intensity. C. The linear activation regime slope τ^{-} increases with

stimulus intensity (linear fit, R2=0.987). D. The priming delay D_0 decreases with stimulus intensity (exponential decay R2=0.972). 94

Figure 26: Response of the Myc-Rb-E2F network to pulse inputs. A. In response to serum stimulation, the Myc-Rb-E2F can exhibit bistability in E2F levels. B. Simulated dependence of activation probability on the duration of the pulse input. Solid black arrow indicates increasing stimulus intensity. The dependence is approximately threshold linear for sub-saturating durations. Black arrow indicates direction of increasing stimulus intensity. C. The linear activation regime slope r increases with stimulus intensity (linear fit, R^2=0.997). D. The priming delay D_0 decreases with stimulus intensity (exponential decay R^2=0.985). 97

Figure 27: Determining activation for the Myc-Rb-E2F pathway. A. Simulated E2F time courses in response to a pulse input with varying durations. For sufficiently strong stimuli (e.g. S=5), increasing duration led to a characteristic adaptive response in E2F level (ON). The fraction of individuals exhibiting this adaptive response is a function of stimulus duration. B. and C. OFF and ON populations were delineated by the width of the pulsatile response. For each time course, width of the pulsatile response at the half maximum E2F level was determined. This metric resulted in a bistable distribution: the population centered at the higher mode was taken as the activated fraction. 99

Figure 28: Linear increase in activation probability is a preferable allocation strategy. A. A discrete bistable system allows comparison of various activation probability curves. In this model, successive pulses of unit intensity, mean duration D, and Gaussian-

distributed deviation ΔD_i are applied to a population. For each pulse, a fraction $p(D+\Delta D_i)$ are "activated" and proliferate. The rate of proliferation is assumed to be dependent on the signal intensity per individual $\frac{D+\Delta D_i}{N_i}$, following a Monod function. The remaining inactivated subpopulation is eliminated (i.e. cell death). I note that the conclusions about relative fitness are not affected if the inactivated subpopulation is assumed to be quiescent (alive but non-growing). Successive pulses can be applied to simulate fluctuating environmental conditions. B. Three characteristic activation probability curves as a function of signal duration. Population response can be grouped into one of three categories. A fluctuation in signal duration can result in a corresponding linear change in activation (blue line), or a change that is more sensitive (red line) or less sensitive (green line) than linear. Note that all three representative curves are defined over the same range of signal durations, and $k(0)=0, k(500)=1$ for all. C. For each characteristic curve in (B), I plot the fold change after 1,000 pulses of a particular mean duration. A linear allocation strategy results in a larger fold change than fast and slow activation for 100% and

86% of signal durations, respectively. I note that this qualitative conclusion is true regardless of initial population size and number of pulses. 103

Figure 29: Determination of p_{act} from stochastic simulations of the positive-feedback model. A. Due to the presence of stochastic noise, replicates with identical initial conditions form distributions centered around two steady states. B. Time courses of 10,000 simulations were separated into OFF and ON fractions based on the boundary given by the critical unstable concentration value (middle panel, dotted line). C. The ON fraction was then plotted as a function of stimulus duration (right panel). I used the same method to evaluate the positive-feedback model and the toggle switch model. .. 109

Figure 30: Recovery dynamics in response to periodic dosing. A. Periodic dosing regimens can be specified by four key parameters: the antibiotic concentration A, the dosing interval T_1, the time between doses T_2, and the total number of doses, n. I denote the recovery time following n doses as RT_n. B. Dosing parameters dictate treatment efficacy. Here, the heatmap colors indicate recovery time after $n = 3$, for each combination of T_1 and T_2; yellow corresponds to large recovery time (i.e. a successful treatment) and blue corresponds to a low recovery time (i.e. treatment failure). C.—D. The boundary between treatment efficacy and failure (as shown by the color map, is dependent on the antibiotic concentration and number of doses. Intuitively, as either of these parameters increase, the space of (T_1, T_2) over which treatment remains effective increases..... 114

Figure 31: RT_1 predicts the efficacy of RT_n treatments. A. Here, each trajectory corresponds to one value of T_2, and colors correspond to increasing values of A; each data point corresponds to a single multi-dose treatment. There is a sharp transition in treatment efficacy (as measured by RT_n) at $\frac{T_2}{RT_n} = 1$; that is, the recovery time in response to a single dose corresponds to the maximum value of T_2 that results in a successful multi-dose treatment. B. As in C, but using a minimal degradation motif (FIG). 115

Figure 32: A proposed gradient chip design. Here, media flows from right to left, and subsequent mixing channels create a gradient of antibiotic concentration (or any other media condition of interest). This module would be placed upstream of any experimental chip and allow the user to test a wider variety of conditions without significantly increasing the amount of external hardware required. 116

Acknowledgements

There are so many people without whom I would not be the person I am today, and without whom graduate school would not have been the same experience. I am eternally grateful for all of them, past and present.

First and foremost, I thank my parents. For always giving me a place to return to, for showing me everyday that family is a priceless and unbreakable bond. For the happy memories and the hard lessons, for teaching me the values of determination and effort. For inspiring in me a love of math and science, and setting me on the path to today. For always being there when I needed help, and for listening when I didn't want to talk. The world is a big place, and because of them, there will always be a corner of it that will be home. My brother Rono; we've gone through life together, from playing soccer in the backyard to high school and college and now the real world (he had a bit of a head start on me on that one).

I would like to thank my committee members: Dr. Charles Gersbach, Dr. Brenton Hoffman, Dr. Katia Koelle, and Dr. John Neu, for their invaluable advice on my work. I am grateful to the Duke Center for Biotechnology and Tissue Engineering for funding two years of my graduate career.

Importantly, I am grateful for the many friends I have been fortunate enough to make over my time in graduate school, both inside and outside of the lab. Drs. Robert Smith, Anand Pai, Yu Tanouchi, and Stephen Payne welcomed me to the lab and made me feel comfortable in what was initially an alien environment than I was used to. Rob in particular taught me so much and established the beginnings of the research path I took through graduate school. I will always be grateful for his willingness to answer every question and explain every mistake. That corner of the lab, with those four gentlemen, was always good times and good advice, liberally seasoned with jokes and good-natured fun. I thank my current labmates; we've shared all the triumphs and tribulations together. I'd particularly like thank Allison Lopatkin, whom I've had the pleasure of working with and the honor of being friends with. Through all the ups and downs, she has made me a better person, and I am lucky that she is my closest friend.

I'd like to thank the group of friends with whom I've shared the past several years. Hrishikesh Rao, Wyatt Shields, Kedar and Sneha Prabhudesai, Nicholas Tang, Swarnali Sengupta and Dave Bjeergard, Nick and Beth Bottenus, Jeff and Kara Schaal, for all the memories, discussion, support, jokes, and the good times.

Finally, I would like to thank my advisor, Dr. Lingchong You, for his help and guidance throughout my time in graduate school. I came to his lab after a last-minute email and interview, and I am grateful to him for taking that chance on me. He has devoted many hours to mentoring me through projects, always adapting his mentoring style to best fit the circumstances. In addition to his academic guidance, he was extremely generous in enabling my internship experience. Throughout my graduate career, he has made me a better scientist and researcher, and I am grateful for his impact.

1. Introduction

In this chapter, I discuss the initial development of antibiotics, and the various modes by which bacteria (including pathogens) are able to survive drug treatment: genetic resistance, phenotypic resistance, and population density-dependent behaviors. I also touch on potential treatment strategies to counteract each of these survival mechanisms. Finally, I give a short primer on the applications of microfluidic platforms and mathematical modeling as they apply to the study of bacterial dynamics and antibiotic resistance.

1.1 Antibiotics and resistance: a brief history

The earliest antibiotics were derived from industrial dyes, and originally used as cytological stains[1]. In the late 19th and early 20th centuries, Paul Ehrlich hit upon the idea of using methylene blue as a suitable dye for bacterial cells[2]. In a seminal leap of genius, Ehrlich surmised that the dye, effective in staining against *Plasmodiidae* (including the malaria pathogen), could be used as a chemotherapeutic agent. Future work would avoid the side effects of methylene blue and arrive at quinine[3]. The second keystone discovery was that of the inhibitory effects of penicillin mold by Alexander Fleming in the 1920s[4], which led to the entire class of penicillin antibiotics. Indeed, the period between 1940 and 1970 was characterized by rapid discovery and implementations of

large number of antibiotics, including beta-lactams[5], aminoglycosides[6], fluoroquinolones[7] and others[8]. These drugs inhibited pathogens through a multitude of methods, including protein synthesis inhibition, DNA/RNA synthesis inhibition, and compromising the cell wall. It seemed as though society was well on the way to finding a *therapia sterilisans magna*, the "magic bullet" treatment that Ehrlich imagined[9]. Indeed, by 1969 the surgeon general remarked "… that we had essentially defeated infectious diseases and could close the book on them"[10]. Without question, antibiotics were arguably the greatest medical discovery of the 20th century.

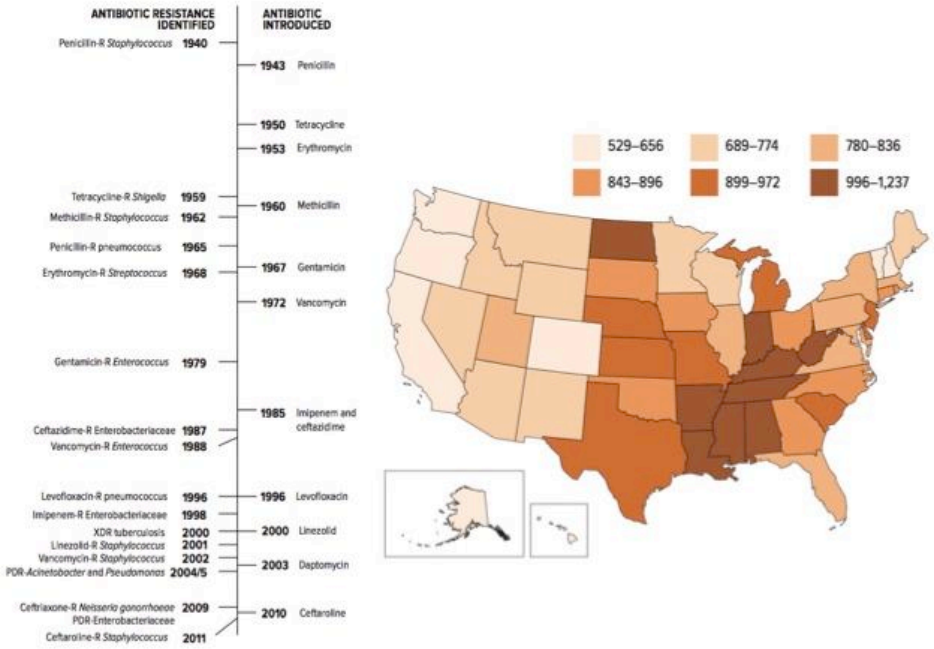

Figure 1: Left panel shows a timeline of antibiotic development and subsequent emergence of resistance. The placement of antibiotics above the timeline corresponds to the year each was deployed, while the placement below the time corresponds to the year resistance was first observed. Here, it is important to note that

observation of resistance does not necessarily imply loss of all clinical utility. Right panel shows the frequency of antibiotic prescriptions (per 1000 people) on a state by state basis. Figure reproduced with permission from[11].

This golden period of antibiotic development lasted approximately 50 years; during this time, many compounds were either discovered or derived, and infectious disease seemed destined to quickly be a museum artifact. However, bacteria are nothing if not adaptable; and given their rapid duplication time, they undergo evolution on timescales much more rapid that what I might think. Even as antibiotics were being developed, bacteria were generating and utilizing a wide array of strategies to survive drug treatment. Indeed, this natural evolution has progressed much more rapidly than novel antibiotic development (Figure 1)[11]. To compound this problem, the pharmaceutical industry simply is not interested in developing novel antibiotics, which are financially unattractive: typical infectious diseases require at most a few weeks of antibiotic treatment, whereas more chronic conditions, such as hypertension, diabetes, and heart disease, often require life-long treatment[10]. These chronic illnesses generate a much higher profit for pharmaceutical companies, and indeed, the latter half of the 20th century saw a drastic halt in the development of new antibiotics. However, due to a combination of bacterial evolution, over-prescription and misuse of existing drugs, resistance soon emerged to nearly every antibiotic in use[11]. Indeed, since the 1930s, the

window of efficacy between the development of a novel antibiotic and the emergence of resistance has dramatically shortened[12,13], leading many to wonder whether I are returning to the "dark ages" of the pre-antibiotic era[14].

As the scientific community and the wider public gradually return to acknowledging the importance of antibiotic development and stewardship[15], effectively addressing this emergent crisis requires two complementary strategies. One is to develop novel drugs and therapeutic methods to combat bacterial infections. It is equally critical to develop effective antibiotic treatment protocols that can extend the efficacy of existing antibiotics. Antibiotic treatment regimens that are optimized to minimize the amount of antibiotic used, while concurrently minimizing the chance of pathogen proliferation will extend the "shelf-life" of common approved antibiotics and ensure that resistance does not spread.

1.2 Mechanisms of antibiotic resistance

Bacterial resistance to drugs can arise through myriad pathways (Figure 2A). In many cases, resistance is genetic – an individual bacterium acquires a stable mutation that allows it to withstand antibiotic treatment. Genetic resistance can arise from *de novo* mutations or horizontal gene transfer[16]. This subpopulation then proliferates and

eventually dominates the original genotype. Such mutations often lead to the upregulation of drug efflux pumps that drive antibiotics out of individual cells[17-19], increased synthesis of some antibiotic-degrading enzyme that effectively decreases the intracellular antibiotic concentration below toxic levels[20], or modifications in cellular target proteins that render antibiotic binding and action less effective[16,21]. Regardless of the particular mechanism, genetic resistance is a natural implication of microbial evolution; it is an unavoidable risk inherent in all antibiotic treatments. Indeed, many studies have shown that antibiotic treatments themselves may increase the likelihood of genetic resistance[22].

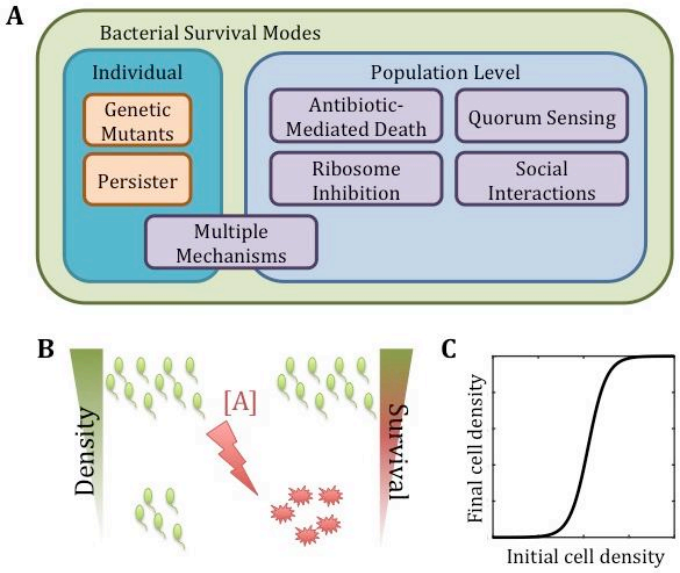

Figure 2: Antibiotic tolerance mechanisms and collective antibiotic tolerance (CAT). A. Bacteria can survive antibiotic treatment through a variety of mechanisms, either on the individual or population level. Often, multiple mechanisms are at play. B. Collective antibiotic tolerance (CAT) is defined as a population density-dependence at intermediate antibiotic concentrations. For example, at low

concentrations, populations are able to withstand treatment regardless of density. Conversely, at high antibiotic concentrations, populations are inhibited regardless of density. However, at intermediate concentrations, population fate depends on initial density. C. CAT is characterized by a transition in population fate as a function of initial density.

Genetic resistance is distinct from, and often preceded by, *antibiotic tolerance*. Antibiotic tolerance is distinguished from resistance in that it is phenotypic: tolerant populations are genotypically identical to their sensitive counterparts[23]; however, they utilize a number of mechanisms to survive antibiotic treatment. Perhaps the most well-known is persistence, in which a subpopulation enters a dormant, non- or slow-growing state upon encountering antibiotic stress[24]. Tolerance can also emerge via population-level behaviors; this class of mechanisms is called collective antibiotic tolerance (CAT), and includes a myriad of density-dependent strategies such as the collective synthesis of resistance-conferring enzymes, antibiotic titration, and social interactions within and between populations[25-27]. Here, the premise is that members of a population share the burden of antibiotic tolerance; this requires that a population surpass a minimum density. CAT mechanisms are characterized by this density dependence: populations at high densities are able to withstand treatment that would be inhibitory to low density populations (Figure 2B-C). Moreover, CAT enables a population to recover faster than

persisters, and provides a time window for otherwise susceptible bacteria to acquire more permanent genetic resistance [27].

1.3 Phenotypic persistence

In many cases, a population of predominantly sensitive cells also contains a small subpopulation of cells, called persisters, which exhibit a reduced growth rate. These persisters may emerge stochastically, in response to stress, or due to errors in replication and cell metabolism[28,29]. Ultimately many persistence pathways function through the induction of stress responses[30]. Persisters are genetically identical to susceptible cells but are tolerant to antibiotics[29,31]. In the absence of antibiotics, persisters can switch back to the growing state, leading to population recovery. As a result, persisters can cause post-treatment relapses and enable development of genetic resistance[31]. Unlike genetic resistance, persistence is non-inheritable, though the frequency of persisters in a population can be genetically determined[31,32].

1.4 Population-level behaviors

Both genetic resistance and phenotypic persistence are predicated on single-cell behavior: the likelihood of a given cell acquiring resistance through either mechanism is independent of its neighbors. In contrast, the following phenomena are density-

dependent; that is, they are all collective mechanisms that are effective at initial cell densities above a critical threshold (Figure 2C).

1.4.1 Antibiotic-mediated altruistic death

Genetic antibiotic resistance arises from the expression of resistance-conferring proteins, which often degrade or modify the antibiotic [16]. However, single-cell expression levels these proteins may be insufficient to protection, depending on the antibiotic concentration. If so, the fate of a bacterial population will depend on its density (Figure 3A): population survival is determined by the relative rates of antibiotic-mediated killing and population (enzyme)-mediated antibiotic degradation. In general, the population will initially decline due to antibiotic-mediated killing of a subpopulation of bacteria. This death is altruistic because the subpopulation releases resistance proteins that degrade global antibiotic concentrations to the benefit of surviving cells [33,34]. The importance of population density is inherent in these two rates: if the initial population density is too low, the population will be eradicated before the antibiotic is degraded to a sub-lethal level. Conversely, if the initial population density is sufficiently high, the total resistance protein can clear the antibiotic before complete eradication of the population, allowing the survivors to repopulate. The interplay between cell growth, antibiotic-mediated killing, and antibiotic degradation by the resistance protein from

cells (live or dead) will result in CAT. Indeed, smaller inocula of pathogens expressing β-lactamases (Bla) are more susceptible to β-lactams than larger inocula [35]. Such CAT often arises from constitutive expression of Bla and other resistance proteins [36]. Alternatively, many pathogens' Bla expression is up-regulated through the induction of *ampC* in the presence of β-lactam antibiotics [36].

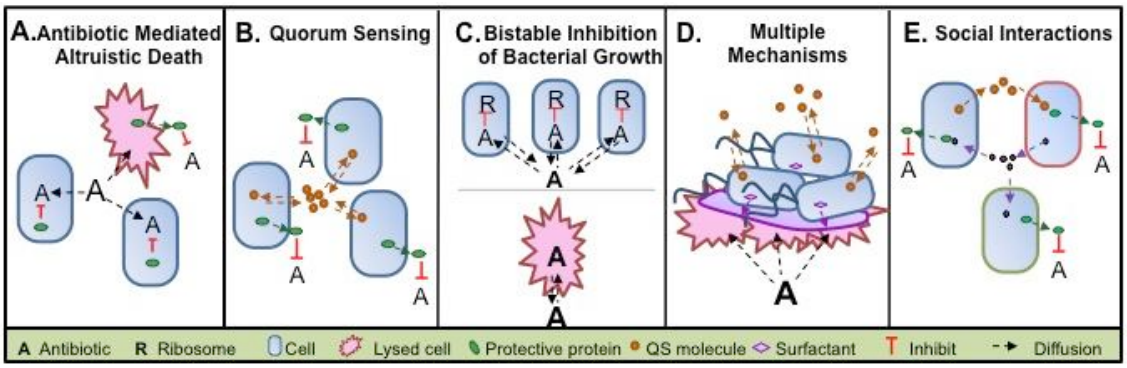

Figure 3: Diagrammatic description of various CAT mechanisms. A. In PAD populations, cells produce a beneficial molecule e.g. a drug-degrading enzyme, often termed public good, intracellularly. In response to antibiotic stress, a fraction of cells lyse, releasing the intracellular public good to the global environment, where surviving cells benefit (hence "altruistic). B. QS populations synthesize a signaling molecule, often an N-acyl homoserine lactone (AHL), that is secreted to the global environment. These signaling molecules diffuse into local cells and act as a proxy for local cell density. When the local signal concentration exceeds a critical threshold, downstream gene expression (e.g. production of an antibiotic-degrading enzyme) leads to population survival. C. Antibiotics diffuse into individual cells, where they inhibit ribosome function and protein synthesis. At sufficiently high population densities, the intracellular antibiotic concentration is sub-inhibitory, leading to population survival. D. These mechanisms often act in parallel to enable antibiotic tolerance. E. Moreover, the metabolic burden of gene/protein expression is often shared in multi-species consortia. This can lead to social interactions, e.g. mutualism, commensalism, and others.

Altruistic death of partial populations, as outlined above, is a natural consequence of antibiotic action, and is not limited to β-lactam antibiotics. In other contexts, antibiotic-mediated death is genetically programmed[33]. For example, some antibiotics effect bacterial death by interfering with toxin-antitoxin systems[37]. The *mazEF* system can result in programmed cell death (PCD) when an antibiotic, such as chloramphenicol, inhibits the transcription/translation of the MazE antitoxin[38]. Without the labile MazE antitoxin, the stable MazF toxin accumulates and triggers PCD. Other antibiotics, such as fluoroquinolones, trigger PCD by inducing an SOS response[39]. During stress response, PCD can benefit survivors by directly or indirectly relieving stress[33,34]. When this occurs, the use of antibiotic can promote the survival of a pathogen and aggravate its virulence. For instance, antibiotics induce PCD in Shiga toxin (Stx)-producing *Escherichia coli* (STEC) O157:H7. Encoded in a bacteriophage[40], Stx is assembled and released upon cell lysis. Stx kills nearby eukaryotic predators, thereby enabling STEC growth and survival[41]. Death here is altruistic and required for the release of Stx. The population must be large enough to afford the cost of lysing the bacteria necessary to release sufficient Stx for survival.

1.4.2 Quorum sensing (QS) and biofilm formation

If it is costly to produce a given resistance protein, cells may delay synthesis until the cell density is high enough such that the overall benefit of the protein outweighs its metabolic cost. This delay can be realized by quorum sensing (QS), which enables bacteria to coordinate gene expression in a density-dependent manner[42,43]. In QS, individual cells produce and secrete a diffusible signaling molecule; this signaling molecule acts as a density sensor, increasing in extracellular concentration with cell density. Using the signal concentration as an inducer of downstream gene expression, coordinate behavior (e.g. resistance protein synthesis) according to their density[42].

QS often controls the expression of resistance-conferring enzymes (Figure 3B). In *Providencia stuartii*, a Gram-negative pathogen that causes urinary catheter infections, QS controls the expression of an acetyltransferase, which inactivates aminoglycoside antibiotics[44,45]. Low-density populations express minimal levels of acetyltransferase, rendering them sensitive to aminoglycosides; high cell density triggers acetyltransferase expression, yielding CAT. Using a synthetic gene circuit, Pai *et al.* demonstrated that QS represents an optimal strategy to control the expression of a costly protein that benefits the entire population[46].

QS also contributes to CAT by modulating biofilm formation, which enhances antibiotic tolerance[47]. Although the specifics of biofilm formation vary by species, the general steps are similar[43,48]. Planktonic bacteria first attach to a surface at a low density and begin to form microcolonies, while producing basal levels of QS signals. Once the population reaches a sufficiently high density, the accumulated QS signals activate genes involved in biofilm formation[42]. Depending on the antibiotic and bacterial specie, the surface layer of biofilms may serve as a protective barrier for resident bacteria by reducing the penetration rate of some antibiotics[49,50]. Moreover, some antibiotics, such as piperacillin or ampicillin, can induce antibiotic-deactivating enzymes in biofilms, which can further reduce antibiotic penetration and the killing of biofilm-residing bacteria[51,52]. Biofilms also have limited nutrients at their core, which diminishes internal cell growth. These slow growing cells tend to be less sensitive to certain antibiotics[53].

1.4.3 Bistable inhibition of the replication machinery

When bacterial populations produce a resistance-conferring protein, density-dependence may be intuitive: increasing cell density increases total protein production, thus increasing the likelihood that a population will survive treatment[54]. However, CAT has also been observed in response to antibiotics that inhibit ribosome activity and protein synthesis (e.g. aminoglycosides) without requiring production of degrading

enzymes[55]. Tan *et al*. established a mechanism for CAT in the absence of active antibiotic degradation: intra-population antibiotic titration coupled with bistable ribosome inhibition[25] (Figure 3C). In this scenario, ribosome synthesis in individual cells is controlled by positive feedback: ribosomes translate mRNA into proteins, including ribosomal components, resulting in ribosome synthesis[56]. This feedback can be inhibited by intracellular antibiotic, resulting in a bistable response[57].

Within a population, the extracellular antibiotic is allocated to individual cells according to the import and export rates across the cell membrane. When import is faster than export, the intracellular antibiotic will be higher than the extracellular concentration, and will decrease slightly with increasing cell density. This decrease is amplified by ribosomal positive feedback, leading to bistable growth inhibition: at high cell densities, the average intracellular antibiotic concentration is relatively low (below minimum inhibitory concentrations), positive feedback overcomes antibiotic inhibition and enables population survival. Modeling suggests that density dependence can be modulated by altering various processes, such as drug uptake and binding. However, the critical condition required for CAT in this scenario is the rapid degradation of ribosomes, which can be triggered by antibiotics that target ribosomal components. These antibiotics induce heat-shock response[58], which leads to upregulation of proteases

and faster degradation of ribosomal components[59]. If the ribosome degradation rate remains slow, as with chloramphenicol treatment, the population fate is density-independent: populations either grow (low antibiotic concentrations) or die (high antibiotic concentrations). When coupled with direct induction of heat shock, however, these antibiotics can also cause bistable inhibition of population growth, leading to CAT.

1.4.4 Mixed strategies

In nature, CAT often arises from traits that are controlled by combinations of the mechanisms discussed above. For example, when PCD is coupled with density-dependent gene expression in *Staphylococcus aureus*, lysis is tightly controlled and can result in CAT through biofilm formation. CidA and LrgA expressions turn lysis ON and OFF at specified stages of cell growth, respectively[60]. Lysis releases genomic DNA, resulting in enhanced biofilm formation[61,62]. These genes have been linked to regulation of antibiotic tolerance: mutations disrupting CidA or LrgA enhance or reduce population survival, respectively[60,63].

Another strategy to survive antibiotic treatment involves a combination of phenotypically shifting from a "swimming" state (planktonic growth) to a “swarming” state (surface growth), QS, and altruistic death (**Figure 3D**). Swarming is flagella-driven

group-migration of bacteria over a semi-solid surface and happens exclusively at the leading edge of a population[64,65]. Although the underlying mechanisms are species dependent and not fully elucidated, some swarming species have been observed to rely on QS to upregulate the production of biosurfactants, such as rhamnolipids, which are necessary for reducing surface tension[64]. Swarmers exhibit increased tolerance to a variety of antibiotics, including aminoglycosides and fluoroquinolones[65,66]. Altruistic death may contribute to this survival advantage. It is speculated that cells dying from prolonged direct contact with the antibiotic form a protective platform that prevents other swarmers from coming into direct contact[65]. Thus, the population has to have a high enough density to upregulate QS-mediated swarming genes[65] and afford the cost of individuals that are directly exposed to the antibiotic. While swarming and biofilm formation involve similar mechanisms, such as altruistic death and QS, the two states are inversely regulated[67,68]. As a result, biofilms contain a population of sessile cells while swarms disperse a population of active cells[68].

The mechanisms underlying swarming-mediated motility and density-dependent survival appear to vary between species; QS has been implicated in *Pseudomonas aeruginosa*[64], but not in *Salmonella*[65]. Other studies have examined the impact of biofilm creation[65] and increased efflux pump expression[69]. Swarming motility has

been observed to strongly correlate with the expression of the *pmrHFIJKLM* operon[66]. This operon encodes the lipid A portion of LPS, which reduces the binding strength of various antimicrobial peptides[70]. Kim *et al*. showed that *pmrK* expression is upregulated in conditions that promote swarming. Expression decreases as cells de-differentiate from the swarming phenotype, and knockout results in the loss of swarming ability[66].

1.4.5 Social Interactions

In a mixed population, CAT can be facilitated by "charitable" actions, wherein one subpopulation produces a product that helps another subpopulation, without receiving any benefit from the latter (Figure 3**E**). Lee *et al*. demonstrated that a population of drug sensitive *E. coli* can tolerate antibiotic with the aid of a few highly resistant population members[71]. In the absence of antibiotic, the entire population produces indole, a signaling molecule generated by growing bacteria. In the presence of an antibiotic, however, only a subpopulation with mutated efflux pumps has the resistance necessary to continue producing large amounts of indole. The released indole upregulates efflux pump expression and oxidative-stress mechanisms, thus enabling the entire population to tolerate the antibiotic. This survival tactic will fail if the fraction of mutant indole producers is too small to support a large population of sensitive cells or if the metabolic cost of production is too high.

CAT can also arise from *mutualistic* interactions, where two or more bacterial populations depend on one another to survive. Hu *et al.* used an engineered system to demonstrate how two populations can collaborate to survive different antibiotics[27]. Each engineered population produced the QS signal molecule needed by the other to upregulate the production of a resistance protein. Increasing either population's initial density increased QS signal accumulation, resulting in higher final densities following antibiotic treatment. Similarly, multispecies swarms can arise due to the communal nature of QS signals. For example, *Serratia ficaria* do not produce biosurfactants, but they do produce QS signals necessary for S. *liquefaciens* QS-deficient mutants to upregulate their own biosurfactant production. Once sufficient signaling molecules accumulate, *S. liquefaciens'* biosurfactant production facilitates the swarming[72] and, presumably, the CAT of both populations. Another example of mutualism-mediated CAT can be found in multi-species biofilms[73]. For example, species can work together to decrease antibiotic penetration of biofilms. *Burkhodia cepacia* and *P. aeruginosa*, both associated with cystic fibrosis, produce polysaccharides that interact to increase biofilm viscosity and decrease antibiotic activity[74].

1.4.6 Density dependent survival leads to faster recovery from antibiotic treatment

The mechanism by which bacteria survive antibiotic treatment can significantly influence the speed of their recovery. Here, previously published models were used to compare the recoveries of populations dependent on different forms of CAT or persistence[25,32 ,46,75]. The three CAT populations (QS, ribosome inhibition, and PCD) recover significantly faster than the persister-dependent population (Figure 4A). Intuitively, the recovery times (defined as the time required for a population to double following treatment) decrease as the initial population density increases. Populations surviving by enzyme-dependent CAT actively degrade antibiotic; thus, the antibiotic concentration is quickly reduced to sub-inhibitory levels, enabling recovery. In the case of bistable ribosome inhibition, at high cell densities, the intracellular antibiotic concentration is insufficient to overcome the positive feedback in ribosome synthesis, again leading to rapid recovery. Conversely, recovery via persisters requires a relatively long time period due to the dependence on the slow, intrinsic removal of the antibiotic and the low frequency of persister formation (Figure 4B).

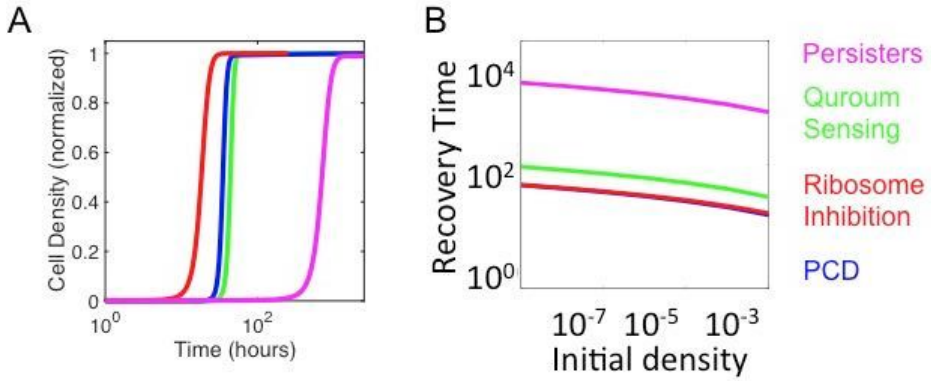

Figure 4: CAT, compared to persistence or genetic mutation, enables rapid population recovery. A. The mechanism by which bacteria survive antibiotic treatment can significantly influence the speed of their recovery. Here, previously published models are used to compare the recoveries of populations dependent on different forms of CAT or persistence[24,25,76,77]. The three CAT populations (QS, ribosome inhibition, and PCD) recover significantly faster than the persister-dependent population. B. The recovery times (defined as the time required for a population to double following treatment) decrease as the initial population density increases. Populations surviving by enzyme-dependent CAT actively degrade antibiotic; thus, the antibiotic concentration is quickly reduced to sub-inhibitory levels, enabling recovery. In the case of bistable ribosome inhibition, at high cell densities, the intracellular antibiotic concentration is insufficient to overcome the positive feedback in ribosome synthesis, again leading to rapid recovery. Conversely recovery via persisters requires a relatively long time period due to the dependence on the slow, intrinsic removal of the antibiotic and the low frequency of persister formation.

1.5 Implications for antimicrobial treatment strategies

Despite their common features, various mechanisms implicated in CAT can lead to distinct population and evolutionary dynamics. These dynamics must be taken into account when developing novel, effective treatment strategies.

1.5.1 Timing in antibiotic dosing

As discussed, CAT populations are most vulnerable at low population densities. It follows that bacteria growth could be more effectively inhibited by timing antibiotic dosing to target early-stage infections, in which the population density is insufficient to utilize cooperative mechanisms. Indeed, A mouse study on treating STEC infections showed early treatment (1-3 days after infection) with a lysis-inducing antibiotic resulted in zero mortality, while late treatment (3-5 days) resulted in 95% mortality[78]. Targeting early stage infections is also effective in treating biofilms; studies have demonstrated that immature biofilms are more susceptible to antibiotic treatment[79,80]. These improved treatment outcomes may be due to a myriad of factors, including suppression of growth and/or virulence factor synthesis.

Indeed, pharmacokinetic/pharmacodynamic (PKPD) considerations can result in drastically different outcomes in response to periodic treatment. Tan *et al*. demonstrated that different periodic dosing frequencies have drastically different outcomes when treating a population capable of generating CAT due to bistable ribosome inhibition[25]. When antibiotic doses were delivered at high frequency, populations had insufficient time to recover. Conversely, when doses were delivered at low frequency, the antibiotic eradicated the population to such an extent that it could not recover. For intermediate

frequencies, however, treatment was ineffective; populations recovered between doses. Furthermore, the frequency range over which populations were able to survive can be modulated by changing the fraction of each period spent at a high antibiotic concentration. In general, the optimal dosing protocol will likely depend on the specific types of mechanisms by which CAT arises, representing a significant direction for quantitative biology research.

1.5.2 Molecular interventions to disrupt CAT

Different mechanisms underlying CAT also suggest potential targets for molecular-level intervention (Figure 5). For example, CAT facilitated by enzyme expression can be reduced by inhibiting either the production or the action of the enzyme. These strategies are often adopted for treating bacteria that produce β-lactamases (Bla); weak inducers of AmpC Bla production, e.g. cefepimes and piperacillin, have been shown to have lower MICs when treating inducible pathogens[81]. Alternatively, Bla-inhibitors, e.g. clavulanic acid, sulbactam, and tazobactam, are frequently used in conjuction with a β-lactam antibiotic to treat Bla-producing bacteria[82]. It should be noted that some bacteria have already evolved resistant mechanisms to Bla inhibitors[83].

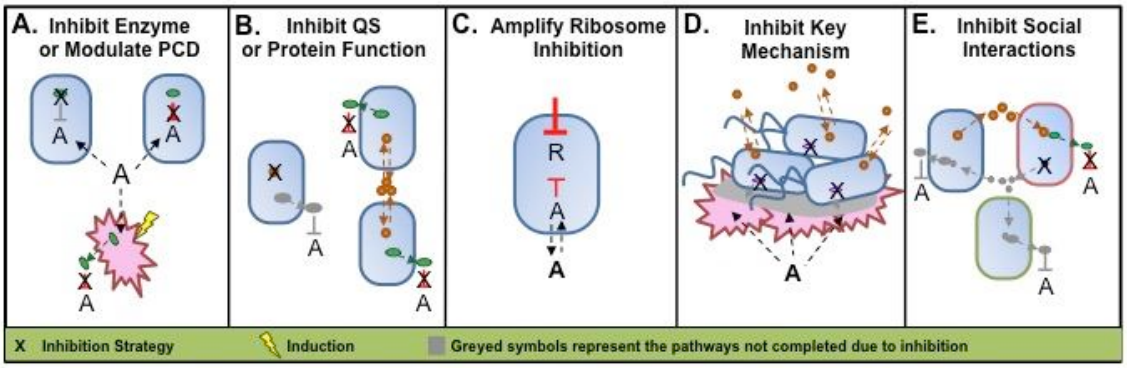

Figure 5: Treatment strategies to inhibit CAT. CAT mechanisms can be attenuated via a number of specific strategies; inhibiting the synthesis or function of antibiotic-degrading enzymes and/or signaling molecules (A-B), increasing ribosome inhibiton (C), or inhibiting specific mechanisms/interactions in consortia (D-E).

PCD can be inhibited with a number of strategies. For example, cell lysis can be induced before sufficient levels of some beneficial enzyme are produced (Figure 5**A**). Indeed, studies have begun to screen antimicrobial peptides that have increased efficacy in activating killing by triggering bacterial toxin-antitoxin systems[84,85]. For some pathogens, however, activation of PCD alone may be undesirable as it can enhance bacterial survival and virulence. Instead, PCD inhibition can reduce virulence by suppressing the release of effectors that promote bacterial survival or virulence. For example, in *Streptococcus pneumoniae*, release of a virulence factor to extracellular space is mediated by autolysis of a subpopulation of cells[86], which in turn can benefit survivors. Serum from mice immunized with autolysin inhibited autolysis and reduced bacterial

virulence[86]. As demonstrated using synthetic gene circuits[75], reduced lysis can paradoxically lead to overall worse bacterial survival.

Similar strategies that inhibit either the production or the action of an enzyme have been applied to target QS pathogens (Figure 5**B**). Targeting QS is appealing as it can reduce virulence without directly targeting the immediate survival of cells. For example, azithromycin has been shown to inhibit QS signaling, leading to inhibition of biofilm formation and virulence in *P. aeruginosa*[87,88]. Likewise, enzymes, such as AiiA that hydrolyze QS signal molecules[89] and synthetic molecules that prevent AHL receptor activation[90], can also block QS signaling and lead to decreased virulence and increased susceptibility to antibiotic treatment in QS pathogens[91]. Drugs that target the function of QS-mediated proteins have also been studied. Oseltamivir is a drug originally developed to inhibit viral production of neuraminidase. As neuraminidase is also a QS-mediated enzyme essential for *P. aeruginosa's* initial colonization process and subsequent biofilm formation, oseltamivir has been tested for its ability to inhibit biofilm formation. Indeed, Soong *et al.* observed a dose-dependent decrease in biofilm formation when oseltamivir was applied [92]. Here, it is important to emphasize that treatment strategies that inactivate signaling molecules or beneficial enzymes molecularly (e.g. inactivation, titration, etc) are advantageous over targeting molecule/enzyme production; by

targeting an inert molecule as opposed to a physiological process, these strategies minimize selection risk[93].

Rapid ribosome turnover is a prerequisite to generate CAT in response to antibiotics that target protein synthesis[25]. As the rate of ribosome turnover increases, the range of antibiotic concentrations over which CAT occurs shrinks and shifts towards lower values. To reduce or eliminate CAT, future drug development could focus on alternative avenues to disrupt ribosome efficacy, such as interfering with subunit assembly[94] (Figure 5**C**). Targeting pathways involved in the stringent response could also eliminate CAT (e.g. relA, ppk). In response to various stresses, many bacterial species reduce rRNA transcription and ribosome synthesis while up-regulating amino acid synthesis[95]. These metabolic shifts can promote bacterial survival and virulence[96]. Inhibition of such metabolic shifts could prevent CAT at high population densities. These pathways may thus represent potential targets for new drugs[97].

Kim et al. observed that a fundamental requirement for swarming is the production of extracellular surfactants, particularly lipopolysaccharides (LPS), which lubricate cells' local environment so they can "slide" past each other[66]. Therefore, the increased antibiotic tolerance exhibited by swarmers could be avoided by inhibiting LPS

production[98]. Previous studies have shown that LPS inhibition by antimicrobial peptides results in the loss of swarming motility[70]. A caveat is that inhibiting swarming motility could lead to increased biofilm formation[99], as these phenotypes are often linked.

Finally, mixed populations can be inhibited by targeting the keystone members, those that facilitate the survival of the majority of co-inhabitants (Figure 5**D-E**). In the case of charitable interactions, treatments should target the subpopulation producing the resistant protein that protects producers and non-producers alike. For instance, penicillin treatment of tonsillitis is often ineffective due to mixed populations of Bla producing pathogens that protect *Streptococci*. However, the infections were effectively treated upon the introduction of a Bla inhibitor, clavulanic acid[100]. In a mutual relationship, such as in Hu *et al.*'s synthetic system[27], survival depends on both subpopulations being present. For such systems, a viable treatment strategy could be to disable one subpopulation such that all participating subpopulations are more susceptible to treatment. To this end, Clustered Regulatory Interspaced short palindromic repeats (CRISPR)-Cas systems could represent an ideal antimicrobial strategy to directly target the specific sub-populations that promote CAT. This genome-editing tool utilizes targeted guide RNA sequences that can be designed to recognize desired bacterial DNA and induce nucleic acid breaks, which can disrupt gene function

in the target. Indeed, recent studies demonstrate the ability to customize antimicrobial treatments by the targeted inactivation or killing of specific bacteria within a population through CRISPR delivery[101,102].

1.5.3 Treatment considerations

Depending on the underlying mechanisms, complex treatment responses could arise from populations capable of CAT. One counterintuitive response is the Eagle effect, a phenomenon wherein increasing antibiotic concentration promotes bacterial recovery[103]. Whether and to what extent the Eagle effect happens in the clinical setting remains to be tested; however, the Eagle effect has been observed to result from PCD-mediated tolerance *in vitro*[75]. Another example is the counterintuitive effect of inhibiting different aspects of QS. Inhibiting QS signal synthesis effectively increases the cell density threshold required to trigger downstream gene expression, such as virulence factor production[104]. However, QS inhibition also alleviates the metabolic burden placed on each cell, resulting in faster growth[46]. Despite this caveat, the overall outcome of QS signaling inhibition ultimately depends on bacterial survival and virulence development. The treatment would likely be considered successful if the target bacteria are rendered non-pathogenic[105].

While QS inhibition can attenuate virulence in the short term, it can promote the selection of more virulent pathogens in the long term[106]. For example, long-term inhibition of QS signaling in *P. aeruginosa* by azithromycin can select for more cooperative and virulent individuals[88,106]. Azithromycin inhibits general protein synthesis; however, it has been shown that QS-regulated genes are among the most severely inhibited by this drug[107]. Over an 11-day course of azithromycin in patients, Köhler *et al*. observed a slight decrease in the frequency of QS-deficient mutants; the QS-deficient mutant frequency in the placebo group increased approximately 2-fold[106]. One possible explanation for this counterintuitive response is, when uninhibited, the cooperative nature of QS is prone to cheaters: cells that do not produce virulence factors exploit the benefit while avoiding the cost of public good production[108]. Cheaters, therefore, are less virulent, but have a fitness advantage. For instance, *P. aeruginosa* cheaters that are QS-deficient due to LasR mutations have a growth advantage over the wildtype[88,109]. When the QS signal is inhibited and no public goods are synthesized, the fitness advantage by the cheaters will be reduced, making it more difficult for them to outcompete cooperators. The negative consequences of direct inhibition of enzyme production may be avoided by inhibiting the enzyme after it is produced[110]. This strategy aims to maintain the cost of enzyme production while eliminating the benefits, leaving virulent bacteria at a metabolic disadvantage and more vulnerable to treatment.

This method may also reduce the selective pressure induced by antibiotic treatment, slowing pathogens' adaptive response.

More quantitative studies are needed to better establish the evolutionary dynamics involved in QS-mediated cooperation and the impact of inhibition on different aspects of QS. For instance, the discussion above only considers QS effectors that are public goods. The evolutionary outcomes can be significantly different if the effectors are private goods, with each cell able to access only those goods it produces.[111] and may be species-specific[112]. The same challenge is applicable for the population and evolutionary dynamics of other mechanisms leading to CAT. To this end, the use of well-defined model systems[113], both natural[25,111,114,115] and engineered[46,75,112], will be valuable for the development of better quantitative understanding of a population's response to antibiotics. This understanding can serve as the critical foundation to design 'evolution proof' treatment strategies that select against resistance[116].

Although antibiotic resistance has been well studied, predicting long term consequences on bacterial dynamics has proved elusive. Bacteria have already developed strategies to survive QS inhibition[106] and combination treatments involving Bla inhibitors[83], and will likely develop strategies to survive other inhibition methods.

Bacteria will constantly evolve to withstand antibiotic treatment; however, a better understanding of bacterial population and evolutionary dynamics under different treatment strategies can help us optimize treatment strategy.

1.6 Mathematical modeling in systems biology

Systems biology seeks to develop in-depth understandings of genotypic and phenotypic networks to explain natural behavior[117]. Increasingly, mathematical models are used to aid in achieving this goal, and generate testable predictions that validate their usefulness. These models take advantage of experimental data to constrain parameter values and describe potential interactions; this is often an iterative process, wherein experiments suggest a particular construction, and validation of model predictions leads to streamlining of the model itself.

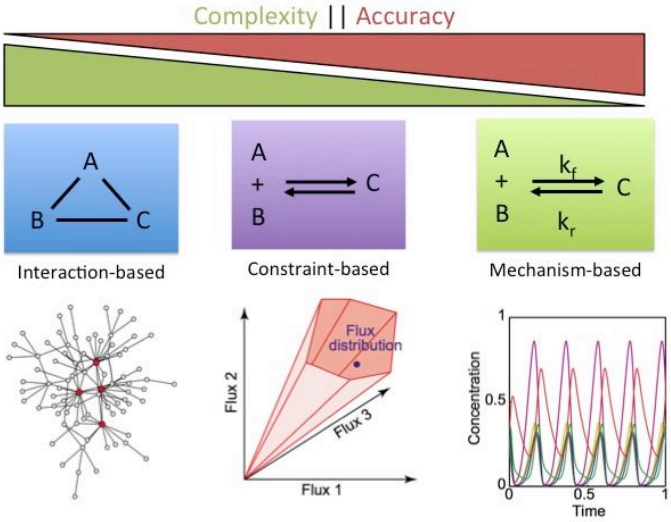

Figure 6: Mathematical representations of cellular networks. Mathematical models can be based on interactions alone (blue panel), constraints (purple panel), or mechanisms (green panel). Interaction-based models consist of various components (hubs) and their correlations (edges); constraint-based models consist of flux distributions calculated from reaction pathways; mechanism-based models track the time series evolution of components of interest. These three types of models fall on a continuum, progressively sacrificing scope/complexity in favor of detail/accuracy. Figure redrawn from[118].

Depending on the scope of analysis, a variety of models can be used to describe a phenomenon of interest[118]. For example, interaction-based models (Figure 6**, blue panel**) illustrate the connections between different components of interest; these are often represented by nodes in a map, where interactions between components are denoted as connecting edges. This type of representation is particularly useful in –omics analyses, which typically track expression levels (DNA, RNA, protein, etc) of many genes. Interaction-based models are useful in that they can reveal clusters of nodes that are

correlated; this can lead to inferences of conserved subnetworks, or suggest nodes that are non-essential. However, these networks do not involve any stoichiometry or quantitative rate parameters; it is often difficult to make conclusions beyond the power of correlation. A second modeling approach, constraint-based modeling (Figure 6**, purple panel**), begins to add this level of detail by specifying (or assuming) stoichiometric relationships between components. This type of model is often used in flux analyses; it is important to note that both interaction- and constraint-based models do not take history into account. That is, they take into account only amounts (e.g. concentrations, gene expression levels, etc.) without describing the time series trajectories that components follow. However, temporal dynamics are often vital to describing and understanding biological phenomena; mechanism-based models (Figure 6**, green panel**) attempt to use both stoichiometry and rate constants to be able to describe networks on a temporal basis as well.

Regardless of the specific network, mathematical models are inherently abstractions of the biological networks they seek to represent. No model will fully capture every interaction with quantitative certainty, and must make a tradeoff between complexity and accuracy; from interaction-based models to constraint-based to mechanism-based, scope is sacrificed from increasing levels of detail and accuracy; the

converse is true in the opposite direction. However, mathematical models do offer a number of advantages to the biologist, including:

Abstraction: It is not necessary to have detailed knowledge of every interaction. Often a "black box" approach, assuming a given input/output relationship. This encourages the development of minimal, easily understood models that remain sufficient to explain a behavior of interest.

Modularity: Models can often be combined to expand the scope of analyses.

Sensitivity: stability analysis, perturbation studies, dose response, and other trends can be easily investigated.

1.7 Microfluidic approaches to antibiotic resistance

Historically, microbial growth and drug response has been investigated using a number of bulk methods. Disk diffusion assays, counting colony-forming units (CFUs), and more latterly, microplate experiments are a mainstay of many systems and synthetic biology laboratories, and each have notable advantages. Disk diffusion assays, in which antibiotics are placed on a lawn of bacteria, resulting in zones of inhibition, are the standard method for determining minimal inhibitory concentrations (MIC)[119]. CFU counting gives a very precise measure of cell density; microplate experiments are useful in collecting longterm population level data, e.g. growth rates, protein expression, etc.

However, these methods all suffer from a number of common disadvantages: broadly speaking, they are resource/time-intensive, require a relatively large amount of labor, are prone to error/inconsistency, and are not amenable to parallelization.

Microfluidic platforms, designed on the micro- to pico- scale address each of these drawbacks, and are rapidly becoming indispensable to the field of biology. By enabling miniaturization, automation, and integration, microfluidics led to orders of magnitude improvements in the efficiency and throughput of standard reactions, including PCR, nucleic acid synthesis/amplification, and cell sorting[120]. They are less expensive, less reagent/time-intensive, and offer high throughput parallelization and sensitivity. Initially utilized in the 1980s, the applicability of mirocluidics to systems and synthetic biology took off with the development of soft polymer lithography, beginning in the 1990s[121]. Typically, microfluidic chips are first designed in a CAD environment; a mold is then created by spin-coating a photoactive polymer, e.g. SU-8, onto a base wafer, typically made of silicon. The polymer is then UV-crosslinked, and the masked, uncrosslinked portions are chemically washed, yielding a mold that is essentially the reverse of the final chip. A polymer of choice is then poured over this mold, degassed, and crosslinked under high temperature conditions. The most population option is (poly)dimethylsiloxane (PDMS), an elastomer that is transparent, biocompatible, and

easily manipulated[121]. After cutting the chip to size, inflow and outflow ports can be punched manually.

In addition to throughput and resource consumption advantages, microfluidic platforms enable analyses on the both the population and single cell level[122,123], and under precisely controlled environmental conditions. By integrating PDMS chips with time-lapse microscopy, I simultaneously gain the advantages of microplate readers (long term measurements) and flow cytometry (population distribution data). Increasingly, microfluidic platforms are being applied to investigate antibiotic resistance[124,125], including investigations of phenotypic changes[126] and persistence[24]. Moreover, microfluidic devices can be used as long-term chemostats[127].

1.8 Conclusions

Bacterial resistance and tolerance to antibiotic treatment is re-emerging as a global health concern; this issue is aggravated by the lack of novel antibiotic development. In addition to genetic mutation, bacteria use a multitude of population-level behaviors to withstand drug treatment; there is a vital need to develop a detailed understanding of these mechanisms. In doing so, I may be able to develop more

effective strategies to counteract bacterial survival, thereby extending the usefulness of current antibiotics.

1.9 Acknowledgements

This chapter includes material from Meredith HR*, Srimani JK*, et al "Collective antibiotic tolerance: mechanisms, dynamics and intervention", *Nature Chemical Biology* **11(3)** (2015).

2. Introduction

2.1 Postantibiotic effect (PAE): definition and prevalence

The discovery of penicillin in the 1920s[4] heralded a golden period of rapid antibiotic development. It was even suggested that infectious diseases could soon be a thing of the past[128]. However, as discussed in the preceding chapter, although antibiotics are one of the greatest medical breakthroughs in modern medicine, they face an emergent issue of resistance and tolerance, which can rapidly render them ineffective. While resistance develops when individual cells acquire beneficial random mutations, tolerance often arises through non-inherited mechanisms, including titration[129], persister cells[130], and drug-degrading secreted enzymes[71]. Indeed, resistance emerges faster than new drugs can be developed, leading many to wonder whether I are returning to the "dark ages" of the pre-antibiotic era[131]. Addressing the antibiotic crisis requires two complementary strategies. One is to develop novel drugs and therapeutic methods to combat bacterial infections. It is equally critical to develop effective antibiotic treatment protocols that can extend the efficacy of existing antibiotics.

Because antibiotic tolerance often arises through cooperative and phenotypic strategies, it is vital to develop a detailed mechanistic understanding of long-term bacterial dynamics in response to antibiotic treatment. This is applicable not only to developing novel drug targets and molecules, but more importantly to the design of

more effective treatment regimens. One intriguing and vital phenomenon that arises from antibiotic-treated microbial populations is the **postantibiotic effect (PAE)**, which refers to the temporary suppression of bacterial growth following transient exposure to antibiotics. This transient inhibition has been observed since the first studies of penicillin in against *Pneumococcus* and *Streptococcus* in the 1940s; when antibiotic action was halted with penicillinase, populations exhibited a significant lag before resuming growth[132-135]. Since this initial description, many subsequent studies have demonstrated that PAE can be induced by a variety of antibiotics, including aminoglycosides[136], beta-lactams[137,138], fluoroquinolones[139,140], and others[141,142], and against both Gram-positive and negative bacterial species[143-145]. PAE has also been observed in animal models[146,147], where, in addition to suppressing growth, transient antibiotic treatment can render the surviving population more susceptible to innate immune responses and result in decreased virulence expression[134].

These findings underscore the importance of PAE in the design and optimization of periodic and multi-dose antibiotic regimens[145,148]; indeed, previous studies have argued that bacterial population dynamics are equally as important as pharmacokinetic/pharmacodynamic (PK/PD) considerations in determining treatment efficacy[148]. In particular, suppression of recovery suggests that optimized protocols could effectively inhibit pathogens while requiring a smaller amount of drug. Reduced

antibiotic usage is advantageous in that it reduces both perturbation to the native microbiota[149-151] and exerts less selection pressure that can potentially drive the emergence of new genetic antibiotic resistance[152,153]. Accordingly, PAE is a standard metric used to evaluate novel antibiotics[154].

Despite widespread observations of PAE, its underlying mechanisms are not well established. Previous studies have speculated on a number of possible explanations, including non-specific binding and nonlethal damage induced by antibiotic treatment[155,156], antibiotic persistence within the periplasmic space, or the re-synthesis of essential enzymes[157]. Moreover, these studies have not ruled out the possibility of multiple concurrent mechanisms, or different mechanisms being applicable for different antibiotics. More recently, zur Wiesch and colleagues proposed that antibiotic-target binding kinetics are sufficient to explain PAE[158]; however, their model relies on effective antibiotic dilution via cell division. Given that many, if not all, antibiotics lead to PAE, I wondered if there exists an underlying motif that dictates the timescale of bacterial recovery. In this study, I propose that a minimal unifying titration-based interaction is sufficient to account for PAE observed in response to a wide variety of antibiotics. Moreover, I propose that PAE itself is a predictive metric for the efficacy of multi-dose antibiotic treatment regimens.

2.2 Premise

To quantify population recovery dynamics, I first defined population recovery time (RT_{pop}) as the doubling time relative to the end of antibiotic treatment (Figure 7**, left panel**). PAE, then, corresponds to the prolonged recovery time in response to antibiotic treatment, as compared to the control (Figure 7**, right panel**). In the absence of PAE, populations would resume normal growth immediately after the antibiotic was removed; the corresponding recovery time would be independent of the antibiotic treatment. This metric is preferable to historical definitions of PAE, which measured the time required for a population to increase 10-fold after treatment via counting colony-forming units (CFU)[144]; by measuring 2-fold increases in cell density, this metric more precisely captures the effect of any transient dynamics induced by antibiotic treatment.

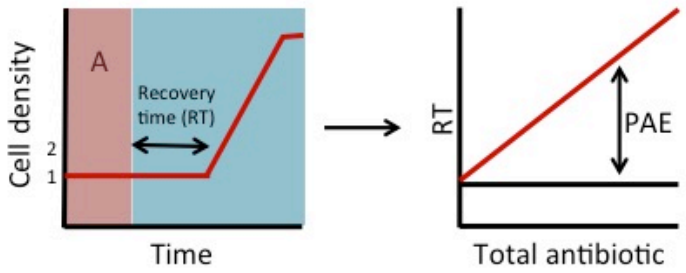

Figure 7: (Left panel) Recovery time is defined as the time required for a population (red line) to double in response to a transient antibiotic treatment (red shading). (Right panel) The postantibiotic effect (PAE) induced by an antibiotic treatment refers to the additional time required for a population to recover (red line) in comparison to the untreated control (black line).

2.3 Results

2.3.1 A microfluidic platform for high throughput quantification of PAE

In addition to potentially masking recovery dynamics on short time scales, previous studies of PAE (including those quantifying recovery by measuring rates of ATP synthesis[137], DNA and protein synthesis[159]) suffer from a common disadvantage: due to sparse time series data, they do not yield temporally precise estimates of recovery time. Moreover, they rely on relatively large populations of cells, which could potentially lead to inoculum effects and skew recovery dynamics[160]. To overcome these technical limitations, I collaborated with Dr. Shuqiang Huang, who previously developed a high throughput microfluidic platform, to quantify the response of bacterial populations to a range of antibiotic concentrations and treatment durations[161]. As shown in Figure 8**A**, the microfluidic chip consists of six independent channels (top row, top view), each with two media inputs (green circles) and one output (red circle). Bacteria are manually loaded into each channel and trapped in individual cylindrical culturing chambers (middle row). The height of the chambers (~1.0μm) constrains bacterial growth to a single monolayer, facilitating precise quantification (bottom row) using time-lapse fluorescence microscopy. Growth media and antibiotic dosing protocols are controlled by programmable syringe pumps.

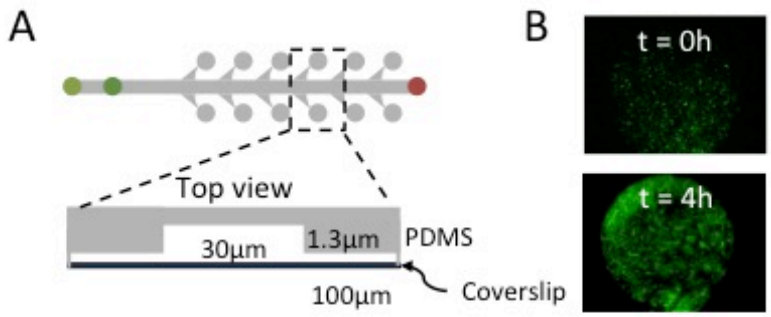

Figure 8: A high throughput microfluidic platform for quantifying bacterial population dynamics. A. Each PDMS-fabricated chip consists of six independent experiments, one of which is shown, from top view (top row). Green circles indicate media inflow; red circle indicates outflow. Bacteria are manually loaded in inflow ports and are trapped in individual culturing chambers (gray circles), the height of which ensures that bacteria are imaged in a monolayer (second row schematic). Growth conditions (e.g. antibiotic dose profile) are precisely controlled via externally programmable syringe pumps. B. Fluorescent images show representative growth of a monolayer of *E. coli* BW25113 cells constitutively expressing GFP over four hours.

Briefly, microfluidic chips were fabricated with polydimethylsiloxane (PDMS) using a silicon mold. Each chip is comprised of six parallel replicate units, each consists of a central flow channel and 24 branched culturing chambers. The height of these chambers (~1.3μm) traps a monolayer of bacterial cells, thereby enabling accurate image processing and population quantification. Each flow channel has two inputs and one output; by controlling media conditions (flow rate, antibiotic concentration) using externally programmed syringe pumps (New Era Pump Systems NE-1600), various antibiotic dose profiles can be implemented.

Overnight cultures were diluted 100-fold into 3mL M9 and grown for 2 hours at 37°C at 250rpm shaking (OD_{600} ~ 0.2). Cells were then condensed 10-fold. Cells were manually loaded into the chip using a P2 pipet. Media flow in the chip was controlled with external syringe pumps. Cells were allowed to grow for 30 minutes in clean media flow (no antibiotics, 120μL/h flow rate), followed by antibiotic treatment (500μL/h with applicable antibiotic concentration) and a recovery phase (no antibiotics, 120μL/h flow rate). These flow rates were chosen such to satisfy two conditions: slow enough so as not to wash out cells from the culturing chambers, and fast enough to observe significant inhibition over the typical course of an experiments (~18h). The entire device was kept at 37°C; five replicates were used per experimental condition. Culturing chambers were imaged every 5 minutes (Figure 8**B**). All experiments followed three phases: cells were initially cultured in media without antibiotic for 30 minutes, followed by media containing antibiotic for a fixed time interval, and then allowed to recover in antibiotic-free conditions.

2.3.2. Quantification of PAE in E. coli cells in response to streptomycin treatment

I used the microfluidic platform to first quantify the recovery dynamics of *Escherichia coli* strain BW25113[162] in response to transient streptomycin treatment. Overnight monoclonal cultures were diluted 100-fold into 3mL M9 and grown for 2 hours at 37°C at 250rpm shaking (OD_{600} ~ 0.2). Cells were then condensed 10-fold. Cells

were manually loaded into the chip using a P2 pipet. Media flow in the chip was controlled with external syringe pumps. Cells were allowed to grow for 30 minutes in clean media flow (no antibiotics, 120μL/h flow rate), followed by antibiotic treatment (500 μL/h with applicable antibiotic concentration) and a recovery phase (no antibiotics, 120μL/h flow rate). The entire device was kept at 37°C; five replicates were used per experimental condition. Culturing chambers were imaged every 5 minutes. All experiments followed three phases: cells were initially cultured in media without antibiotic for 30 minutes, followed by media containing antibiotic for a fixed time interval, and then allowed to recover in antibiotic-free conditions.

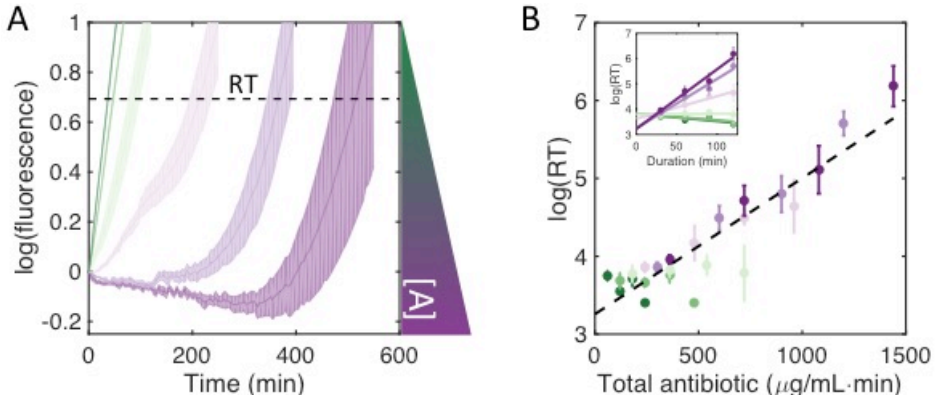

Figure 9: Population recovery time is a function of total antibiotic. A. Representative time series fluorescence data showing dose-dependent population recovery in response to transient streptomycin treatment. Here, time zero is relative to the end of treatment (120 minutes). Trajectories show mean and standard deviation for five replicates; colors indicate increasing antibiotic concentration (2, 4, 6, 8, 10, 12 μg/mL). Population fluorescence values are normalized to time zero; dotted line indicates a 2-fold increase, corresponding to the recovery time for each population. B. Population recovery time is an exponentially increasing function of total antibiotic treatment. Inset shows recovery time as a function of dose duration for increasing

streptomycin concentrations (as in panel C). When plotted against total antibiotic (calculated as $\int_0^{U} A(t)dt$), all recovery time values collapse onto a single exponential function (black line, $R^2 = 0.83$).

Figure 9**A** shows typical time courses of *Escherichia coli* strain BW25113[162] exposed to 120-minute streptomycin treatment at increasing concentrations (t=0 corresponds to the end of treatment). The recovery time drastically increased with increasing antibiotic concentrations, indicating generation of PAE, where the dashed line indicates a two-fold increase relative to t=0. At a fixed concentration, the recovery time drastically increased with treatment duration (Figure 9**B, inset**). Remarkably, by combining the dose and duration for each treatment, I found that the recovery time was determined by the total antibiotic delivered for each treatment, regardless of the dose profile (Figure 9**B**). That is, every treatment (i.e. combination of concentration and duration) that delivered a given total antibiotic resulted in a comparable recovery time, which increased approximately exponentially with the total antibiotic.

2.3.3 Partial population death and phenotypic selection do not account for PAE

Here, I note that a major caveat of using fluorescence reporters in the microfluidic platform is the effect of incomplete population death during antibiotic treatment. Indeed, under some treatment conditions, I observed cells that expressed GFP at comparable levels to other population members but did not divide for the duration of

the recovery phase (~18h). Therefore, although these cells contribute to total fluorescence, they do not contribute to recovery, and should therefore be disregarded from recovery time quantification.

To quantify the concentration-dependent killing rate of streptomycin, overnight cultures were regrown to mid-exponential phase by 100-fold dilution in 3mL M9 media and incubating for 2 hours at 37°C with 250RPM shaking. Cells were then washed and resuspended in a minimal M9 buffer (identical to M9 media described above, without glucose or casamino content). 500μL aliquots in 1.5mL Eppendorf tubes were incubated with appropriate antibiotic concentrations at 37°C with 250RPM shaking. Samples were then serially diluted to 10^7-fold and plated on selecting agar plates (50μg/mL kanamycin). Plates were incubated at 37°C overnight and CFUs counted the next day. Cell density was also measured prior to antibiotic treatment (~7E8 CFU/mL). Viability curves for each streptomycin concentration were normalized to initial densities and fit with exponential decay curves (Figure 10**A**). All data points show the mean and standard deviation of 6 replicates.

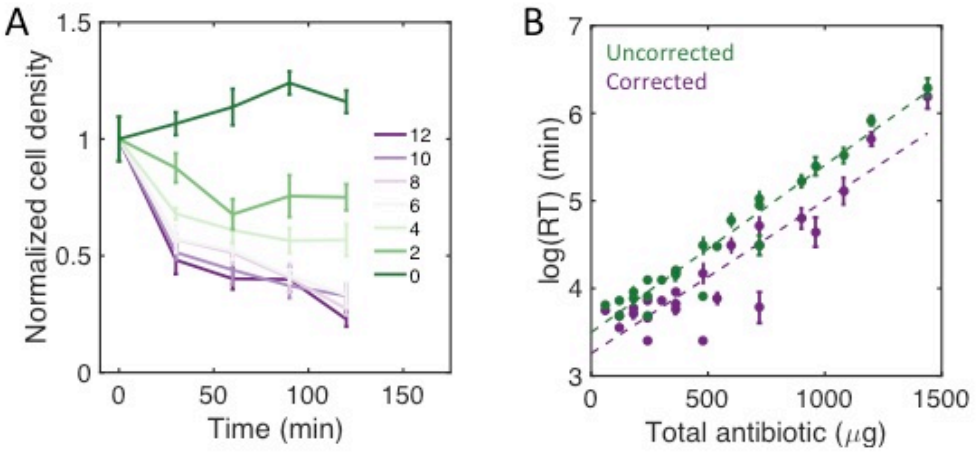

Figure 10: Partial population death does not account for antibiotic dependent recovery time. A. Concentration dependent streptomycin killing rates were determined in the absence of population growth. Overnight cultures were diluted 10-fold and grown in M9 media to a high density. Cells were then incubated in minimal media with the indicated antibiotic concentration for increasing durations. Population viability decreased exponentially with dose duration. The control population showed negligible growth/death in these conditions, indicating that decrease in viability is due to cell killing. All data points show mean and standard deviation of 6 replicates. B. Correcting for partial population death results in a lower effective recovery time (purple data points); however, recovery time remains dependent on total antibiotic.

These death rates were used to adjust the two-fold increase cutoff to reflect the only the fluorescence signal detected from actively proliferating cells. However, this adjustment did not account for the observed PAE; populations still exhibited a history-dependent response to drug treatment (Figure 10B). For example, treating with 12μg/mL streptomycin for 120 minutes resulted in approximately 40% viability (kill rate of 0.6). Therefore, the viable subpopulation would have doubled when the total fluorescence reached $2(1-0.6)+0.6=2-0.6=1.4x$ the total at the end of antibiotic treatment.

Moreover, It is well-established that treatment with subinhibitory antibiotic concentrations can lead to selection effects, wherein individual cells with lower minimum inhibitory concentrations (MIC) are eliminated, resulting in a post-treatment population with increased tolerance to antibiotic[153,163]. Typically, higher tolerance correlates with slower growth, due to reduced antibiotic uptake[164]. Indeed, such phenotypic selection can lead prolonged persistence under continuous treatment[163].

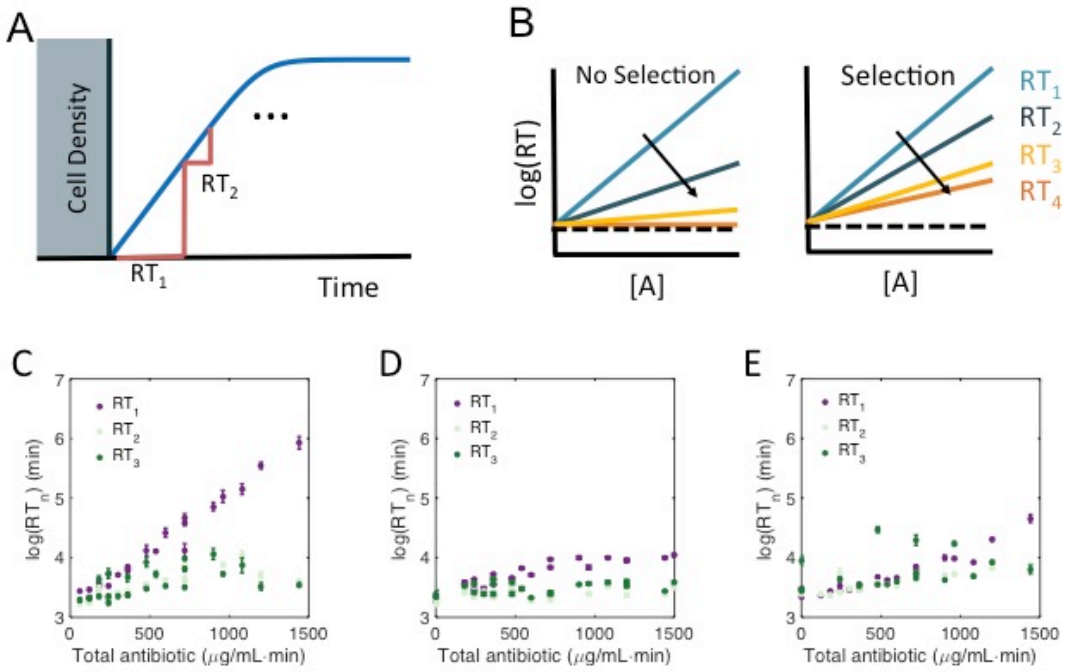

Figure 11: Successive doubling times suggest no phenotypic selection. A. Successive doubling times are defined as the time intervals over which a population increases 2-fold, and can be calculated from individual recovery trajectories, relative to the end of the dose (red shading). Here, the nth doubling time is denoted RT_n. Thus, RT_1 is identical to the recovery time data presented in Figure 1D. The extent of RT_n is limited by the size of the growth environment and data acquisition. B. Convergence

of RT_n suggests the presence or absence of antibiotic-dependent selection effects. In the absence of selection, RT_n would converge to zero slope, indicating that treatment history had no effect on growth dynamics after detoxification; after recovery from antibiotic treatment, populations were indistinguishable from untreated control (left panel). In the presence of antibiotic selection, successive RT_n would converge to slope greater than zero, indicating a physiological "memory effect", aka selection. C. – E. Successive doubling times following streptomycin (C) chloramphenicol (D), and streptomycin treatment in 0.05% w/v casamino acid media converge to a flat line, suggesting that the effect of antibiotic selection is insignificant.

To determine whether selection was the driving force behind these observations of PAE, I compared successive doubling times as a function of antibiotic concentration (Figure 11**A**). In this case, RT_1 is identical to the results presented in Figure 9**D.** In the absence of significant phenotypic selection, I would expect RT_n to approach a horizontal line (Figure 11**B, left panel**); in other words, antibiotic treatment would have no effect on the phenotypic composition of the population after full recovery. On the other hand, in the presence of phenotypic selection, I would expect RT_n to converge to a positively-sloped line, and remain dependent on the treatment history (Figure 11**B, right panel**). As shown in Figure 11**C** (streptomycin treatment) and Figure 11**D** (chloramphenicol treatment), subsequent doubling times calculated from our microfluidic experiments tended toward a constant value independent of antibiotic, suggesting that selection plays a minimal role in setting delayed population recovery.

2.3.4 A minimal model of antibiotic action

To gain insight into both intracellular and population-level dynamics underlying recovery dynamics, I adopted a minimal model of aminoglycoside action[160] (Figure 12**A**). The model consists of six ordinary differential equations (ODEs) representing extracellular and intracellular antibiotic (A_{in} and A_{out}, respectively), ribosome synthesis (C), and a two-step pathway for antibiotic-mediated ribosome degradation (CA and CA'). Through transcription and translation, C is subject to a positive feedback loop. Finally, the ribosome concentration C sets the population growth rate μ[165].

$$\frac{d[C]}{dt} = \frac{k_1[C]}{V_1 + [C]} - k_f[C][A_{in}] - k_u[C] + k_b[CA] \tag{1}$$

$$\frac{d[A_{in}]}{dt} = k_{in}[A_{out}] - k_{out}[A_{in}] - k_f[C][A_{in}] + k_b[CA] + k_r[CA'] \tag{2}$$

$$[A_{out}] = A_0(1 - H(t - D)) \tag{3}$$

$$\frac{d[CA]}{dt} = k_f[C][A_{in}] - k_b[CA] \tag{4}$$

$$\frac{d[CA']}{dt} = k_d[CA] - k_r[CA'] \tag{5}$$

$$\frac{dN}{dt} = \mu_0\left(\frac{[C]}{V + [C]}\right)N\left(1 - \frac{N}{N_m}\right) \tag{6}$$

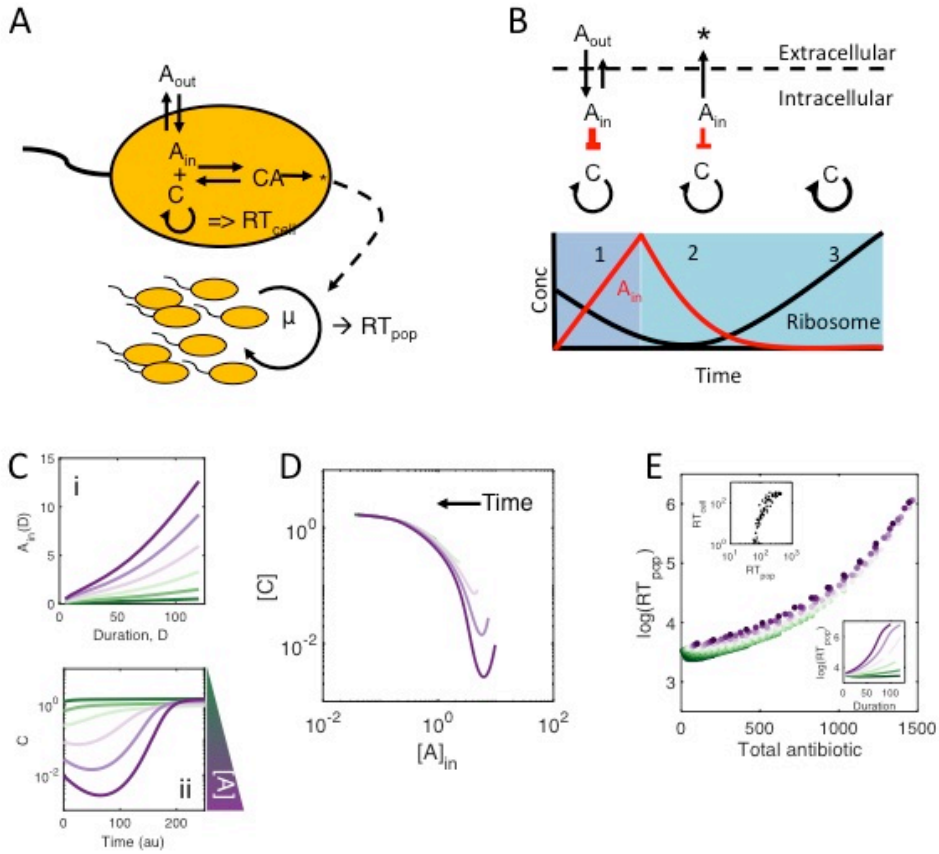

Figure 12: The timescale of intracellular antibiotic efflux dictates individual and population recovery. A. A minimal model of antibiotic action. Antibiotic is transported between the intracellular and extracellular environments (A_{in} and A_{out}) by influx and efflux rates (k_{in} and k_{out}). A_{in} reversibly binds to target ribosomes C to form the complex CA, with binding and dissociation rates k_f and k_b, respectively. This complex can then be degraded through the intermediate CA'. These intracellular dynamics influence the overall population recovery rate; the maximum growth rate μ is dependent on the ribosome concentration C. Thus, recovery can be quantified both on the individual level, as a function of C, or on the population level, in terms of cell density. B. Concurrent antibiotic transport and ribosome inhibition dictate recovery dynamics. During treatment, $A_{out} >> A_{in}$, and the intracellular antibiotic concentration can be linearly approximated by $A_{in}(D) = k_{in} A_{out} D$, where A_{out} is assumed to be constant and D represents the treatment duration (leftmost schematic and panel 1). Antibiotic influx is greater than efflux; A_{in} binds to target ribosomes and strongly inhibits the upregulation of ribosome synthesis. When extracellular antibiotic is removed, A_{in} decreases (middle and rightmost schematics and blue shading and

panels 2-3), and ribosome synthesis is dictated by positive feedback and efflux (panel 3). C. A_{in} accumulates linearly with treatment duration for sufficiently short treatment durations (panel i). After the removal of A_{out}, efflux and inhibition dynamics combine to delay the synthesis of ribosomes in a concentration-dependent manner (panel ii). Colors indicate increasing antibiotic concentration, as shown in panel ii. D. Antibiotic efflux timescale sets intracellular recovery RT_{cell}. Regardless of the antibiotic treatment history, the relationship between intracellelular antibiotic A_{in} and ribosome concentration C approaches the same asymptote, indicating that the timescale of individual detoxification sets the timescale of ribosome synthesis. Colors indicate increasing antibiotic concentration, as in Figure 2C-D; for these representative trajectories, treatment duration was set to 120 minutes. E. Population recovery time is dictated by total antibiotic delivered. Lower right inset shows that RTpop is an increasing function of dose duration; these data collapse onto a single relationship as a function of total antibiotic (main figure). Moreover, RT_{pop} and RT_{cell} are strongly correlated (upper left inset).

In this formulation, $[C]$ represents the free ribosome concentration, which is synthesized following Michaelis-Menten dynamics. Antibiotic shuttles between the extracellular ($[A_{out}]$) and intracellular ($[A_{in}]$) environment according to the rates of influx and efflux, k_{in} and k_{out}, respectively. Ribosomes reversibly bind to intracellular antibiotic (rates k_f and k_b) yielding the complex $[CA]$. This complex undergoes a two-step degradation process, releasing antibiotic to the intracellular concentration[166-168]. k_u represents the basal rate of ribosome turnover. Finally, the maximum population growth rate μ_0 is scaled by the ribosome concentration[165]. All rate constants used are listed in Table 1. For transient dosing simulations (Equation 3), I assumed that the extracellular antibiotic concentration A_0 did not significantly decreasing during the dosing interval

D. Here, the term $1-H(t-D)$ represents a Heaviside step function that implements a rectangular dose with arbitrary duration.

Table 1: Full ODE model parameter values

Parameter	Description	Value
k_1	Synthesis rate constant of [C]	0.2 [μMmin^{-1}]
k_f	Binding rate constant	2.5 [μM^{-1}min^{-1}]
k_b	Dissociation rate constant	1.5 [min^{-1}]
k_{in}	Influx rate constant	7e-3 [min^{-1}]
k_{out}	Efflux rate constant	1e-2 [min^{-1}]
k_d	Antibiotic-mediated ribosome inactivation rate constant	0.1 [min^{-1}]
k_r	Antibiotic-mediated ribosome turnover rate constant	0.02 [min^{-1}]
k_u	Intrinsic ribosome turnover rate constant	0.1 [min^{-1}]

Thus, I assume homogenous populations that interact (i.e. drug influx and efflux) with a common extracellular environment. Because the population growth rate is dependent on the ribosome concentration, I can investigate recovery on two scales: on the population level (RT_{pop}, analogous to Figure 9**B**) as the time required for the cell number to double, and on the individual level, as the time required for the ribosome concentration to achieve its half maximal synthesis rate (RT_{cell}).

Figure 12B shows the typical dynamics of various components, in three phases, in response to the addition and removal of an extracellular antibiotic. During antibiotic

treatment (Figure 12**B, left schematic and blue shading**), $A_{out} >> A_{in}$ and the dominant component dynamic is the accumulation of intracellular antibiotic due to influx. Neglecting the efflux dynamics and titration due to binding of antibiotic to the ribosome, I have: $A_{in}(D) = \frac{k_{in}}{k_{out}}[A_{out}]\left(1 - e^{-k_{out}D}\right) \approx k_{in}[A_{out}]D$ (for sufficiently small D). That is, at the end of an antibiotic pulse, *the intracellular antibiotic concentration is proportional to total amount of the antibiotic used* (Figure 12**C, panel i**), consistent with previous studies[164,169-172].

Upon removal of the antibiotic, $A_{in} >> A_{out} = 0$ and the transport dynamics of the antibiotic are dominated by efflux (Figure 12**B, middle schematic and green shading**). In addition to efflux, binding kinetics between ribosome and antibiotic serve as an intracellular reservoir for A_{in}, and can further delay recovery. If the cell survives treatment, it can revert to a basal growth rate when it is sufficiently detoxified (i.e., when A_{in} is sufficiently small to not inhibit the ribosome effectively) (Figure 12**C, panel ii**). The balance between these three processes (efflux, binding, and degradation) sets the time scale of detoxification and subsequent growth recovery; this time scale manifests itself as PAE. Consistent with this notion, for different dosing protocols, the correlations between C and A_{in} approximately collapse to a single line (Figure 12**D**). This

mechanism recaptures the dependence between population recovery time and total antibiotic (Figure 12**E, main and right inset**).

These results provide a simple explanation for the emergence of PAE: fundamentally, PAE arises as the time required for individual cells to recover by exporting antibiotic, such that ribosome-mediated positive feedback can be activated. This "detoxification" process occurs on the individual cell level, and intracellular recovery dynamics correlate strongly with population recovery, assuming exponential cell growth (Figure 12**E, left inset**). Under the simplifying assumption that extracellular antibiotic is negligible during recovery, individual cells in a given population remain independent of each other; detoxification dynamics in a given cell do not affect any of its neighbors. Therefore, it is unnecessary to incorporate the effects of distributional biochemical noise in our model.

Thus far, in all experiments and simulations I have examined population recovery in response to rectangular doses. However, if recovery time is set by total antibiotic alone, I would expect this idea to hold in the face of arbitrary dose profiles. I used modeling to confirm this idea. Specifically, I investigated both triangular (Figure 13A) and exponentially decaying dose profiles (Figure 13B); our results show that

recovery time remains a function of total antibiotic, regardless of the manner in which it was delivered.

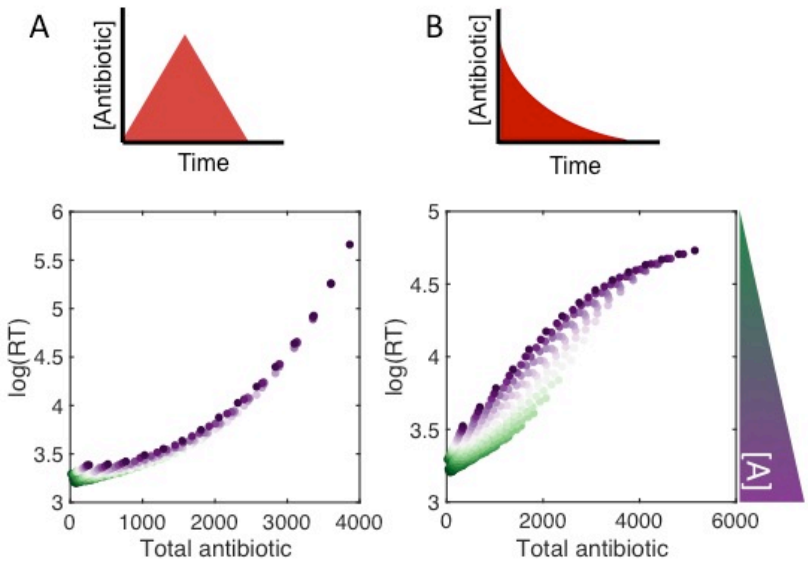

Figure 13: Recovery time remains a function of total antibiotic delivered, regardless of dose profile. Here, I simulated triangular (A) and exponentially decaying dose profiles (B), over the same range of treatment conditions. Population recovery times collapsed reliably as a function of total antibiotic.

2.3.5 Model validation: perturbation studies

I next sought to validate this minimal model by perturbing the key component processes (efflux, ribosome degradation, and ribosome synthesis). As shown in **Figure 3A-C**, decreasing the antibiotic-mediated degradation rate, increasing the efflux rate, or increasing ribosome synthesis rate all lead to more rapid recovery, while maintaining the dependence on total antibiotic.

To investigate the effect of ribosome degradation, I compared the recovery time induced by streptomycin, which has been shown to induce the heat shock response (HSR) and lead to rapid ribosome degradation, to chloramphenicol, which does not induce HSR[160]. As predicted, chloramphenicol treatment resulted in significantly shorter recovery time than streptomycin treatment (Figure 14A/D show modeling and experimental results, respectively).

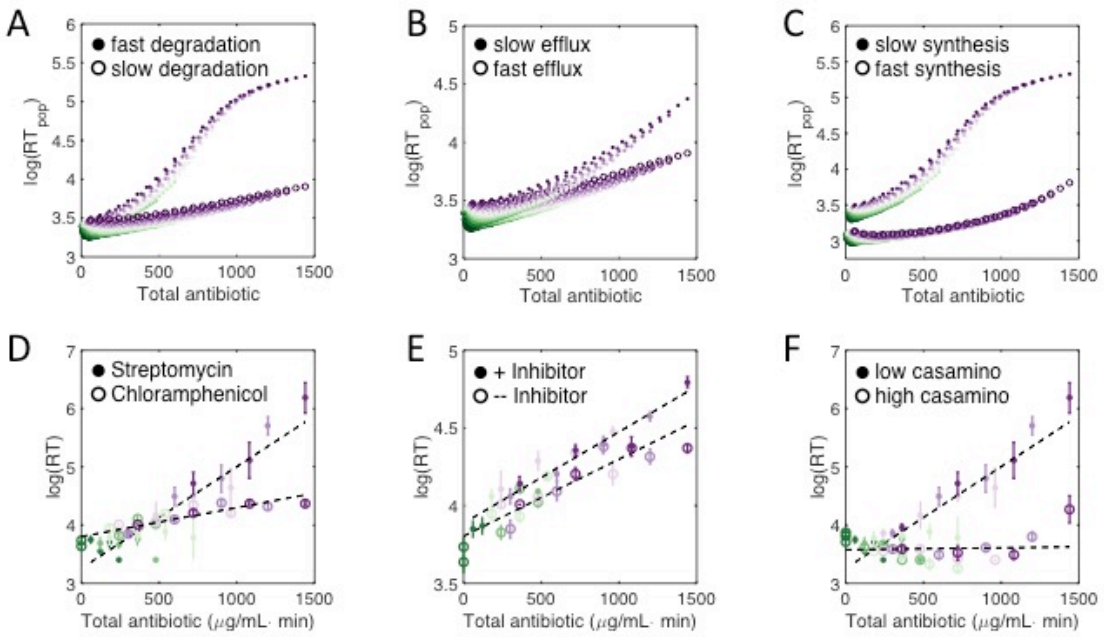

Figure 14: Key parameter perturbations confirm model validity. A. Modeling indicates that decreasing the ribosome degradation rate leads to shorter recovery times in response to equal amounts of total antibiotic. B. Modeling indicates that decreasing the antibiotic efflux rate leads to longer recovery times in response to equal amounts of total antibiotic. C. Modeling indicates that increasing the ribosome synthesis rate leads to shorter recovery times in response to equal amounts of total

antibiotic. D. Streptomycin treatment (closed data points, R^2 = 0.83), which induces heat shock response (HSR) and rapid ribosome degradation, results in significantly longer recovery times than chloramphenicol treatment (open data points). Here, the two responses are statistically significant ($p<0.05$ by ANOVA). E. The addition of efflux pump inhibitor (CCCP) (closed data points, R^2 = 0.91) increases population recovery time in response to chloramphenicol treatment (open data points, R^2 = 0.80). Here, CCCP was added at subinhibitory concentrations (3μg/mL); in the absence of antibiotic treatment, CCCP alone did not inhibit population recovery. The CCCP-mediated increase in recovery time is statistically significant ($p < 0.01$). F. The ribosome synthesis rate was increased by enriching the casamino content of the media from 0.01% w/v (closed data points) to 0.05% w/v (opendata points). Faster synthesis resulted in lower recovery times ($p<0.001$). In each of these panels, the color scheme indicates increasing antibiotic concentration, as in Figure 1C.

We next modulated the antibiotic efflux rate using the small molecule inhibitor carbonyl cyanide 3-chlorophenylhydrazone (CCCP). I measured the effect of CCCP using an adapted ethidium bromide (EtBr)-based assay for efflux pump activity[173,174]. A phosphorylation inhibitor, CCCP has been shown to inhibit a variety of efflux pumps that rely on the proton motive force (PMF), including resistance nodulation division pumps and others[175-177]. At sub-toxic concentrations, ethidium bromide (EtBr) accumulates intracellularly, where it can be detected using plate reader fluorescence measurements (excitation/emission 488nm/590nm); previous studies have shown that this signal is significantly stronger intracellularly, as ethidium bromide binds to bacterial DNA. In this assay, I assumed that the influx of EtBr was not dose dependent; this allowed us to calculate the effective efflux rate based on EtBr accumulation dynamics in the presence of varying levels of CCCP. EtBr stock solution were prepared at 1 mg/mL

in water and stored at room temperature. To measure efflux in BW25113, overnight cultures were washed and diluted 50-fold into a minimal M9 buffer media (M9 as described above, without glucose or casamino acid); EtBr was added to a final concentration of 2μg/mL (IC_{50}>100μg/mL). CCCP stock solutions were prepared by dissolving CCCP in dimethyl sulfoxide (DMSO) to a final concentration of 1mg/mL and stored at 4°C. Cells were plated in 96-well glass bottom plates and covered with 50μL mineral oil to prevent evaporation. Intracellular EtBr signal and cell density (OD600) were measured every 10 minutes at 30°C. Fluorescence time courses were normalized to OD_{600}. Efflux rates were calculated assuming that intracellular EtBr concentration are dictated by the following equation:

$$\frac{dE}{dt} = k_{in}E_0 - k_{out}E \qquad (7)$$

Where E and E_0 represent the intracellular and extracellular EtBr concentrations, respectively. I assume E_0 to be constant. Thus, Equation 7 can be solved to yield:

$$E(t) - E(0) = c_1(e^{k_{out}t} - 1) \qquad (8)$$

Where c_1 represents a constant of integration. Thus, EtBr fluorescence time courses were background-corrected and normalized by OD_{600}. Curves were fit to Equation 8 to determine efflux rates. Figure 15B shows a dose dependent inhibition of intracellular EtBr accumulation in the absence of cell proliferation (Figure 15B, inset);

conditions that minimized cell growth were chosen to ensure that growth dynamics did not skew EtBr signal.

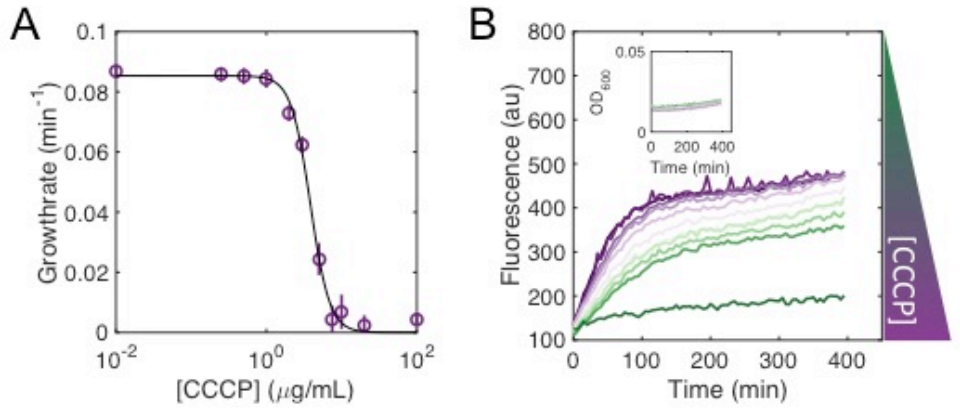

Figure 15: [CCCP] inhibits efflux pump activity in a dose-dependent manner. A. Dose response for carbonyl cyanide m-chlorophenyl hydrazine (CCCP). Seven logarithmically spaced concentrations were chosen, in addition to 0. Growth rates were calculated by log-transforming time series data and calculating the slope of the longest linear segment. Data points are the average of three replicates; black line shows the best fit Hill function (IC_{50} = 3.87μg/mL). B. CCCP increases ethidium bromide (EtBr) accumulation, and inhibits antibiotic efflux, in a dose-dependent fashion. A previously published protocol was used to measure the effect of CCCP on efflux pump activity, in the absence of growth. Intracellular EtBr, which acts as a general efflux pump substrate, can be measured via population fluorescence; accumulation is increased in the presence of increasing CCCP concentrations.

After demonstrating that subinhibitory levels of CCCP (Figure 15A) were sufficient to significantly inhibit efflux activity, I compared the recovery dynamics of BW25113 in the presence and absence of CCCP (3μg/mL) in the microfluidic platform, using chloramphenicol treatment. Our experimental results (Figure 14E) confirm

modeling predictions (Figure 14B); application of CCCP increased recovery times while maintaining the overall dependence on total antibiotic.

Finally, I modulated the ribosome synthesis rate by supplementing the growth media's casamino content[178]. In the presence of increased casamino content, corresponding to rapid ribosome synthesis, populations recovered significantly faster after antibiotic treatment (Figure 14**F**). Again, this was consistent with model predictions (Figure 14C). These computational and experimental results together suggest that our minimal motif of antibiotic action is sufficient to account for the observed dose dependent PAE.

2.3.6 Efficacy of efflux inhibition to diverse antibiotic mechanisms of action

These results suggest that drug response dynamics can be modulated to induce longer PAEs, which is advantageous from a clinical perspective[15,179,180]; antibiotic efflux inhibition is an active area of research[181,182]. In particular, resistance nodulation division (RND) pump systems are prevalent in Gram negative species and have been shown to efflux a variety of antibiotics, including penicillins and cephalosporins, macrolides, aminoglycosides, fluoroquinolones, and tetracyclines[17,183,184]. Moreover, many resistant strains have been shown to over-express these efflux pumps[185-187]. In this context, efflux pump inhibitors (EPIs) have emerged as potential adjuvants for antibiotic treatment;

recent studies have proposed a number of candidate EPIs, via both rational design[188] and natural isolation[189]; these are often based on studies of efflux pump structure, competitive binding, or disruption of transmembrane electrical gradients[190,191]. Intuitively, I would expect that efflux inhibition would be universally beneficial in lengthening PAEs in response to a given antibiotic treatment. However, these approaches have met with limited clinical success[192,193]; optimal co-treatment strategies remain an open question[194].

Therefore, I asked the question, under what conditions is efflux inhibition an effective strategy for extending PAE? I used modeling to examine the sensitivity of various parameters (e.g. ribosome degradation and synthesis rates, as well as positive feedback strength), and antibiotic motifs, to changes in efflux. I reasoned that the induction of PAE by antibiotic accumulation and detoxification dynamics (**Figure 2A**) is applicable to any drug that has an intracellular target (including those in the periplasm) (Figure 16). As such, I expect that qualitatively similar dynamics can lead to PAE for these other antibiotics, and may be sensitive to efflux inhibition.

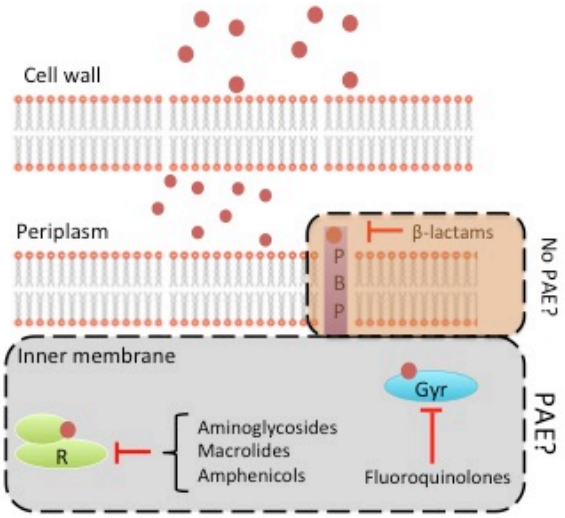

Figure 16: Antibiotics inhibit a variety of intracellular targets, including ribosome function and protein synthesis (e.g. aminoglycosides, amphenicols, and macrolides), DNA gyrase (e.g. fluoroquinolones) and penicillin-binding proteins (β-lactams). Previous studies have described PAEs to all of these classes of antibiotics, although some drugs induce minimal transient growth inhibition.

2.3.6.1 Computational modeling approaches

To quantify the effects of efflux inhibition, I define sensitivity as the total change in recovery time, over a range of antibiotic doses, in response to a change in efflux rate (Figure 17**A**). With this definition, I first examined the effect of efflux inhibition in conjunction with the drug-mediated ribosome degradation rate (Figure 17B). I observed that faster degradation resulted in increased efflux sensitivity. Similarly, I found that increasing the nonlinearity of the target positive feedback loop also increased efflux sensitivity (Figure 17**C**). These results suggest that efflux inhibition may not always be

an effective strategy to induce longer bacterial recovery, but rather need to be administered in conjunction with certain antibiotics that satisfy these constraints.

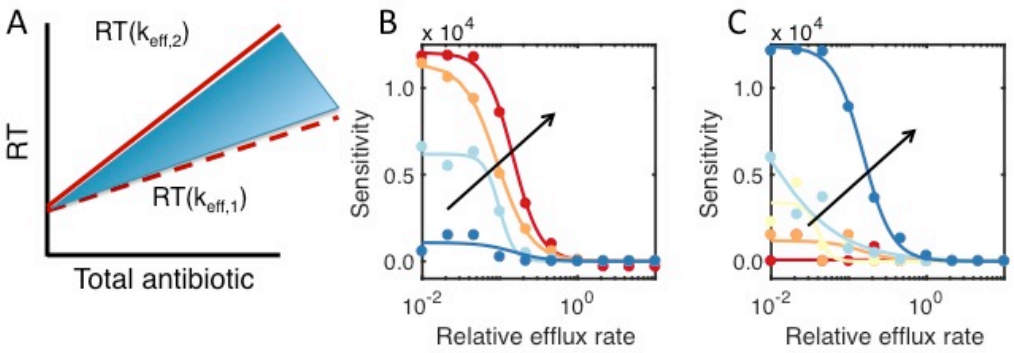

Figure 17: Populations are more sensitive to decreases in antibiotic efflux rate in conjunction with rapid target degradation and strong positive feedback in target synthesis. A. Sensitivity is defined as the total change in recovery time in response to a change in the antibiotic efflux rate. B-C. Each trajectory corresponds to one value of the target degradation rate (B, black arrow shows the direction of increasing parameter value) or feedback nonlinearity (C, arrow shows increasing direction). Sensitivity increased with high degradation and feedback nonlinearity, corresponding to the left motif in Figure 11A.

Thus far, in both experiment and modeling, I investigated PAE as induced by ribosome-binding antibiotics (e.g. streptomycin and chloramphenicol). However, an efflux-mediated recovery motif (Figure 12**A**) is theoretically applicable to any antibiotic mechanism of action, regardless of its putative target and inhibition dynamics (Figure 16); therefore, I would expect PAE to be a function of total antibiotic regardless of the antibiotic used. To test this hypothesis, I developed simplified kinetic models to investigate three scenarios, using the following set of equations.

Table 2: Simplified ODE model parameters

Parameter	Value	Description
k_0	1e-3 [μMmin^{-1}]	Constitutive synthesis rate constant of [T]
k_t	1e-2 [μMmin^{-1}]	Michaelis-Menten synthesis rate of [T]
K_T	0.5 [μM]	Half-maximal value of [T]
k_f	1 [μM^{-1}min^{-1}]	Antibiotic-target binding rate constant
k_b	1e-2 [min^{-1}]	Dissociation rate constant
d_t	1e-2 [min^{-1}]	Degradation rate of [T]
d_p	1e-3 [min^{-1}]	Degradation rate of antibiotic-target complex
k_{in}	0.1 [min^{-1}]	Antibiotic influx rate constant
k_{out}	1e-4 [min^{-1}]	Antibiotic efflux rate constant

We adopted a minimal set of ODEs capable of representing all three (Equations **9-11**, Table 2 shows parameter values used). Here, $[T]$ and $[A]$ represent the drug target and intracellular antibiotic concentration, respectively; $[P]$ represents the antibiotic-target binding product. k_0 represents the basal target synthesis rate, k_f and k_b represent the binding and dissociation rates between antibiotic and target, k_t and K_T represent the maximum synthesis and half-maximal values of $[T]$; d_T and d_P represent the degradation rates of target and antibiotic-target complex, respectively. Finally, A_{out} represents the extracellular antibiotic concentration during a dose, which I assume to be constant; k_{in} and k_{out} represent the influx and efflux rates across the cell membrane, respectively. By setting various parameters to zero, these equations can be used to compare diverse modes of action. Setting $k_0 = 0$ represents the motif inFigure

18A; setting $d_P = 0$ corresponds to the second (Figure 18B), and setting $d_P = 0 = k_t$ corresponds to the third (Figure 18C). As with the full model, intracellular recovery time was calculated as the time to achieve $\frac{1}{2} max\left(\frac{d[T]}{dt}\right)$ during recovery. All parameter values are listed in Table 2.

$$\frac{d[T]}{dt} = k_0 + \frac{k_t[T]}{K_T + [T]} - k_f[T][A] + k_b[P] - d_T[T] \tag{9}$$

$$\frac{d[A]}{dt} = k_{in}A_{out} - k_{out}A_{in} - k_f[T][A] - k_b[P] + d_p[P] \tag{10}$$

$$\frac{d[P]}{dt} = k_f[T][A] - k_b[P] - d_P[P] \tag{11}$$

Using this system I compared three motifs. In each case, the antibiotic is transported between the intracellular and extracellular spaces. In the intracellular space, the antibiotic binds to its target reversibly and the concentration of the free target indicates the viability of the cell. However, these different motifs differ in how the target is regulated. In the first motif, the target synthesis is driven by a positive feedback loop, and binding to the antibiotic leads to enhanced degradation of the target (Figure 18**A**). This motif accounts for antibiotics that target ribosome synthesis and induce fast ribosome degradation, such as streptomycin and kanamycin. The second motif is identical to the first except that the antibiotic does not enhance degradation of the target

(Figure 18**B**). This motif accounts for the action by chloramphenicol and tetracycline[160]. The third motif is identical to the second except that the target is synthesized at a constant rate, with no feedback (Figure 18**C**). This motif accounts for inhibition by β-lactams. For each of these motifs, recovery time (as measured by target synthesis rates, as above) was a function of total antibiotic; moreover, decreasing the efflux rate resulted in significantly longer recovery time for a given total amount, consistent with our previous modeling and experimental observations.

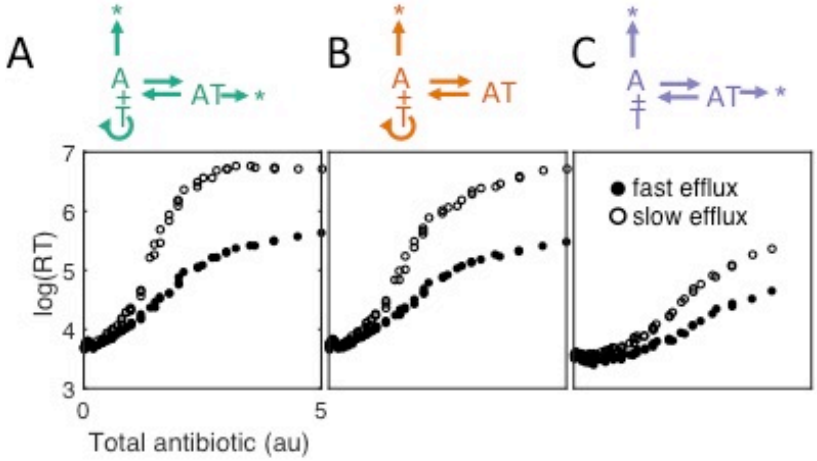

Figure 18: Efflux inhibition is an effective co-treatment strategy for certain antibiotics. A. Three general motifs of intracellular antibiotic action. Left and middle motifs correspond to ribosome-inhibiting antibiotics that induce rapid and minimal ribosome degradation, respectively. In these motifs, the target molecule is subject to nonlinear positive feedback (i.e. transcription and translation, in the case of ribosomes). Right motif corresponds to antibiotics that inhibit other targets that are not subject to positive feedback, e.g. β-lactams. In each case, recovery time is a function of total antibiotic, and is significantly lengthened by efflux inhibition. B. Populations are more sensitive to decreases in antibiotic efflux rate in conjunction with rapid target degradation and strong positive feedback in target synthesis. Sensitivity is defined as the total change in recovery time in response to a change in the antibiotic efflux rate (top panel). In panels i-ii, each trajectory corresponds to one value of the target degradation rate (panel i, black arrow shows the direction of

increasing parameter value) or feedback nonlinearity (panel ii, arrow shows increasing direction). Sensitivity increased with high degradation and feedback nonlinearity, corresponding to the left motif in Figure 11A.

2.3.6.2 Experimental validation

To confirm these predictions, I utilized a constitutively expressed luminescence reporter[195] to investigate the effect of several representative antibiotics encompassing most major classes *in vitro.* Bioluminescence is commonly used as an indicator of cell density, and is advantageous in that it tracks only viable cells[196], thereby bypassing the need to correct for cell death-induced population skew. In order to compare the effect of various antibiotics, I first determined their respective IC_{50} values. Single colonies were grown overnight as above and diluted 100-fold into M9 media. Antibiotic concentration gradients were created by serially diluting from 100 μg/mL, and included 0 μg/mL. Growth was measured in 96-well plates (Corning) with 200μL liquid per well; wells were covered with 50μL mineral oil (Sigma-Aldrich Chemicals) to prevent evaporation and density (OD_{600}) data was collected every 10 minutes using a Tecan M200 Infinite Pro plate reader at 37°C. IC_{50} values were determined by first calculating growth rates by iteratively finding the longest linear region of increase; these growth rates were then fit to a Hill equation, where μ_{max}, n, and A, are the maximum growth rates, Hill coefficient, and antibiotic concentration, respectively (Equation 12 and Figure 19).

$$\mu(A) = \frac{\mu_{max} IC^{n}_{50}}{IC^{n}_{50} + A^{n}} \qquad (12)$$

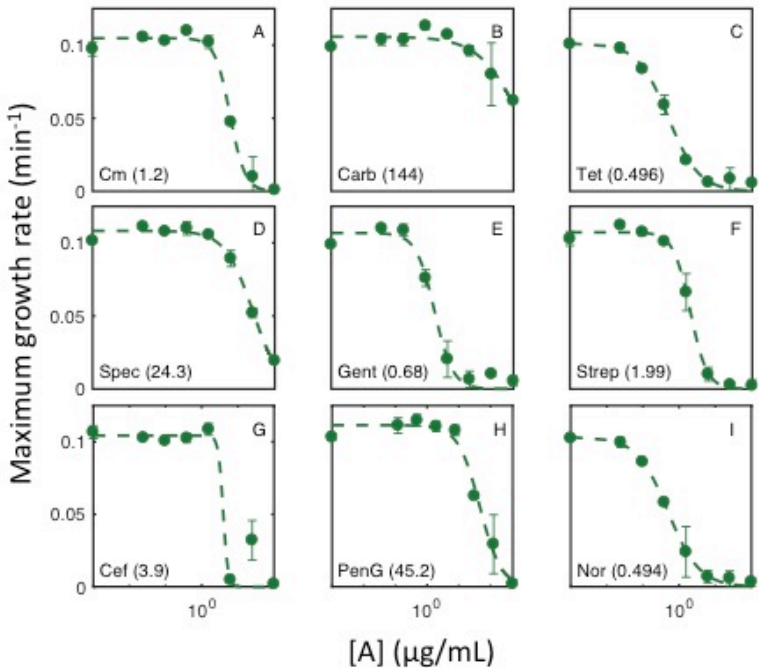

Figure 19: Determining IC_{50} values for various antibiotics. IC_{50} values were calculated from long-term dose responses in 96-well plates. For each antibiotic, seven logarithmically concentrations were tested, using serial dilution. Initial cell density was 100-fold dilution of overnight culture (~2e7 CFU/mL). Growth curves extending up to early stationary phase were collected; maximum growth rates were extracted by log-transforming the data and iteratively determining the longest linear portion. Each data point corresponds to the average of three technical replicates. IC50 values were determined by fitting growth rates to a Michaelis-Menten equation (dashed line), and are shown in each panel (µg/mL). Antibiotics tested are as follows: Chloramphenicol (panel A), carbenicillin (B), tetracycline (C), spectinomycin (D), gentamicin (E), streptomycin (F), cefotaxime (G), penicillin G (H), norfloxacin (I). IC50 values for each antibiotic are labeled in parentheses.

Overnight cultures were diluted 100-fold into M9 media supplemented with selection antibiotics. 1mL aliquots were apportioned in 1.5mL Eppendorf tubes and experimental antibiotic concentrations were added as appropriate. Cultures were incubated at 30°C with shaking at 250rpm for two hours; cells were then resuspended in

fresh M9 media containing only selection antibiotics. 200μL aliquots were transferred to black 96-well plates, and time course luminescence measurements were taken using a Tecan Infinite M200 Pro plate reader every 10 minutes. Three replicates were used per experimental condition, and only alternate wells were used on 96-well plates to avoid capturing luminescence signal from neighboring wells. Time series data were normalized to initial conditions and population doubling time was determined relative to the initial time point.

We tested a number of antibiotics (Figure 19) over the same range of IC_{50} values. Although the addition of CCCP increased the extent of PAE in all cases (Figure 20), this effect was most significant with the three aminoglycoside antibiotics (streptomycin, gentamicin, and spectinomycin), as compared to drugs that fell in either of the latter two motifs. These results confirm our modeling predictions; the three aforementioned antibiotics induce rapid ribosome degradation. Moreover, I observed minimal inhibition with the β-lactams penicillin G, carbenicillin, and cefotaxime, as suggested by sensitivity analysis.

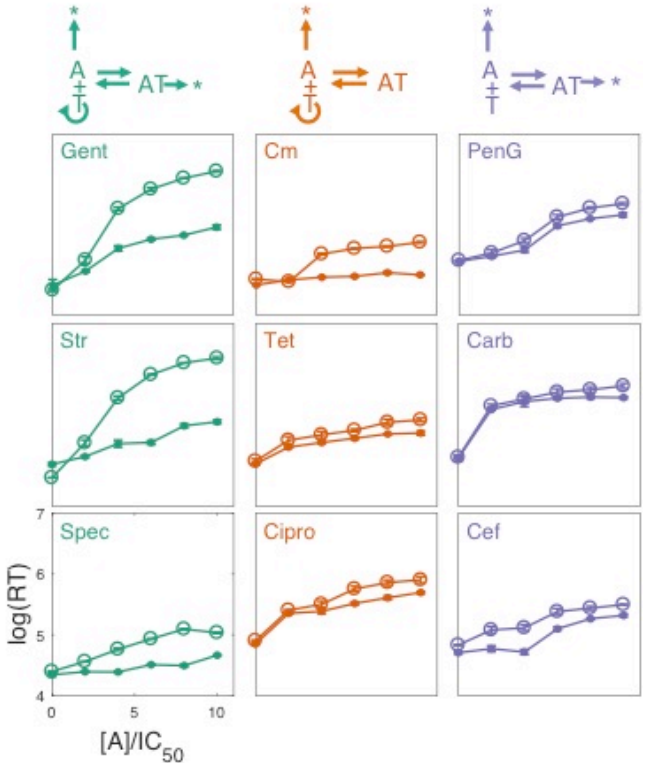

Figure 20: Inhibiting antibiotic efflux with CCCP significantly increased population recovery time in response to a wide variety of antibiotics (penicillin G (PenG), spectinomycin (Spec), gentamicin (Gent), streptomycin (Str), chloramphenicol (Cm), tetracyclin (Tet), and carbenicillin (Carb)). Here, the particular antibiotic concentrations used have been scaled by their respective IC_{50} values (solid points and open circles show response with no efflux inhibition and 2µg/mL CCCP, respectively).

2.4 Discussion

In general, there are two strategies to combat the rapid rise of drug-resistance microbial pathogens: novel antibiotic development, or more effective stewardship of existing drugs[15,197]. Given the prohibitive time and financial costs of the former, many studies have examined strategies to better use the antibiotics already at our disposal. In

doing so, it is important to move beyond steady-state measures of efficacy, e.g. IC_{50}, and emphasize the importance of temporal dynamics in drug response. PAE is one such response; our results suggest that a minimal but common motif is sufficient to account for this phenomenon in response to a wide variety of antibiotics. These results suggest that efflux-mediated recovery could be a unifying motif to explain PAE in response to a wide variety of antibiotics. This would tie together wide-ranging literature reports of PAE in many antibiotic/microbial combinations, without requiring distinct drug-dependent explanations.

Moreover, I show that efflux inhibition is a more effective strategy to induce PAE for certain antibiotic mechanisms of action, namely those that rapidly degrade a target subject to nonlinear positive feedback, than for others. These observations provide a potential clinical guidance to the use of EPIs as antibiotic adjuvants; rather than using them in all cases, it is vital to understand the transient population dynamics induced by particular antibiotics to determine whether EPI usage would result in a positive outcome.

2.5 Conclusions

In this chapter, I have proposed and validated a minimal mechanism that can give rise to the postantibiotic effect (PAE) in response to a diverse array of antibiotics. I

show that PAE is a function of total antibiotic delivered to a population, and that antibiotic transport and binding kinetics are sufficient to explain this dependence. Significantly, I demonstrate that the efficacy of efflux pump inhibitors (EPI, an established class of antibiotic co-treatments, is dependent on the dynamics of the pathogen-antibiotic system; our results may explain apparent failures observed in EPI treatment.

3. Linear population allocation by bistable switches in response to transient stimulation

In this chapter I present a study of population allocation in response to transient stimuli. Inherent to these conclusions is the idea of intra-population stochasiticity; coupled with nonlinear feedback, it is possible that genotypically identical individuals assume different fates in response to identical input signals. I demonstrate this phenomenon for a variety of bistable motifs of increasing complexity, and propose the adaptive advantages of a linear response to stimulus strength.

3.1 Bistability

Bistable systems refer to those in which a species of interest (e.g. chemical species, protein numbers, etc.) assumes one of two stable states (e.g. concentrations). In response to a stimulatory signal, the system state can be shifted from one equilibrium to the other, but critically, when the signal is withdrawn, the current state of the system is maintained. Regardless of the specific details of implementation, all bistable systems share two defining features: nonlinear positive feedback, and hysteresis. The first implies that the species of interest directly or indirectly induces its own synthesis; nonlinear feedback creates ultrasensitivity to input signals and ensures that two states, e.g. OFF and ON, are stable (Figure 21**A**). Hysteresis refers to the idea that bistable systems are, to varying degrees, reversible. However, one transition, e.g. OFF to ON, is

often more difficult than the reverse, e.g. ON to OFF. This can be visualized in terms of potential energy (Figure 21**B**); stable steady states correspond to local minima separated by an unstable steady state (the critical value necessary to switch). Hysteresis is implied in the fact that these potential wells may be of different depths. In this case, the system state will depend not only on the stimulus strength, but also on the stimulus history; the transition between states occurs at different stimulus values if the stimulus is increasing vs decreasing (Figure 21**C**). Several mechanisms can give rise to bistability, including nonlinear positive feedback[198], protein titration[199,200], and ultrasensitivity[201,202].

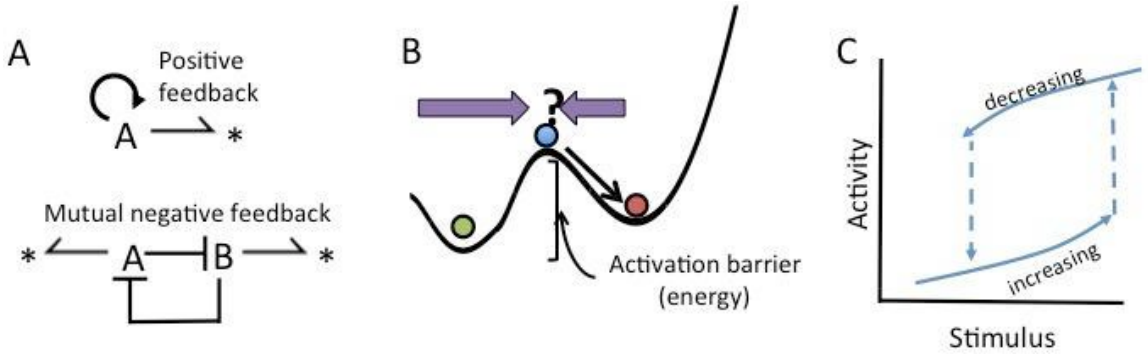

Figure 21: Bistability results in systems assuming one of two stable states. A. Bistability can arise through a number of mechanisms/motifs, including nonlinear positive feedback (top), wherein a species of interest catalyzes its own synthesis, or mutual negative feedback (bottom), wherein two species each inhibit the synthesis of the other. In each of these cases, a sufficiently strong external stimulus can shift the system from one state to another, e.g. from low A to high A (positive feedback), or high A/low B to low B/high A (mutual negative feedback). B. The transition between bistable states can be visualized in terms of potential energy; stable states correspond to local minima, separated by an unstable intermediate state. If the stable states are of unequal depth, the system will default to the more stable default. C. Hysteresis is a property of bistable systems that refers to the fact that different stimulus histories (e.g. increasing vs decreasing) will result in different response curves and state

transition points. Specifically, in the bistable region, the system state is dependent on the stimulus history.

In the context of biological systems, it is important to note that bistable networks function in concert with intra-population heterogeneity. That is, even in a clonal population of cells, the presence of both intrinsic and extrinsic noise[203] implies that species of interest, e.g. protein concentrations, follow a distribution (typically assumed to be normal) rather than be numerically identical. Therefore, in heterogeneous bistable populations, noisy dynamics dictate which individuals will transition from an initial state, in response to some stimulus.

3.2 Decision making in biological systems

To optimally survive, cell populations must appropriately respond to changes in environmental conditions, including nutrient availability, competition, and drug perturbations. These environmental cues often trigger distinct cell fate responses (e.g., rest vs. grow; live vs. die) in an otherwise homogeneous cell population. These distinct responses are important to both the fitness of unicellular microbes and the proper cellular functions in multicellular organisms, e.g., tissue homeostasis[204], differentiation[205], and wound healing[206-208].

Despite the diversity of cell fate response systems, many share a common property: the phenotypic response is controlled by a bistable switch that assumes one of two stable states (e.g. OFF and ON). Extensive modeling and experimental studies have investigated the generation and modulation of the bistable systems, with emphasis on their responses to sustained signals[198,209]. However, bistable switches can operate under conditions where input signals are transient. For example, *Bacillus subtilis* shifts from vegetative growth to competence and sporulation in a nutrient-limited environment [210]. It reverts to the vegetative state when sufficient nutrient is available. If too many individuals revert, the nutrient level may be insufficient to support them; if too few individuals revert, the population would fail to fully utilize the available resources. The fraction of reverted individuals is dependent on the nutrient duration, in a process controlled by a bistable switch involving the regulatory gene *SpoA*[211].

Bistable decisions also underlie the development and maintenance of virulence factors in a variety of bacterial pathogens, including the human pathogens *Salmonella typhimurium*[212,213] and *Pseudomonas auruginosa*[214], as well as the plant pathogen *Dickeya dadantii*[215]. A major driver of virulence in all these species is the expression of a Type III secretion system (T3SS) that allows the pathogen to inject host cells with protein factors that enable invasion [216]. Single-cell studies have shown that the T3SS is often expressed in a bistable manner in response to environmental factors such as salt concentrations[212].

That is, a clonal population contains a mix of two phenotypic subsets, T3SS+ and T3SS-. While the T3SS+ subset enables the *Salmonella* population to invade the host[217], it has a slower growth rate (probably due to an increased metabolic burden and the presence of gene regulons that couple metabolism and virulence)[218,219]. Therefore, a tradeoff is necessary between growth and virulence – if the T3SS+ fraction is too high, the population cannot multiply fast enough to withstand host defense mechanisms; if the T3SS+ fraction is too low, the population cannot invade the host cells effectively. To this end, the bistable system that controls the T3SS expression may coordinate the population distribution (T3SS+ vs. T3SS-) based on the favorability of environmental conditions.

Another example is bacterial programmed altruistic death (PAD). In response to stress, a fraction of a population undergoes programmed death, which leads to the release of certain "public good" molecules and ultimately the stress alleviation, thus benefiting the survivors[220,221]. For each cell, death is a bistable decision (a cell either dies or lives). I have previously shown that an optimal death rate exists for a given stress level. If the death rate is too low, the population will be unable to alleviate the stress; if the death rate is too high, the population will be unable to recover, even after the removal of stress[77]. When a PAD-capable population is subjected to transient stress, such

as periodic antibiotic dosing, the bistable network might inherently set the optimal death rate, based on the dosing profile.

Given that bistable decision-making motifs are so common in natural systems, what are the evolutionary advantages of population phenotypic heterogeneity, and thus, apportioning a population to multiple potential outcomes? In general, population heterogeneity arises due noise in protein concentrations, which can be due to stochastic gene expression[222], differential access to resources[223], or other factors. This heterogeneity is the basis for evolution: subpopulations that have a fitness advantage (i.e. faster reproduction) will eventually dominate a previously resident population. In the face of steady state environmental conditions, heterogeneity optimizes a population towards one phenotype. However, in the face of uncertain or rapidly changing environmental conditions, it becomes advantageous to maintain multiple phenotypes concurrently, each of which responds optimally to a given set of conditions. This strategy, called "bet hedging"[224], serves to spread the risk inherent in varying conditions, and has been observed in a variety of natural systems[225,226], and mechanisms including negative frequency dependence[227], temporal variation[228], kin selection[229], and state dependence[230]. However, the question of how to optimally divide a population amongst multiple states remains an open area of research.

3.3 Premise

The wide prevalence of bistability motifs in biological systems leads to the question: how does a bistable switch responds to transient signals. Without loss of generality, each transient signal can be approximated by a rectangular pulse (Figure 22A) with intensity S and duration D. If the switch operates in the absence of noise (in a hypothetical cell population), I expect a uniform, binary transition (e.g. from OFF to ON) at a critical stimulus duration, D_{crit}, which is a function of the switch parameters and the signal intensity S. However, in the presence of cellular noise, D_{crit} may vary from cell to cell (Figure 22**B**). The superimposing of stochasticity onto bistability leads to the division of a cell population into two subpopulations, e.g. OFF and ON. Intuitively, the magnitude of stochastic noise must be restricted within some intermediate range to ensure the emergence of a bimodal population: at extremely low noise levels, I would expect to see a deterministic transition with increasing stimulus. In contrast, excessively high noise would overwhelm the network dynamics.

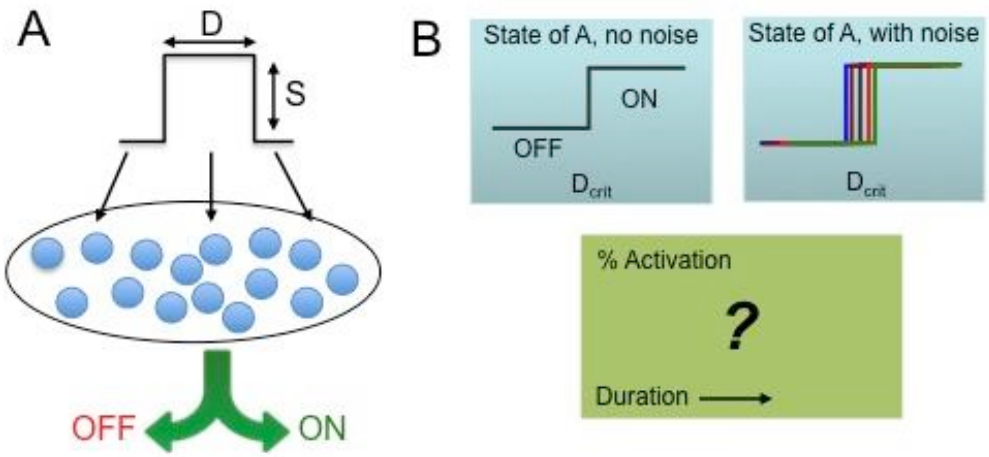

Figure 22: Stimulation of a bistable network by a pulse input. A. A pulse input can be specified by its intensity (S) and duration (D). Stimulation of a stochastic bistable network in an isogenic population using this pulse results in the emergence of two distinct subpopulations (e.g. OFF and ON). B. If the activation is deterministic, there exists a critical pulse duration beyond which all individuals in a population will transition between the two steady states (e.g. from OFF to ON) (top panel). Presence of noise will result in variability in the critical duration: different individuals will be activated at different thresholds (middle panel). For a short duration, a fraction of a population will be allocated to either steady state. Here, I aim to investigate this population activation, which I term "activation probability", as a function of both pulse intensity and duration (bottom panel).

Here I examine *how the fraction of activated individuals (the ON subpopulation) depends on the strength and duration of the transient input signals*. I use theoretical analysis and computational simulations to investigate the input-output function of three representative bistable systems with increasing complexity. In particular, I focused on the effects of varying input signal parameters and noise levels. I show that increasing the stimulus duration results in an exponential asymptotic increase in population activation. When the input duration is short, this dependence is *linear*, and this property is

maintained for all three bistable systems. I propose that this linear dependence (activated fraction vs. signal duration) can function as a survival strategy, representing an optimal response to transient input signals. I use a minimal model to demonstrate that when pulse (e.g. nutrient) duration governs growth rate, over-allocation results in slower growth due to cells having fewer resources; conversely, under-allocation results in wasted excess resources. A linear strategy balances these two detrimental effects, enabling populations to proliferate faster than either extreme. In this regard, a bistable switch acts as an integrator, enabling a cell population to assess transient signals based on intensity and duration and respond accordingly.

3.4 Results

3.4.1 A positive feedback circuit

We start with a minimal bistable system consisting of a protein driving its own synthesis, forming a positive feedback loop (Figure 23**A**). This system can be modeled using a single ordinary differential equation (ODE): $\dot{x} = f(S,D) + a(x) - x$. The three terms on the right hand side of the equation, from left to right, correspond to external stimulation, nonlinear positive feedback, and decay, respectively.

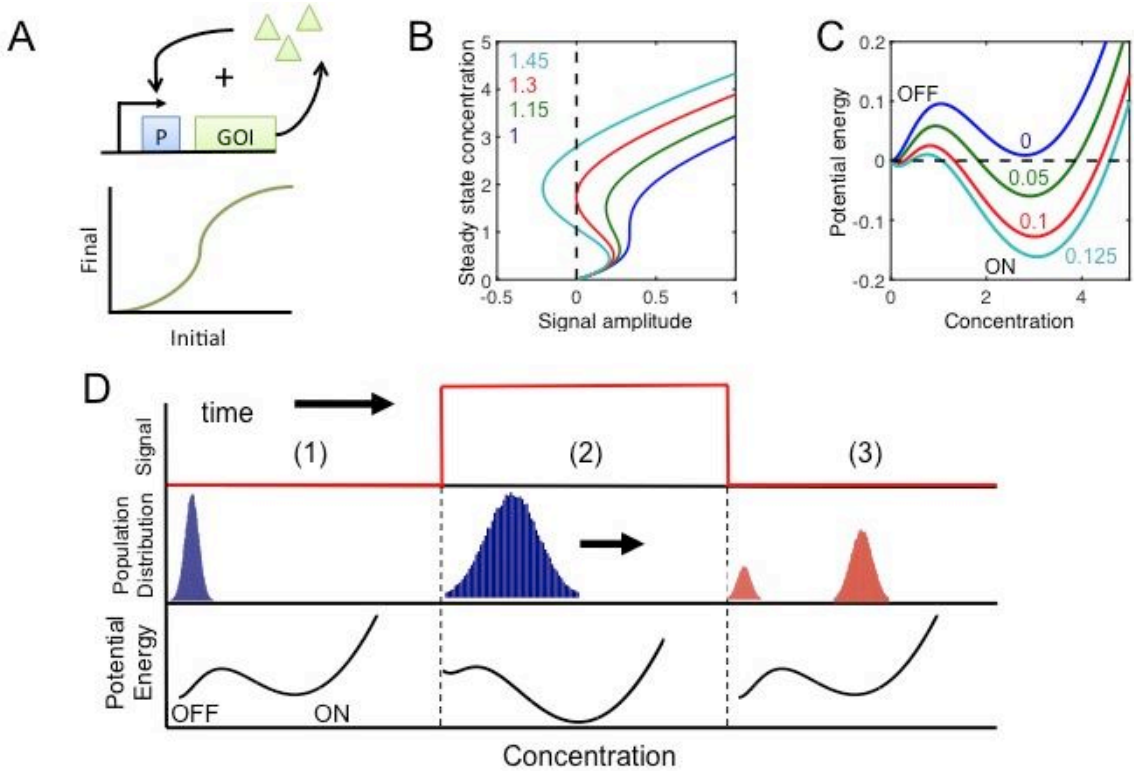

Figure 23: Response of a positive-feedback model to pulse inputs. A. A minimal positive feedback motif consists of some gene of interest (GOI) which drives its own synthesis by activating its promoter *P*. Nonlinear feedback is often achieved through cooperative binding, leading to a sensitive response dependent on the initial concentration of the GOI. B. The effect of autocatalysis. In the absence of stimulus (dotted line), the emergence and relative placement of steady states in the non-dimensional model can be tuned with the autocatalytic parameter "c". For low values of this parameter, the only steady state is at 0. However, with sufficiently strong positive feedback, two nonzero steady states emerge. C. Potential energy landscapes as a function of stimulus intensity. If the autocatalysis parameter "c" is chosen such that nonzero steady states are attainable, the potential energy landscape forms two wells corresponding to OFF and ON. Increasing stimulus intensity simultaneously leads to a shallower well at c_{off} and a deeper well at c_{on}. This trend corresponds to an overall shift in the population from OFF to ON with increasing stimulus. Here I used $c = 1.45$, $\epsilon = 0.005$, and $D_e = 0.01$. D. Schematic shows the evolution of a population of cells carrying a bistable switch (blue) in response to a pulse input (red). Potential energy landscapes are shown in black. In the absence of stimulus (1), the population is in the OFF state. When stimulus is applied (2), the potential energy landscape shifts in favor of the ON state, driving the population toward the ON state. When the

stimulus is removed (3), the potential energy landscape reverts to its initial state, splitting the population into two subpopulations (OFF and ON).

Without loss of generality, I choose $u(x) = \frac{8}{3} c \frac{x^2}{3 + x^2}$ and the parameter c such that the system is bistable in the absence of stimulus ($f = 0$), with an unstable steady state at $x_* = 1$ and $\dot{u}(x) = c$ (See model development for detailed description). A larger value of c corresponds to stronger positive feedback, which increases the distance between the two steady states (Figure 23**B**). We use the Fokker-Planck formulation of this non-dimensional ODE to incorporate the effects of both mechanism-dependent (intrinsic) and independent (extrinsic) noise sources, which we assume to be Gaussian distributed. This formulation enables us to simulate the noise inherent in biochemical reactions, due to the effects of both discrete small numbers of molecules as well as small reaction volumes (i.e. cells). Unless f is saturating, the potential landscape resulting from this stochastic ODE has two wells corresponding to two stable steady states (Figure 23C), separated by an energy barrier at the unstable steady state. For saturating f, the landscape is monostable.

For $f = 0$, consider a population of cells residing at the OFF state, assuming a Gaussian protein distribution (Figure 23D, panel 1). When the stimulus is applied ($f > 0$), the landscape shifts in favor of the ON state: the energy barrier is lowered and

the ON state becomes more stable. This shifted landscape promotes stochastic transition from the OFF to the ON state (Figure 23D, panel 2), as if the population of cells are gradually sliding toward the ON state. When the stimulus is turned off, the potential landscape reverts to the initial configuration (Figure 23D, panel 3). At this moment, the population will be split into two subpopulations, depending on the relative position of each cell in comparison to the unstable steady state. Cells to the right of the unstable steady state will continue to move toward the ON state; those to the left will move back to the OFF state. The fraction of activated cells (or the activation probability) depends on the transition rate, which in turn depends on stimulus intensity and noise magnitude.

Using the Fokker-Planck equation, we find that, for a given input intensity, the activation probability increases with the input duration, approximately following an exponential asymptotic function: $p_{act} = 1 - e^{-rD}$. The transition rate constant, *r*, is a function of the input strength (*f*) and noise magnitude (see Supplemental Information for full derivation). This theoretical solution agrees well with results from numerical simulations, using the corresponding stochastic differential equations (SDE) (Figure 24A). As expected, stronger stimuli result in a deeper ON well, and a faster increase in activation probability, characterized by larger *r* values (Figure 24B). Importantly, for sufficiently small D, $p_{act}(D) = 1 - (1 - rD) = rD$. That is, for a

population of cells exposed to a short stimulus, the number of cells that switch increases linearly with the signal duration.

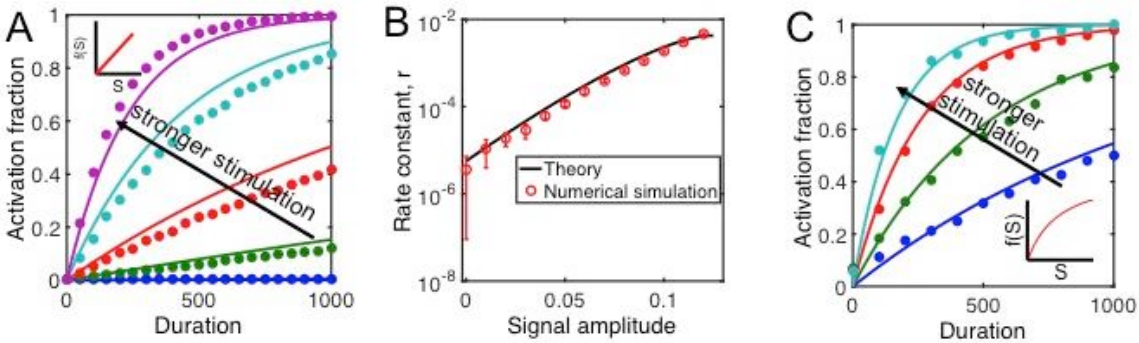

Figure 24: A. Simulation (open circles) vs. theoretical prediction (solid lines) of activation probability as a function of pulse duration. The black arrow indicates increasing stimulus intensity. The activation probability increases linearly with the duration, when the latter is small. Inset shows intermediate signal transformation function. B. The transition rate dictates the linear dependence, and increases with increasing stimulus intensity. Open circles and lines indicate theoretical and numerical predictions, respectively. C. The pulse strength can be monotonically scaled upstream of the bistable decision module without affecting the characteristic activation property. Here, I use a Hill function with coefficient $n = 2$ as the transformation function (shown in inset).

In general, a pulse input can be processed by an intermediate signaling module or cascade in the cell, prior to the bistable module. Mathematically, this processing can be considered as a transform by a relevant function (e.g. a Hill function). The resulting scaled stimulus will assume a modified shape dictated by the signaling module throughout the stimulus duration, while remaining zero for $t > D$. As long as the transformation is monotonic in terms of signal strength, it does not qualitatively change the allocation property (Figure 24C, inset shows intermediate transformation): the

activation probability increases approximately linearly with increasing duration of the input pulse, when the duration is small.

Our analysis confirms previous studies of switching properties, which have described exponentially distributed residence times in potential wells using Fokker-Planck formulations of population drift and diffusion [231-234]. However, these studies utilize arbitrary two-well potential functions to realize transitions from one state to another. It is unclear to what extent these conclusions are applicable to more complex bistable systems, based on molecular mechanisms, which exist in nature. Furthermore, these studies do not address the potential biological implications of these switching properties. To that end, I use numerical simulations to interrogate the response of two increasingly complex bistable frameworks, and describe a general biological scenario in which conserved switching properties may be advantageous to bistable populations.

3.4.1.1 Model development

Given a positive-feedback system dictated by:

$$\dot{x} = f(t) + a(x) - x \qquad (13)$$

where $f(t)$ represents an external source signal that can be experimentally controlled and can potentially serve as a trigger for the switch, $u(x)$ represents a necessarily nonlinear, autocatalytic Hill term leading to bistability, and $-x$ denotes

degradation of the species of interest. Here, the dimensionless time constant of the decay term is unity, indicating that the physical unit of time is the inverse of the decay time constant.

A number of general constraints on this non-dimensionalized system are necessary to better to mimic actual stochastic biological systems:

In the absence of external stimulus $f(t)$, extrinsic noise should induce a basal fraction of individuals to the ON state.

The rate of transition from ON to OFF (the 'reverse' direction), while non-zero, will follow a time constant much longer than the OFF to ON transition; therefore, there will be negligible 'deactivation' within the time scale of interest.

Without loss of generality, take the autocatalytic term $u(x)$ from Eq. S1 above as:

$$u(x) = \frac{8}{3} c \frac{x^2}{3 + x^2} \qquad (14)$$

Using this Michaelis-Menten form with appropriate parameter choices ensures bistability. Here, I have chosen the pre-factor and half-maximal values such that $u(x)$ has its inflection point corresponding to the maximum of $\frac{da}{dx}$ at $x = 1$. Bistability in the kinetics dictated by Equation 14 are shown in the following bifurcation diagram (Figure 23B). Here, I have set $\dot{x} = 0$ to show the steady states of x as a function of constant stimulus f. Each trajectory in Figure 23B represents this relationship for a particular

value of the constant c. A particular steady state value of x is linearly stable if $\frac{d(x-a(x))}{dx} > 0$; accordingly, the portions of the trajectories with positive slopes represent stable branches. Conversely, the portions with negative slope are unstable branches. If $c < 1$, the graph of x vs f is monotonically increasing; there is a unique stable point. For $c = 1$, a vertical tangent occurs at $(x, f) = (1, \frac{1}{3})$. For each $c > 1$ condition, then, I have a bistable range of f, separated by stable branches where the system is either OFF (lower branch) or ON (upper branch); the points at which the bistable range meets either the stable or unstable branch are saddle-node bifurcations. I note that the ON saddle-node bifurcation crosses the f axis for $c = \frac{3\sqrt{3}}{4} \approx 1.299$. This means that for $c = \frac{3\sqrt{3}}{4}$, there will be no ON state in the absence of stimulus ($f = 0$); conversely, for $c > \frac{3\sqrt{3}}{4}$, there exists an ON state with $f = 0$.

These trajectories correspond to situations in which a subpopulation will be activated even in absence of stimulus, satisfying condition (i) from above. I have chosen $c = 1.45$, which corresponds to a metastable ON state; although a subpopulation may be activated in the absence of stimulus (due to stochastic noise), all individuals will settle at the OFF state given an infinitely long time span. In this work, we are interested in the

population response to a transient square wave signal $f(t)$; that is, $f(t- < D) = k > 0, f(t > D) = 0$ for some arbitrary signal duration D.

3.4.1.2 Deriving and analytical solution for activation probability

In practice, the deterministic kinetics given by the ODE in Equation 14 are perturbed by random noise. Here, we consider two sources of such noise: a chemical noise (intrinsic to $x(t)$ itself), and an extrinsic component due to the inherent randomness of the system environment. Because $x(t)$ is a protein concentration, and changes therein are discrete events, I model the noisy dynamics using Poisson processes; therefore, at any time, a population will form a distribution with positive variance.

We can use a Fokker-Planck formulation to examine the behavior of this system in the presence of stochastic noise. The dependent state variable is the ensemble probability density $p(x)$. Specifically, in a given population, the fraction of individuals with concentrations $x(t)$ in the range $(x, x+dx)$ is $p(x,t)dx$. The dimensionless Fokker-Planck equation (FPE) for the system can be simply written as a convection-diffusion partial differential equation (PDE) in x-space as follows, where j denotes the flux term, and subscripts indicate first partial derivatives:

$$p_t + j_x = 0 \qquad (15)$$

$$j = (a(x) - kx + f)p - \{(D_E + \frac{1}{2V}(a(x) + kx + f))p\}_x \tag{16}$$

Here, the first term in j represents the convection of probability in accordance with the deterministic kinetics. The second term represents diffusion of probability due to the two aforementioned sources of random noise. Specifically, D_E represents external noise; the remaining terms represent the probability flux associated with chemical noise. Nondimensionalization yields the following form, where ϵ scales the intrinsic, state-dependent noise component:

$$j = (a(x) - x + f)p - ((D_e + \epsilon(a(x) + x + f))p)_x \tag{17}$$

In chemistry, "detailed balance" refers to equilibria in which forward and backward reaction rates are exactly balance, and there is no net changes in species concentrations. In an FPE, the analogous situation occurs when the probability flux vanishes identically. If the state space of independent variables (here $x(t)$) is one-dimensional, I can always find equilibria characterized by detailed balance. If I set $j = 0$, the solutions $p(x)$ are proportional to the following Boltzmann factor:

$$p(x) \propto e^{\frac{-U(x)}{D_E}} \tag{18}$$

Where $U(x)$ is the effective potential in the concentration space. This satisfies the following relationship:

$$\dot{U}(x) = \frac{x - a(x) - f - \epsilon(a(x) - a)}{1 + \frac{\epsilon}{D_E}(a(x) + x - f)} \tag{19}$$

The Boltzmann factor, as a function of x, has maxima at the minima of $U(x)$. In the case of zero intrinsic noise ($\epsilon = 0$) Equation 19 reduces to the conditions for a stable critical point in the deterministic system.

As shown in Figure 23C, the potential landscape, $U(x)$ vs x, consists of two wells separated by a barrier, reflecting the stable points of the system and the perturbation required to transition between them. The range of stimulus f shown is within the aforementioned bistable range. For each landscape, the wells are given by the minima of $U(x)$: I will denote these minima as $U_{off} = U(f, x_{off})$ and $U_{on} = U(f, x_{on})$, where $U_{on} > U_{off}$. These minima are separated by an energy barrier; I will define $E = U(x_c) - U_{off}$. This is the energy required to transition from the OFF state to the ON state. With no stimulus, the OFF state is favored; as stimulus increases, the ON state becomes increasingly favored.

We are interested in transient stimuli; in these situations, a population will encounter two landscapes. Initially, with the application of stimulus, the nonzero stimulus will yield a landscape more permissive towards activation, allowing a fraction of individuals to overcome a relatively low E. When stimulus is removed, the landscape reverts, and activation becomes significantly less likely (refer to Figure 23D). I are interested in the fraction $p_{act}(t)$, which I define to be the proportion of a population that is activated during a transient stimulus of length t. That is, the fraction that surpasses x_c within the interval $t < D$ with nonzero stimulus. The rate of transition from OFF to ON is ultimately dependent on f. The predicted rate constant based on asymptotic analysis of the Fokker-Planck equation in the small noise limit $\frac{E}{D_e}$ is as follows:

$$r := \frac{1}{2\pi}\sqrt{\ddot{U}_{off}\,|\ddot{U}_c|}\,e^{\frac{E}{D_e}} \qquad (20)$$

In general, then, $p_{act}(t)$ satisfies the following ODE:

$$\dot{p}_{act}(t) = r(1 - p_{act}) \qquad (21)$$

It is easily seen that the ODE satisfied by:

$$p_{act}(t) = 1 - e^{-rt} \qquad (22)$$

We note that for weak stimuli, which correspond to small values of r, the activation probability increases linearly for sufficiently short stimulus durations $\frac{dp_{act}}{dt} \approx r$.

3.4.2 A toggle switch model

To test the general applicability of the linear response, I next examine the response of a toggle switch[235] to transient stimulation. This motif has been found in numerous natural biological networks[236,237], and is one of the first regulatory motifs to be implemented and analyzed with synthetic gene circuits using different genetic elements, in bacteria, yeast, and mammalian cells[238-241]. The toggle switch consists of two molecular species mutually inhibiting each other (Figure 25A). Due to its greater complexity, I employ dimensionless numerical simulations using an SDE model (all units are arbitrary) to examine its response to a pulse input.

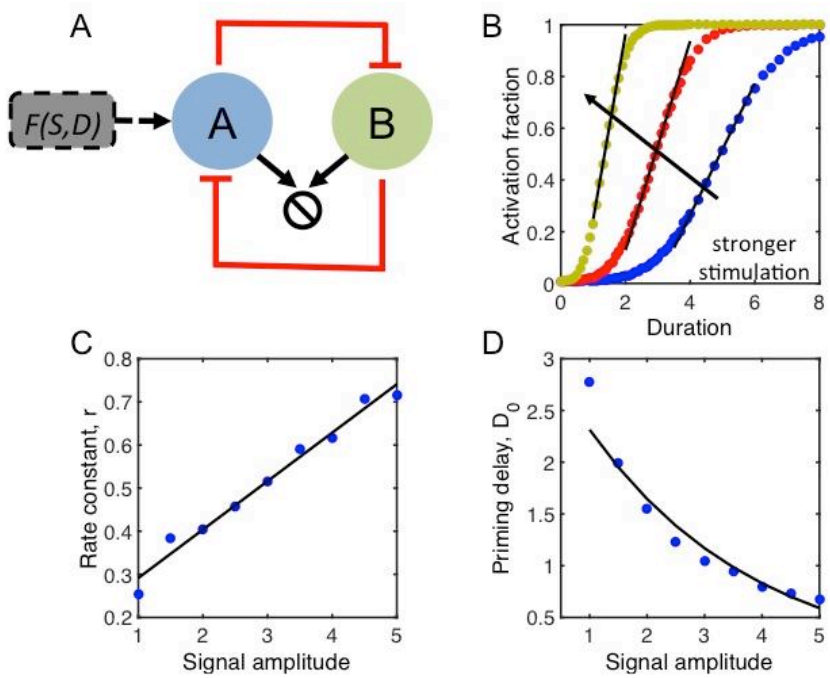

Figure 25: Response of a toggle-switch to pulse inputs. A. A toggle switch consisting of two molecules (A and B) inhibiting each other. With sufficient nonlinearity, the system is bistable, with either A or B dominating. Our analysis assumes that all cells are initiated at state A. A pulse input is applied to drive them into state B. B. Simulated dependence of the activation probability on pulse duration. For sub-saturating durations, the dependence exhibits an approximately threshold-linear property: there is no activation until the pulse duration is above a threshold; then the activation probability increases linearly (as shown by solid lines, R2>0.9) until saturation. Black arrow indicates direction of increasing stimulus intensity. C. The linear activation regime slope r increases with stimulus intensity (linear fit, R2=0.987). D. The priming delay D_0 decreases with stimulus intensity (exponential decay R2=0.972).

Our simulation results show that the toggle switch exhibits a "priming" period (D_0): for signal durations less than this value, the switch is minimally activated. This feature is likely due to the inhibitory mechanism. For example, assuming a population is initially in state A, weak upregulation of B (short duration) will be unable to overcome

the inhibition of B imposed by high levels of A. For stimuli longer than D_0, the system follows the same short duration linear approximation as the cooperative model. I can fit the activation probability curve using $p_{act}(D) = r(D - D_0)$, taking $p_{act}(D) = 0$ for $D < D_0$. A representative example is shown in Figure 25B (solid line, see Materials and Methods for details). In addition, our results show that the rate of linear increase, r, is positively correlated with the signal intensity (Figure 25C, solid line shows linear fit, $R^2 = 0.987$) and that D_0 should decrease with increasing stimulus intensity, as shown in Figure 25D (solid line shows exponential decay, $R^2 = 0.972$). Here, it is important to note that a priming period may occur for any bistable motif, given sufficiently short pulse duration. That is, if the pulse duration were short enough that activation is outweighed by degradation, the system would experience a priming delay. In the preceding positive feedback model, the lack of inhibition means that the priming delay is negligibly short compared to the subsequent linear activation region.

3.4.2.1 Model development

We use a variant of the toggle switch model originally derived by Gardner et al.[235]. In this model, nonlinear mutual inhibition between two species creates a bistable landscape. The deterministic ODEs and rate parameters used are as follows:

$$\frac{d[A]}{dt} = k_0 + f([S]) + \frac{k_A}{K_1 + [B]^n} - d_A[A] \tag{23}$$

$$\frac{d[B]}{dt} = \frac{k_B}{K_2 + [A]^n} - d_B[B] \qquad (24)$$

Table 3: Parameter values for a mutual inhibition toggle switch

Parameter	Description	Value
k_0	Basal level production	1e-5 [μM/h]
k_a	Synthesis rate of A	0.7 [μM/h]
K_1	Half maximal level of A	1.66e-4 [μM]
k_b	Synthesis rate of B	1 [μM/h]
K_2	Half maximal level of B	1.66e-4 [μM]
d_A	Degradation rate of A	0.2 [1/h]
d_B	Degradation rate of B	0.95 [1/h]
σ	Intrinsic noise scale factor	1
γ	Extrinsic noise scale factor	1

3.4.3 A bistable Myc-Rb-E2F model

We next examine a much more complex network, Myc-Rb-E2F network (Figure 26A), which plays a critical role in controlling cell cycle entry and cell fate decisions [242,243]. Dysregulation of this network has been shown to contribute to uncontrolled cell proliferation and cancer development. Our previous work [244-246] has studied the dynamic network properties underlying E2F-mediated cell cycle entry. In normal cells, serum stimulation can lead to bistable activation of E2F, which in turn serves as a master-regulator of genes involved in cell cycle entry.

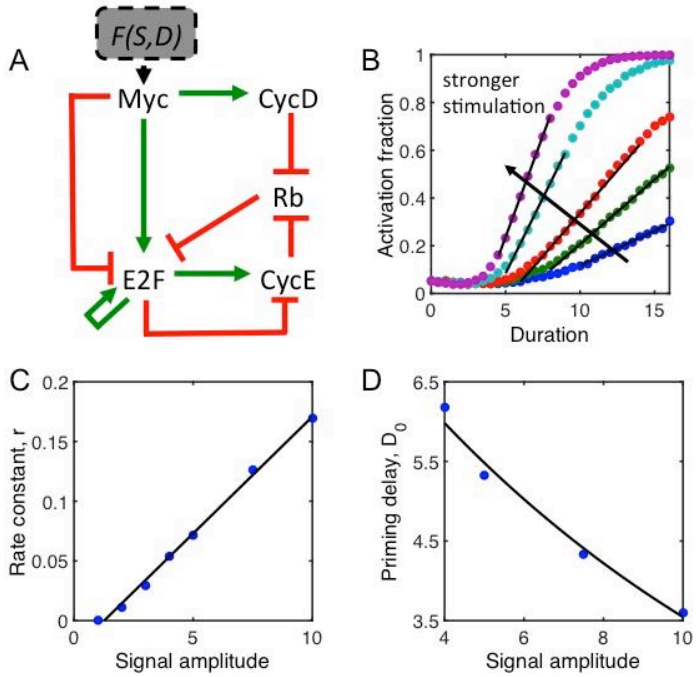

Figure 26: Response of the Myc-Rb-E2F network to pulse inputs. A. In response to serum stimulation, the Myc-Rb-E2F can exhibit bistability in E2F levels. B. Simulated dependence of activation probability on the duration of the pulse input. Solid black arrow indicates increasing stimulus intensity. The dependence is approximately threshold linear for sub-saturating durations. Black arrow indicates direction of increasing stimulus intensity. C. The linear activation regime slope r increases with stimulus intensity (linear fit, R^2=0.997). D. The priming delay D_0 decreases with stimulus intensity (exponential decay R^2=0.985).

Again, I adopt an SDE model [247] of the Myc-Rb-E2F network to examine its response to transient growth stimulation (Figure 26B and Figure 27). Despite its much greater complexity, this model exhibits qualitatively the same trend in activation probability (Figure 26B) as the toggle switch model. In particular, a population exhibits a threshold-linear response: when the stimulation duration is shorter than a threshold value (D_0, the priming duration), the network does not respond significantly. In this

case, the priming delay is due to a number of inhibitory interactions, as diagrammed in Figure 26A. For a short duration above D_0, the activation probability increases linearly with increasing duration. As shown in Figure 26C, the rates of linear increase are dependent on the stimulus intensity (line shows linear fit, $R^2 = 0.997$). As with the toggle switch, the priming delay D_0 decreases exponentially with increasing stimulus intensity (Figure 26D, $R^2 = 0.985$).

3.4.3.1 Model development

The Myc-Rb-E2F pathway has been extensively studied in connection with mammalian cell cycle control and cell fate decisions[248,249]. When exposed to appropriate growth factors (serum, Myc, etc), E2F family proteins are upregulated, exhibiting a peak and decline behavior characteristic of adaptive response. This transient increase in E2F levels in turn regulates hundreds of downstream genes that lead to DNA replication and eventual cell division. As such, dysregulation of this network has been implicated in many cancer types, and constitutes an active area of study [250-252]. Here, I use the Myc-Rb-E2F pathway (Figure 26A) as a case study; I take the model equations and rate parameters from the literature [245,247], and apply the simulation method described above. As shown in Figure 27A, in response to transient serum stimulation, a subpopulation of individuals will exhibit upregulation of E2F. Furthermore, this subpopulation will become more prevalent as the pulse lengthens, as can be seen in the progressive panels. I

detect the accompanying adaptive response numerically and use the width at the half-maximal E2F level as the distinguishing metric between inactivated (small width) and activated (large width) individuals (Figure 27B); this metric yields a bimodal distribution (Figure 27C) which I use to separate the activated fraction.

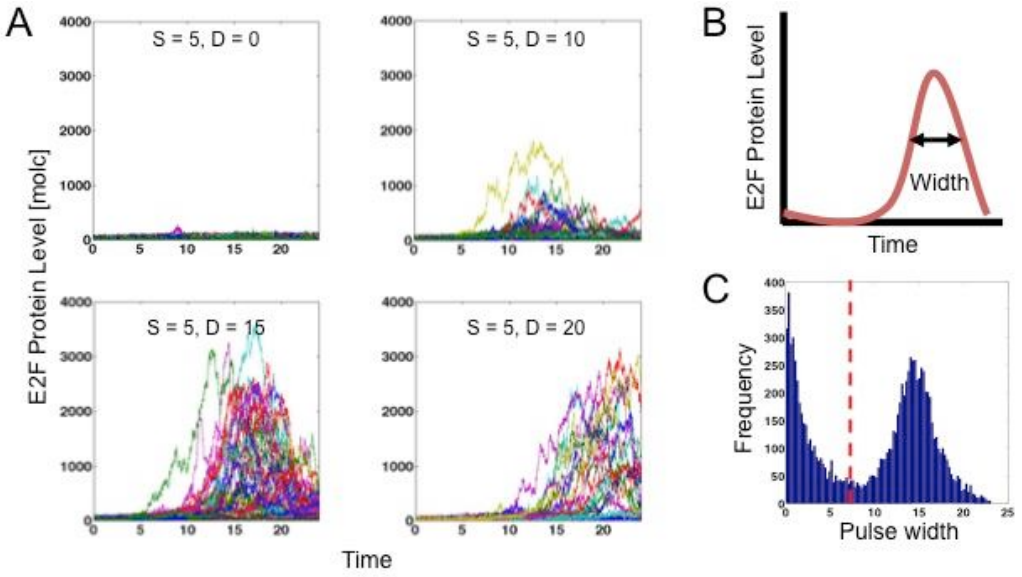

Figure 27: Determining activation for the Myc-Rb-E2F pathway. A. Simulated E2F time courses in response to a pulse input with varying durations. For sufficiently strong stimuli (e.g. S=5), increasing duration led to a characteristic adaptive response in E2F level (ON). The fraction of individuals exhibiting this adaptive response is a function of stimulus duration. B. and C. OFF and ON populations were delineated by the width of the pulsatile response. For each time course, width of the pulsatile response at the half maximum E2F level was determined. This metric resulted in a bistable distribution: the population centered at the higher mode was taken as the activated fraction.

3.4.5 Initial lag in the toggle-switch and Myc-Rb-E2F models

As shown in Figure 25B and Figure 26B in the main text, simulation results for both the toggle switch and Myc-Rb-E2F network show an initial lag phase, wherein for low stimulus durations, the activation probability does not increase appreciably. Subsequently, for sufficiently long durations, the activation probability appears to behave according to the previously described exponential relationship. This is not unexpected; intuitively, weak stimuli may fail to trigger transitions between steady states.

We propose that this effect is more noticeable for the toggle switch and Myc-Rb-E2F networks due to the presence of negative feedback regulation: the toggle switch modeled here is based on NF interactions as discussed in the main text. In the mammalian cell cycle model, titration of E2F by the protein Rb imposes a significant inhibition of E2F levels. In these cases, negative feedback sets a barrier to activation that must be overcome, hence the initial lag. In contrast, the cooperative model contains no such NF interactions. There will still be an initial lag in the cooperative system (due to degradation at low concentration), but evidently it is on a much smaller timescale than the minimum stimulus durations sufficient for activation.

3.4.6 Advantages of linear activation

Previous studies have demonstrated that negative feedback reduces the effect of biochemical noise and linearizes dose responses [253]. The negative-feedback-mediated linearization of dose responses occurs at the individual cell level. Our preceding analysis suggests that population response can also be linearized the in the duration domain: bistable switches amplify expression variability in individual cells and linearize the population-level response to transient stimuli.

How is the linear response advantageous to a cell population, compared to nonlinear responses, to a cell population sensing transient stimuli? For monotonically increasing response functions $p(D)$ over a given range of signal durations, a linear response is equally sensitive to variability in the signal duration regardless of the value of D. That is, because the derivative $\frac{dp}{dt}$ is constant, any fluctuation ΔD will result in the same change $\Delta p = p(D+\Delta D) - p(D)$, regardless of the value of D. In this manner, the bistable decision serves to integrate a transient input signal, respond cumulatively to fluctuating environmental conditions, and neither "over-commit to" nor "withhold from" a signal-dependent alternate steady state.

To illustrate this point, I constructed a minimal model in which an isogenic population responds to a train of multiple pulsatile stimulatory signals (Figure 28**A**); this

approach has previously been used to evaluated bistable populations [254-257]. These signals can be interpreted as a necessary resource (e.g. nutrients) for cells to grow and divide. That is, the duration of a pulse is proportional to the amount of resource made available to the population. The durations of these pulses are normally distributed around a mean value *D*, with ΔD_i being the deviation for the ith pulse. In each pulse, a fraction of the total population N_i is stimulated to proliferate, and the rest are eliminated (i.e. cell death). This bifurcation represents a bistable event: each individual either survives or does not. As such, the surviving fraction, or the activation probability, is a function of the signal duration ($k(D+\Delta D_i)$). Furthermore, I *assume that the growth rate of surviving cells depends on the amount of resource per individual* $\frac{g(D+\Delta D_i)}{N_i}$, following a Monod equation [258,259]. I simplified this model by assuming that resources are divided equally among all members of the population, and that the input signal intensity is strong enough such that variability in its intensity is negligible. Here, it is important to note that our model assumes that resources, once allocated, are consumed and thus unavailable to other cells in the population, e.g. when a stimulus pulse corresponds to nutrient availability. However, this may not be true for all stimuli. For example, transcription factors and enzymes can freely diffuse between, and affect, multiple cells without being consumed or degraded.

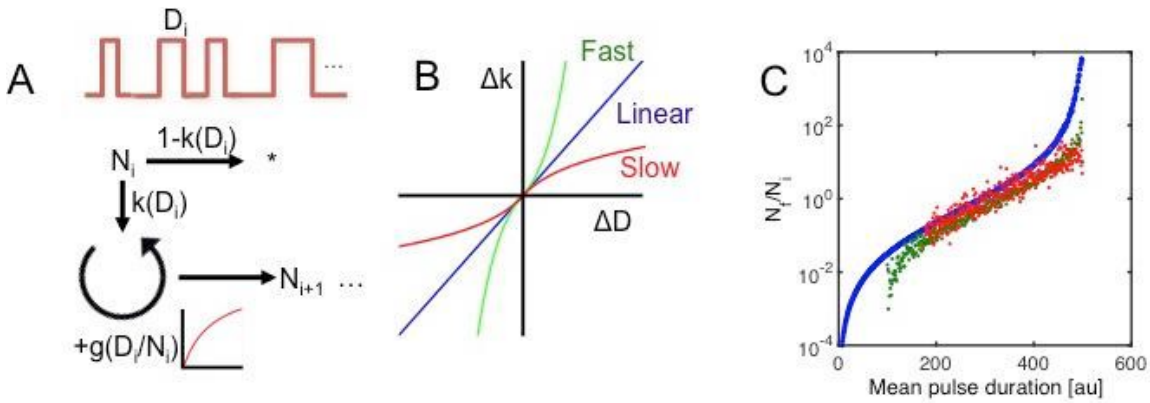

Figure 28: Linear increase in activation probability is a preferable allocation strategy. A. A discrete bistable system allows comparison of various activation probability curves. In this model, successive pulses of unit intensity, mean duration D, and Gaussian-distributed deviation ΔD_i are applied to a population. For each pulse, a fraction $p(D+\Delta D_i)$ are "activated" and proliferate. The rate of proliferation is assumed to be dependent on the signal intensity per individual $\frac{D+\Delta D_i}{N_i}$, following a Monod function. The remaining inactivated subpopulation is eliminated (i.e. cell death). I note that the conclusions about relative fitness are not affected if the inactivated subpopulation is assumed to be quiescent (alive but non-growing). Successive pulses can be applied to simulate fluctuating environmental conditions. B. Three characteristic activation probability curves as a function of signal duration. Population response can be grouped into one of three categories. A fluctuation in signal duration can result in a corresponding linear change in activation (blue line), or a change that is more sensitive (red line) or less sensitive (green line) than linear. Note that all three representative curves are defined over the same range of signal durations, and $k(0)=0, k(500)=1$ for all. C. For each characteristic curve in (B), I plot the fold change after 1,000 pulses of a particular mean duration. A linear allocation strategy results in a larger fold change than fast and slow activation for 100% and 86% of signal durations, respectively. I note that this qualitative conclusion is true regardless of initial population size and number of pulses.

In this scenario, how should populations respond to fluctuations in signal duration? That is, given a train of pulses with variable duration, what is the ideal

strategy to maximize the population fitness? To examine this question, I compared three representative response strategies:

Linear activation (Figure 28**B, blue line**): a fluctuation in signal duration ΔD results in a linear change in the surviving fraction.

Fast activation (Figure 28**B, green line**): a fluctuation in signal duration ΔD results in a stronger than linear change in the surviving fraction; a positive ΔD results in a greater increase, and a negative ΔD results in a greater decrease, in the surviving fraction when compared to linear activation. This strategy represents a "greedy" response, in that the over-allocation restricts the amount of resource available to each individual.

Slow activation (Figure 28**B, red line**): the opposite of fast activation; a fluctuation in signal duration ΔD results in a weaker than linear change in the surviving fraction; a positive ΔD results in a lesser increase, and a negative ΔD results in a lesser decrease, in the surviving fraction when compared to linear activation. This strategy represents a "cautious" response, in that under-allocation does not take full advantages of the resources available.

Here, I note that the curves shown in Figure 28**B** show *changes in activation probability*; the growth rate is fixed by the Monod equation, and the deviations can be linear, fast, or slow, as described above. I then simulated the effect of these different strategies on independent populations (please see Materials and Methods for detailed description). For each possible input signal duration, a train of variable pulses was used to stimulate the growth and/or decay of a population. I define fitness as the fold change between the final and initial population sizes. As shown in Figure 28**C**, a linear activation strategy outperformed (larger fold difference) both slow and fast activation for the majority of durations tested (100% and 86% of durations, as compared to slow and fast activation, respectively). These results suggest that the transition rate between bistable states can be optimized, especially in scenarios in which transition dynamics can affect overall fitness in opposing ways. I note that these conclusions also hold true if the inactivated subpopulation is assumed to be quiescent (alive but non-growing).

In the model examined here, fast activation appears beneficial in that more individuals survive the bistable decision; however, it results in lower per capita resource availability, and therefore a lower growth rate (overestimating the resource availability). Conversely, slow activation results in a higher growth rate due to higher per capita resource availability, but fewer individuals survive to take advantage of those favorable conditions (underestimating the resource availability). Clearly, there is a need to balance

these interconnected effects. Linear activation is a happy medium that allows populations to utilize fluctuating conditions moderately, without being greedy or overly cautious.

3.4.7. Discussion

Bistable decisions have been shown to underlie many cellular decisions, including differentiation and stress response. Previous studies have shown that pulsatile stimulation can be modulated to affect downstream gene expression in calcium-mediated signaling in yeast [260], NF-κB signaling in mammalian cells [261], and T cell stimulation [262]. These studies demonstrated that cell populations can multiplex different modes of information (signal intensity, duration, frequency etc.) to implement complex behaviors [263]. In many cases, these decisions are made on a single cell level; inherent biochemical stochasticity implies that the responses will vary within a population. In this context, it becomes important to understand how populations respond to non-saturating stimuli in the presence of cellular noise. Here I have demonstrated a characteristic linear dependence of activation probability on input signal duration in various stochastic bistable systems. Using a simple nonlinear feedback model, I showed that this activation probability can be mathematically predicted; I then demonstrated the same property in two increasingly complex systems, the toggle switch, and the Myc-Rb-E2F cell cycle network.

I propose that this deterministic duration-response linearity is an inherent feature of bistable systems, allowing populations to optimally respond to transient signals in a "real-time" manner, without *a priori* knowledge of signal duration. By allocating an appropriate number of individuals to each state, bistable networks could serve to ensure that populations take full advantage of favorable stimuli (e.g. increased nutrient levels), or avoid non-favorable factors (e.g. antibiotics). Notably, while positive feedback is generally thought to amplify variability, I show that bistable systems can process this individual uncertainty (at the single cell level) into a collective certainty (at the population level). Moreover, our results suggest that linear activation can be a better option than both excessively fast and prohibitively slow responses as a population survival strategy under fluctuating environment. Indeed, this linear response can be observed in a variety of scenarios. Recent work has demonstrated the emergence of linear response in T cell activation, wherein naïve T cells differentiate into helper T cells in response to antigen exposure [264]. As the antigen exposure duration is lengthened, the percentage of T cells transition to helper T cells increases linearly and then asymptotically approaches a maximum [262]. This differentiation decision is critical to generating a defensive immune response while minimizing the risk of autoimmunity [265]. Linear activation has also been observed in caspase-mediated apoptosis models, in which the fraction of dead cells increases linearly with the duration of treatment with an

apoptosis inducer such as Apo2L/TRAIL after an initial priming delay [266]. These conclusions are analogous to the response I have described; further demonstrating that linear response can be generated by a diversity of bistable motifs.

3.4.8 Materials and methods

3.4.8.1 Noise implementation and stochastic simulation algorithm (SSA)

We use a Langevin approach [267] to study the effects of intrinsic and extrinsic noise in all simulations discussed. Specifically, I use the form shown below:

$$\frac{dX_i}{dt} = \Sigma_{j=1}^{M} v_{ji} a_j [X(t)] + \sigma \Sigma_{j=1}^{M} v_{ji} a_j^{1/2} X(t) \Gamma + \delta\omega \tag{25}$$

where $X_i(t)$ represents the population of species i at time t, and $X(t)$ is the complete system state at time t. Therefore, the system temporally evolves according to the rates $v_{ji}X(t)$ with the inherent changes in molecular number given in v_{ji}, Γ and ω are temporally uncorrelated, statistically independent normal Gaussian noises. In this formulation, the first term on the RHS represents deterministic kinetics, the second term represents reaction-dependent (intrinsic) noise, and the third term represents reaction-independent (extrinsic) noise. The factors σ and δ are scaling factors that can be precisely adjusted to tune the levels of intrinsic and extrinsic noise, respectively. All reaction rate parameters and species concentrations were converted to molecular numbers as appropriate.

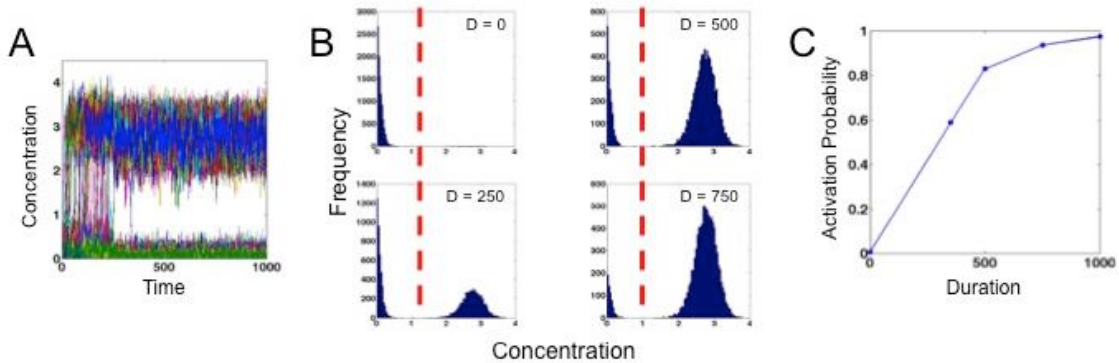

Figure 29: Determination of p_{act} from stochastic simulations of the positive-feedback model. A. Due to the presence of stochastic noise, replicates with identical initial conditions form distributions centered around two steady states. B. Time courses of 10,000 simulations were separated into OFF and ON fractions based on the boundary given by the critical unstable concentration value (middle panel, dotted line). C. The ON fraction was then plotted as a function of stimulus duration (right panel). I used the same method to evaluate the positive-feedback model and the toggle switch model.

As previously discussed, biochemical noise can stochastically induce a fraction of a population to transition from one stable equilibrium to another (Figure 29A), resulting in a population distribution (Figure 29B), dependent on the strength of the stimulus. Activation fraction can then be calculated as a function of stimulus intensity and duration (Figure 29 C).

3.4.8.2 Linear advantage simulations

A sequence of pulse durations was randomly generated, normally distributed with a given mean duration and variance equal to 10% of the mean. All populations were of the same initial size. For each pulse in the sequence, a fraction of the population

(dictated by the particular allocation strategy used) multiplied. The remainder of the population was discarded. The growth rate was assumed to be a Monod function of the per capita resource level, that is, pulse duration normalized by current population size. This procedure was carried out with 1000 consecutive pulses, after which the fitness was calculated as the fold change between the final and initial population sizes. All simulations were implemented in Matlab.

3.5 Conclusions

Bistable motifs often function as decision-making modules in living systems; in the face of biochemically noisy populations, a transient stimulus can apportion a subpopulation to each separate steady state. Here, I show that this outcome distribution is a linear function of stimulus intensity, and argue that such a property could be optimized, e.g. when faced with limited resources. This linear response may represent a form of bet-hedging, enabling a population to adjust it's average phenotype to respond to unpredictable conditions, e.g. nutrient deprivation, antibiotic stress, etc.

3.6 Acknowledgements

This chapter includes material from reproduced with permission from Lee TJ*, Srimani JK* et al, "Linear Population Allocation by Bistable Switches in Response to Transient Stimulation" *PloS One* **9(8)** (2014).

4. Postantibiotic effect: implications for treatment design

4.1 Introduction

In previous chapters, I examined the relationship between a single dose of antibiotic (or other stressor) and the resultant inhibition on population recovery and regrowth. However, typically, antibiotics are prescribed and administered periodically[54]. There are a variety of justifications for these strategies, including avoiding toxicity[268,269], maximizing bioavailability, and lengthening the total amount of time spent above the inhibitory threshold of a drug[270]. However, the particular timing of antibiotic dosing: what concentration to use, how many doses to administer, and at what interval, have often been determined by historical, *ad hoc* means, without a deep understanding of the resultant pathogen dynamics[271]. For example, a common refrain in classical antibiotic dosing is to "hit early, and hit hard"[272], meaning that antibiotics should be delivered at an early stage of an infection and at a high concentration, so as to kill as large a fraction of the population as possible and allow the natural immune response to inhibit the infection. However, studies have shown that such treatment strategies can often select for resistant subpopulations[273] and enable them to repopulate an infection post-treatment[274,275].

With the rise of antibiotic resistance, there has been a push towards antibiotic stewardship[15,180,197]. These efforts have espoused the more intelligent and efficient use of

antibiotics, so as to minimize their total usage and lengthen their shelf-life without inducing resistance. Although there have been efforts to develop novel antibiotics, this direction is not financially attractive, and has met with little success[12,276]. As such, it is of vital importance to develop a better understanding of antibiotic-bacterial dynamics and use that knowledge to administer existing antibiotics more effectively. To that end, recent studies have placed an emphasis on understanding the pharmacokinetics and pharmacodynamics (PK/PD) inherent in antibiotic treatment[277] to rationally design more effective dosing protocols. Various measures, including total area under the curve (AUC) of doses and time above minimum inhibitory concentration (MIC), have proven useful in dosing both concentration dependent antibiotics (e.g. aminoglycosides) and time dependent antibiotics (e.g. β-lactams)[278,279]. However, designing optimal antibiotic dosing protocols remains an open question[280,281]; indeed, some have argued that incorrect dosing parameters may contribute to the emergence of drug resistance[282].

4.2 Premise

Here, I ask the question: what is the informational value of PAE? That is, can recovery time in response to one dose of antibiotic serve as a reliable predictive metric of multi-dose efficacy? I used computational modeling to examine these questions, using the minimal intracellular models developed in the preceding chapters. These results

serve as preliminary evidence for these ideas, and could potentially form the basis for future related research directions.

4.3 Results

To investigate these questions, I expanded the models from Figure 18A: instead of characterizing single antibiotic doses by concentration and duration, periodic regimens were specified by the antibiotic concentration, A, the duration of each dose, T_1, the time between doses, T_2, and the total number of doses, n (Figure 30A). I define RT_n as the recovery time after n doses. Intuitively, a high value of RT_n would correspond to a successful treatment regimen, whereas a low value of RT_n would correspond to a treatment failure. Indeed, modeling indicated that treatment outcome was dictated by the choices of T_1 and T_2 (Figure 30B). Indeed, these results suggest that there is a boundary between treatment outcome based on these parameters. Moreover, this boundary can be influenced by the number of doses n and antibiotic concentration A (Figure 30C).

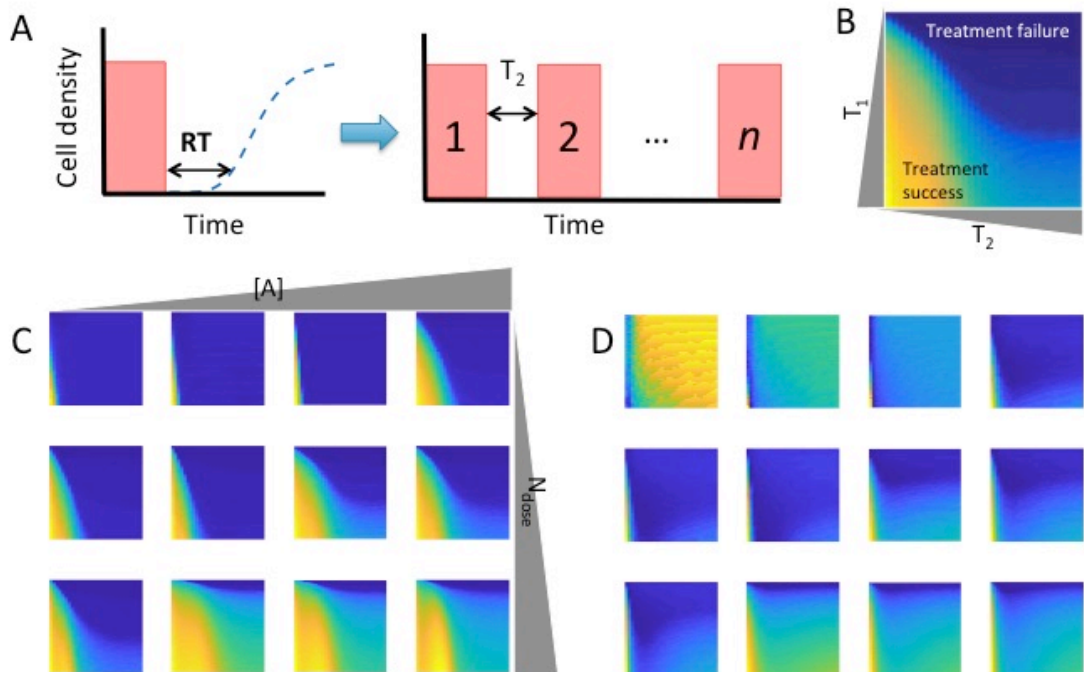

Figure 30: Recovery dynamics in response to periodic dosing. A. Periodic dosing regimens can be specified by four key parameters: the antibiotic concentration A, the dosing interval T_1, the time between doses T_2, and the total number of doses, n. I denote the recovery time following n doses as RT_n. B. Dosing parameters dictate treatment efficacy. Here, the heatmap colors indicate recovery time after $n = 3$, for each combination of T_1 and T_2; yellow corresponds to large recovery time (i.e. a successful treatment) and blue corresponds to a low recovery time (i.e. treatment failure). C.—D. The boundary between treatment efficacy and failure (as shown by the color map, is dependent on the antibiotic concentration and number of doses. Intuitively, as either of these parameters increase, the space of (T_1, T_2) over which treatment remains effective increases.

To test the predictive value of PAE, I examined the relation between the recovery time induced by one dose of antibiotic, i.e. RT_1 and the recovery time induced by n doses, i.e. RT_n. Notably, the single dose recovery time was predictive of multi-dose treatment efficacy for two of the three antibiotic motifs I tested (Figure 31). When the

drug target was subject to a positive feedback loop, any treatment which satisfied the relationship $T_2 < RT_1$ induced a significant RT_n. As soon as the inter-dose interval exceeded the recovery time induced by a single dose, treatment quickly became ineffective, as indicated by the sharp downward trend in all trajectories.

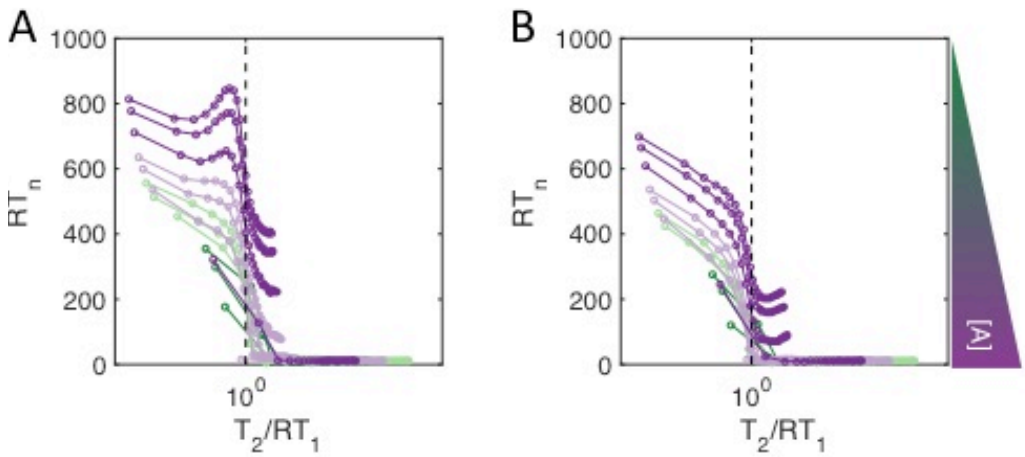

Figure 31: RT_1 predicts the efficacy of RT_n treatments. A. Here, each trajectory corresponds to one value of T_2, and colors correspond to increasing values of [A]; each data point corresponds to a single multi-dose treatment. There is a sharp transition in treatment efficacy (as measured by RT_n) at $\frac{T_2}{RT_n} = 1$; that is, the recovery time in response to a single dose corresponds to the maximum value of T_2 that results in a successful multi-dose treatment. B. As in C, but using a minimal degradation motif (FIG).

4.4 Future directions

These results suggest that PAE can be utilized to constrain the design of periodic dosing treatments; given knowledge of the relationship between recovery time and total

antibiotic delivered, one can chose a intra-dose interval such that treatment induces a significant PAE. In the future, one can imagine utilizing PAE as a fingerprint for a given antibiotic/pathogen combination; a database of these fingerprints would provide a rapid, easy way to design drug treatments on an individual basis.

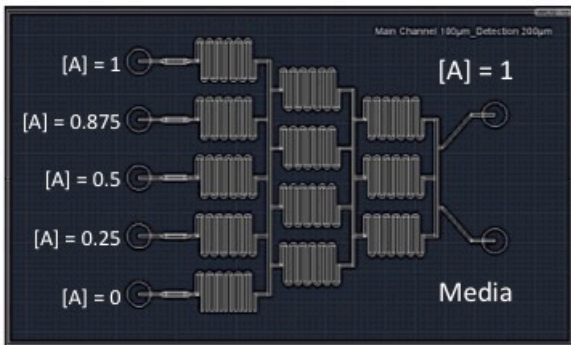

Figure 32: A proposed gradient chip design. Here, media flows from right to left, and subsequent mixing channels create a gradient of antibiotic concentration (or any other media condition of interest). This module would be placed upstream of any experimental chip and allow the user to test a wider variety of conditions without significantly increasing the amount of external hardware required.

Future studies would need to validate these conclusions in more complex and clinically relevant contexts, e.g. with isolated pathogens and a wider array of antibiotics. This presents a number of challenges: thus far, all modeling and experimental studies have assumed that populations were homogeneously susceptible to the antibiotic used. However, as noted in previous chapters, clinical infections are often multi-drug resistant and mixed. Thus, subsequent modeling needs to include the effects of population heterogeneity. Moreover, to effectively test different periodic dosing regimes, it may be

necessary to expand and increase the throughput of our microfluidic device to simultaneously test more antibiotic concentrations and/or media conditions. Figure 32 shows a potential "splitter" design (developed in collaboration with Dr. Shuqiang Huang), wherein sequential mixing channels can be used to create a concentration gradient without increasing the amount of external hardware (e.g. syringe pumps). With these improvements in both modeling and experimental approaches, future studies would be able to expand the conclusions detailed herein, and be broadly applicable to a variety of pathogens. Furthermore, these results would form the basis of a drug/pathogen reference set that may be applicable to subsequent animal models.

References

1 Meyers, M. A. *Happy accidents: Serendipity in modern medical breakthroughs*. (Arcade Pub., 2007).

2 Krafts, K., Hempelmann, E. & Skórska-Stania, A. From methylene blue to chloroquine: a brief review of the development of an antimalarial therapy. *Parasitology research* (2012).

3 Knox, W. E. The quinine-oxidizing enzyme and liver aldehyde oxidase. *Journal of Biological Chemistry* (1946).

4 Fleming, A. On the antibacterial action of cultures of a penicillium, with special reference to their use in the isolation of B. influenzae. *British journal of experimental pathology* **10**, 226 (1929).

5 KONG, K.-F., SCHNEPER, L. & MATHEE, K. Beta-lactam antibiotics: from antibiosis to resistance and bacteriology. *Apmis* **118**, 1-36, doi:10.1111/j.1600-0463.2009.02563.x.

6 Tulkens, M. & Mingeot-leclercq, M. Aminoglycosides: activity and resistance. *Antimicrob Agents …* (1999).

7 Blondeau, J. M. Fluoroquinolones: mechanism of action, classification, and development of resistance. *Survey of Ophthalmology* **49**, S73-S78, doi:10.1016/j.survophthal.2004.01.005 (2004).

8 Zaffiri, L., Gardner, J. & Toledo-Pereyra, L. H. History of Antibiotics. From Salvarsan to Cephalosporins. *Journal of Investigative Surgery* **25**, 67-77, doi:10.3109/08941939.2012.664099 (2012).

9 Sörgel, F. The Return of Ehrlich's 'Therapia magna sterilisans' and Other Ehrlich Concepts? *Chemotherapy* **50**, 6-10, doi:10.1159/000077277 (2004).

10 Overbye, K. M. & Barrett, J. F. Antibiotics: where did I go wrong? *Drug discovery today* (2005).

11 Ventola, C. L. The antibiotic resistance crisis: part 1: causes and threats. *Pharmacy and Therapeutics* (2015).

12 Clatworthy, A. E., Pierson, E. & Hung, D. T. Targeting virulence: a new paradigm for antimicrobial therapy. *Nature Chemical Biology* **3**, 541-548, doi:10.1038/nchembio.2007.24 (2007).

13 Monnet, D. L. Antibiotic development and the changing role of the pharmaceutical industry. *International Journal of Risk and Safety in Medicine* (2005).

14 Schillaci, D. The Re-Discovering of Old Molecules to face the Antibiotic Crisis. *Journal of Microbial & Biochemical Technology* **07**, doi:10.4172/1948-5948.1000e121 (2015).

15 Fishman, N. Antimicrobial stewardship. *American Journal of Infection Control* **34**, S55-S63, doi:10.1016/j.ajic.2006.05.237 (2006).
16 Davies, J. & Davies, D. Origins and evolution of antibiotic resistance. *Microbiology and Molecular Biology Reviews* **74**, 417-433 (2010).
17 Nikaido, H. Antibiotic resistance caused by gram-negative multidrug efflux pumps. *Clinical infectious diseases* (1998).
18 Llanes, C. *et al.* Clinical Strains of Pseudomonas aeruginosa Overproducing MexAB-OprM and MexXY Efflux Pumps Simultaneously. *Antimicrobial Agents and Chemotherapy* **48**, 1797-1802, doi:10.1128/AAC.48.5.1797-1802.2004 (2004).
19 Fernandez, L. & Hancock, R. E. W. Adaptive and Mutational Resistance: Role of Porins and Efflux Pumps in Drug Resistance. *Clinical Microbiology Reviews* **25**, 661-681, doi:10.1128/CMR.00043-12 (2012).
20 WRIGHT, G. Bacterial resistance to antibiotics: Enzymatic degradation and modification. *Advanced Drug Delivery Reviews* **57**, 1451-1470, doi:10.1016/j.addr.2005.04.002 (2005).
21 Levy, S. B. & Marshall, B. Antibacterial resistance worldwide: causes, challenges and responses. *Nature medicine* **10**, S122-S129 (2004).
22 Eliopoulos, G. M. & Blázquez, J. Hypermutation as a factor contributing to the acquisition of antimicrobial resistance. *Clinical infectious diseases* (2003).
23 Tuomanen, E., Durack, D. & Tomasz, A. Antibiotic tolerance among clinical isolates of bacteria. *Antimicrobial agents and chemotherapy* **30**, 521 (1986).
24 Balaban, N. Q. Bacterial Persistence as a Phenotypic Switch. *Science* **305**, 1622-1625, doi:10.1126/science.1099390 (2004).
25 Tan, C. *et al.* The inoculum effect and band-pass bacterial response to periodic antibiotic treatment. *Molecular systems biology* **8** (2012).
26 Lee, J. H. & Lee, J. Indole as an intercellular signal in microbial communities. *FEMS microbiology reviews* **34**, 426-444 (2010).
27 Hu, B., Du, J., Zou, R.-y. & Yuan, Y.-j. An environment-sensitive synthetic microbial ecosystem. *PloS one* **5** (2010).
28 Lewis, K. Persister cells, dormancy and infectious disease. *Nature Reviews Microbiology* **5**, 48-56 (2006).
29 Johnson, P. J. & Levin, B. R. Pharmacodynamics, population dynamics, and the evolution of persistence in Staphylococcus aureus. *PLoS genetics* **9**, e1003123 (2013).
30 Harms, A., Maisonneuve, E. & Gerdes, K. Mechanisms of bacterial persistence during stress and antibiotic exposure. *Science* **354**, aaf4268-aaf4268, doi:10.1126/science.aaf4268 (2016).
31 Levin, B. R. & Rozen, D. E. Non-inherited antibiotic resistance. *Nature Reviews Microbiology* **4**, 556-562 (2006).

32 Balaban, N. Q., Merrin, J., Chait, R., Kowalik, L. & Leibler, S. Bacterial persistence as a phenotypic switch. *Science* **305**, 1622-1625 (2004).
33 Tanouchi, Y., Lee, A. J., Meredith, H. & You, L. Programmed cell death in bacteria and implications for antibiotic therapy. *Trends in Microbiology* **21**, 265-270, doi:10.1016/j.tim.2013.04.001 (2013).
34 Nedelcu, A. M., Driscoll, W. W., Durand, P. M., Herron, M. D. & Rashidi, A. On the paradigm of altruistic suicide in the unicellular world. *Evolution* **65**, 3-20 (2011).
35 Thomson, K. S. & Moland, E. S. Cefepime, piperacillin-tazobactam, and the inoculum effect in tests with extended-spectrum β-lactamase-producing Enterobacteriaceae. *Antimicrobial agents and chemotherapy* **45**, 3548-3554 (2001).
36 Sykes, R. & Matthew, M. The β-lactamases of gram-negative bacteria and their role in resistance to β-lactam antibiotics. *Journal of Antimicrobial Chemotherapy* **2**, 115-157 (1976).
37 Kolodkin-Gal, I., Sat, B., Keshet, A. & Engelberg-Kulka, H. The communication factor EDF and the toxin–antitoxin module mazEF determine the mode of action of antibiotics. *PLoS biology* **6**, e319 (2008).
38 Engelberg-Kulka, H., Sat, B., Reches, M., Amitai, S. & Hazan, R. Bacterial programmed cell death systems as targets for antibiotics. *Trends in Microbiology* **12**, 66-71, doi:10.1016/j.tim.2003.12.008 (2004).
39 McGannon, C. M., Fuller, C. A. & Weiss, A. A. Different classes of antibiotics differentially influence Shiga toxin production. *Antimicrobial agents and chemotherapy* **54**, 3790-3798 (2010).
40 Plunkett, G., Rose, D. J., Durfee, T. J. & Blattner, F. R. Sequence of Shiga Toxin 2 Phage 933W fromEscherichia coli O157: H7: Shiga Toxin as a Phage Late-Gene Product. *Journal of Bacteriology* **181**, 1767-1778 (1999).
41 Lainhart, W., Stolfa, G. & Koudelka, G. B. Shiga toxin as a bacterial defense against a eukaryotic predator, Tetrahymena thermophila. *Journal of bacteriology* **191**, 5116-5122, doi:10.1128/JB.00508-09 (2009).
42 Miller, M. B. & Bassler, B. L. Quorum sensing in bacteria. *Annual Reviews in Microbiology* **55**, 165-199 (2001).
43 Hammer, B. K. & Bassler, B. L. Quorum sensing controls biofilm formation in Vibrio cholerae. *Molecular microbiology* **50**, 101-104 (2003).
44 Robicsek, A. *et al.* Fluoroquinolone-modifying enzyme: a new adaptation of a common aminoglycoside acetyltransferase. *Nature medicine* **12**, 83-88 (2005).
45 Ding, X., Baca-DeLancey, R. R. & Rather, P. N. Role of SspA in the density-dependent expression of the transcriptional activator AarP in Providencia stuartii. *FEMS microbiology letters* **196**, 25-29 (2001).
46 Pai, A., Tanouchi, Y. & You, L. Optimality and robustness in quorum sensing (QS)-mediated regulation of a costly public good enzyme. *Proceedings of the*

National Academy of Sciences **109**, 19810-19815, doi:10.1073/pnas.1211072109/-/DCSupplemental/pnas.201211072SI.pdf (2012).

47 Juhas, M., Eberl, L. & Tummler, B. Quorum sensing: the power of cooperation in the world of Pseudomonas. *Environmental Microbiology* **7**, 459-471, doi:10.1111/j.1462-2920.2005.00769.x (2005).

48 Davies, D. G. *et al.* The involvement of cell-to-cell signals in the development of a bacterial biofilm. *Science* **280**, 295-298 (1998).

49 Ishida, H. *et al.* In vitro and in vivo activities of levofloxacin against biofilm-producing Pseudomonas aeruginosa. *Antimicrobial agents and chemotherapy* **42**, 1641-1645 (1998).

50 Singh, R., Ray, P., Das, A. & Sharma, M. Penetration of antibiotics through Staphylococcus aureus and Staphylococcus epidermidis biofilms. *Journal of antimicrobial chemotherapy* **65**, 1955-1958 (2010).

51 Anderl, J. N., Franklin, M. J. & Stewart, P. S. Role of antibiotic penetration limitation in Klebsiella pneumoniae biofilm resistance to ampicillin and ciprofloxacin. *Antimicrobial agents and chemotherapy* **44**, 1818-1824 (2000).

52 Giwercman, B., Jensen, E., Høiby, N., Kharazmi, A. & Costerton, J. Induction of beta-lactamase production in Pseudomonas aeruginosa biofilm. *Antimicrobial agents and chemotherapy* **35**, 1008-1010 (1991).

53 Costerton, J., Stewart, P. S. & Greenberg, E. Bacterial biofilms: a common cause of persistent infections. *Science* **284**, 1318-1322 (1999).

54 Craig, W. A., Bhavnani, S. M. & Ambrose, P. G. The inoculum effect: Fact or artifact? *Diagnostic Microbiology and Infectious Disease* **50**, 229-230, doi:10.1016/j.diagmicrobio.2004.07.006 (2004).

55 Udekwu, K. I., Parrish, N., Ankomah, P., Baquero, F. & Levin, B. R. Functional relationship between bacterial cell density and the efficacy of antibiotics. *Journal of Antimicrobial Chemotherapy* **63**, 745-757 (2009).

56 Tadmor, A. D. & Tlusty, T. A Coarse-Grained Biophysical Model of E. coli and Its Application to Perturbation of the rRNA Operon Copy Number. *PLoS Computational Biology* **4**, e1000038, doi:10.1371/journal.pcbi.1000038.s016 (2008).

57 Thron, C. Bistable biochemical switching and the control of the events of the cell cycle. *Nonlinear Analysis: Theory, Methods & Applications* **30**, 1825-1834 (1997).

58 VanBogelen, R. A. & Neidhardt, F. C. Ribosomes as sensors of heat and cold shock in Escherichia coli. *Proceedings of the National Academy of Sciences* **87**, 5589-5593 (1990).

59 Sykes, M. T., Shajani, Z., Sperling, E., Beck, A. H. & Williamson, J. R. Quantitative Proteomic Analysis of Ribosome Assembly and Turnover< i> In Vivo</i>. *Journal of molecular biology* **403**, 331-345 (2010).

60 Rice, K. C. *et al.* The Staphylococcus aureus cidAB operon: evaluation of its role in regulation of murein hydrolase activity and penicillin tolerance. *Journal of bacteriology* **185**, 2635-2643 (2003).
61 Rice, K. C. *et al.* The cidA murein hydrolase regulator contributes to DNA release and biofilm development in Staphylococcus aureus. *Proceedings of the National Academy of Sciences* **104**, 8113-8118 (2007).
62 Bayles, K. W. The biological role of death and lysis in biofilm development. *Nature Reviews Microbiology* **5**, 721-726 (2007).
63 Groicher, K. H., Firek, B. A., Fujimoto, D. F. & Bayles, K. W. The Staphylococcus aureus lrgAB operon modulates murein hydrolase activity and penicillin tolerance. *Journal of bacteriology* **182**, 1794-1801 (2000).
64 Köhler, T., Curty, L. K., Barja, F., van Delden, C. & Pechère, J.-C. Swarming of Pseudomonas aeruginosa is dependent on cell-to-cell signaling and requires flagella and pili. *Journal of bacteriology* **182**, 5990-5996 (2000).
65 Butler, M. T., Wang, Q. & Harshey, R. M. Cell density and mobility protect swarming bacteria against antibiotics. *Proceedings of the National Academy of Sciences* **107**, 3776-3781 (2010).
66 Kim, W., Killam, T., Sood, V. & Surette, M. G. Swarm-cell differentiation in Salmonella enterica serovar Typhimurium results in elevated resistance to multiple antibiotics. *Journal of bacteriology* **185**, 3111-3117 (2003).
67 Verstraeten, N. *et al.* Living on a surface: swarming and biofilm formation. *Trends in Microbiology* **16**, 496-506, doi:10.1016/j.tim.2008.07.004 (2008).
68 van Ditmarsch, D. *et al.* Convergent evolution of hyperswarming leads to impaired biofilm formation in pathogenic bacteria. *Cell reports* **4**, 697-708 (2013).
69 Overhage, J., Bains, M., Brazas, M. D. & Hancock, R. E. Swarming of Pseudomonas aeruginosa is a complex adaptation leading to increased production of virulence factors and antibiotic resistance. *Journal of bacteriology* **190**, 2671-2679 (2008).
70 Gunn, J. S. Bacterial modification of LPS and resistance to antimicrobial peptides. *Journal of endotoxin research* **7**, 57-62 (2001).
71 Lee, H. H., Molla, M. N., Cantor, C. R. & Collins, J. J. Bacterial charity work leads to population-wide resistance. *Nature* **467**, 82-85, doi:10.1038/nature09354 (2010).
72 Andersen, J. B. *et al.* gfp-based N-acyl homoserine-lactone sensor systems for detection of bacterial communication. *Applied and environmental microbiology* **67**, 575-585 (2001).
73 Moons, P., Michiels, C. W. & Aertsen, A. Bacterial interactions in biofilms. *Critical reviews in microbiology* **35**, 157-168 (2009).
74 Allison, D. & Matthews, M. Effect of polysaccharide interactions on antibiotic susceptibility of Pseudomonas aeruginosa. *Journal of applied bacteriology* **73**, 484-488 (1992).

75 Tanouchi, Y., Pai, A., Buchler, N. E. & You, L. Programming stress-induced altruistic death in engineered bacteria. *Molecular systems biology* **8** (2012).
76 Pai, A., Tanouchi, Y. & You, L. (2012).
77 Tanouchi, Y., Pai, A., Buchler, N. E. & You, L. Programming stress-induced altruistic death in engineered bacteria. *Molecular Systems Biology* **8**, 1-11, doi:10.1038/msb.2012.57 (2012).
78 Kurioka, T., Yunou, Y., Harada, H. & Kita, E. Efficacy of antibiotic therapy for infection with Shiga-like toxin-producing Escherichia coli O157: H7 in mice with protein-calorie malnutrition. *European Journal of Clinical Microbiology and Infectious Diseases* **18**, 561-571 (1999).
79 Kumon, H., Ono, N., Iida, M. & Nickel, J. C. Combination effect of fosfomycin and ofloxacin against Pseudomonas aeruginosa growing in a biofilm. *Antimicrobial agents and chemotherapy* **39**, 1038-1044 (1995).
80 Schultz, G., Phillips, P., Yang, Q. & Stewart, P. Biofilm maturity studies indicate sharp debridement opens a time-dependent therapeutic window. *Journal of wound care* **19**, 320 (2010).
81 Jacoby, G. A. AmpC β-lactamases. *Clinical microbiology reviews* **22**, 161-182 (2009).
82 Drawz, S. M. & Bonomo, R. A. Three decades of β-lactamase inhibitors. *Clinical microbiology reviews* **23**, 160-201 (2010).
83 Chaibi, E., Sirot, D., Paul, G. & Labia, R. Inhibitor-resistant TEM β-lactamases: phenotypic, genetic and biochemical characteristics. *Journal of Antimicrobial Chemotherapy* **43**, 447-458 (1999).
84 Mutschler, H. & Meinhart, A. ε/ζ systems: their role in resistance, virulence, and their potential for antibiotic development. *Journal of molecular medicine* **89**, 1183-1194 (2011).
85 Lioy, V. S., Rey, O., Balsa, D., Pellicer, T. & Alonso, J. C. A toxin–antitoxin module as a target for antimicrobial development. *Plasmid* **63**, 31-39 (2010).
86 Berry, A. M., Lock, R. A., Hansman, D. & Paton, J. C. Contribution of autolysin to virulence of Streptococcus pneumoniae. *Infection and immunity* **57**, 2324-2330 (1989).
87 Tateda, K. *et al.* Azithromycin inhibits quorum sensing in Pseudomonas aeruginosa. *Antimicrobial agents and chemotherapy* **45**, 1930-1933 (2001).
88 Van Delden, C. *et al.* Azithromycin to prevent Pseudomonas aeruginosa ventilator-associated pneumonia by inhibition of quorum sensing: a randomized controlled trial. *Intensive care medicine* **38**, 1118-1125 (2012).
89 Dong, Y.-H., Xu, J.-L., Li, X.-Z. & Zhang, L.-H. AiiA, an enzyme that inactivates the acylhomoserine lactone quorum-sensing signal and attenuates the virulence of Erwinia carotovora. *Proceedings of the National Academy of Sciences* **97**, 3526-3531 (2000).

90 O'Loughlin, C. T. *et al.* A quorum-sensing inhibitor blocks Pseudomonas aeruginosa virulence and biofilm formation. *Proceedings of the National Academy of Sciences* **110**, 17981-17986, doi:10.1073/pnas.1316981110/-/DCSupplemental/sapp.pdf (2013).

91 Brackman, G., Cos, P., Maes, L., Nelis, H. J. & Coenye, T. Quorum sensing inhibitors increase the susceptibility of bacterial biofilms to antibiotics in vitro and in vivo. *Antimicrobial agents and chemotherapy* **55**, 2655-2661 (2011).

92 Soong, G. *et al.* Bacterial neuraminidase facilitates mucosal infection by participating in biofilm production. *The Journal of clinical investigation* **116**, 2297-2305 (2006).

93 Bjarnsholt, T. & Givskov, M. Quorum sensing inhibitory drugs as next generation antimicrobials: worth the effort? *Current Infectious Disease Reports* (2008).

94 Mehta, R. & Champney, W. S. 30S ribosomal subunit assembly is a target for inhibition by aminoglycosides in Escherichia coli. *Antimicrobial agents and chemotherapy* **46**, 1546-1549 (2002).

95 Maisonneuve, E. & Gerdes, K. Molecular Mechanisms Underlying Bacterial Persisters. *Cell* **157**, 539-548, doi:10.1016/j.cell.2014.02.050 (2014).

96 Dalebroux, Z. D., Svensson, S. L., Gaynor, E. C. & Swanson, M. S. ppGpp Conjures Bacterial Virulence. *Microbiology and Molecular Biology Reviews* **74**, 171-199, doi:10.1128/MMBR.00046-09 (2010).

97 Kohanski, M. A., Dwyer, D. J., Hayete, B., Lawrence, C. A. & Collins, J. J. A Common Mechanism of Cellular Death Induced by Bactericidal Antibiotics. *Cell* **130**, 797-810, doi:10.1016/j.cell.2007.06.049 (2007).

98 Toguchi, A., Siano, M., Burkart, M. & Harshey, R. M. Genetics of swarming motility in Salmonella enterica serovar Typhimurium: critical role for lipopolysaccharide. *Journal of bacteriology* **182**, 6308-6321 (2000).

99 Mireles, J. R., Toguchi, A. & Harshey, R. M. Salmonella enterica Serovar Typhimurium Swarming Mutants with Altered Biofilm-Forming Abilities: Surfactin Inhibits Biofilm Formation. *Journal of Bacteriology* **183**, 5848-5854, doi:10.1128/JB.183.20.5848-5854.2001 (2001).

100 Brook, I., Pazzaglia, G., Coolbaugh, J. C. & Walker, R. I. In-vivo protection of group A β-haemolytic streptococci from penicillin by β-lactamase-producing Bacteroides species. *Journal of Antimicrobial Chemotherapy* **12**, 599-606 (1983).

101 Citorik, R. J., Mimee, M. & Lu, T. K. Sequence-specific antimicrobials using efficiently delivered RNA-guided nucleases. *Nature biotechnology*, 1141-1145 (2014).

102 Bikard, D. *et al.* Exploiting CRISPR-Cas nucleases to produce sequence-specific antimicrobials. *Nature biotechnology*, 1146-1150 (2014).

103 Eagle, H. & Musselman, A. D. The rate of bactericidal action of penicillin in vitro as a function of its concentration, and its paradoxically reduced activity at high concentrations against certain organisms. *The Journal of experimental medicine* **88**, 99-131 (1948).

104 Hentzer, M. *et al.* Attenuation of Pseudomonas aeruginosa virulence by quorum sensing inhibitors. *The EMBO journal* **22**, 3803-3815 (2003).

105 Hentzer, M. & Givskov, M. Pharmacological inhibition of quorum sensing for the treatment of chronic bacterial infections. *Journal of Clinical Investigation* **112**, 1300-1307 (2003).

106 Köhler, T., Perron, G. G., Buckling, A. & Van Delden, C. Quorum sensing inhibition selects for virulence and cooperation in Pseudomonas aeruginosa. *PLoS pathogens* **6**, e1000883 (2010).

107 Nalca, Y. *et al.* Quorum-sensing antagonistic activities of azithromycin in Pseudomonas aeruginosa PAO1: a global approach. *Antimicrobial agents and chemotherapy* **50**, 1680-1688 (2006).

108 Schuster, M., Joseph Sexton, D., Diggle, S. P. & Peter Greenberg, E. Acyl-homoserine lactone quorum sensing: from evolution to application. *Annual review of microbiology* **67**, 43-63 (2013).

109 Sandoz, K. M., Mitzimberg, S. M. & Schuster, M. Social cheating in Pseudomonas aeruginosa quorum sensing. *Proceedings of the National Academy of Sciences* **104**, 15876-15881 (2007).

110 André, J. B. & Godelle, B. Multicellular organization in bacteria as a target for drug therapy. *Ecology Letters* **8**, 800-810 (2005).

111 Dandekar, A. A., Chugani, S. & Greenberg, E. P. Bacterial quorum sensing and metabolic incentives to cooperate. *Science* **338**, 264-266 (2012).

112 Chuang, J. S., Rivoire, O. & Leibler, S. Simpson's paradox in a synthetic microbial system. *Science* **323**, 272-275 (2009).

113 Tanouchi, Y., Smith, R. P. & You, L. Engineering microbial systems to explore ecological and evolutionary dynamics. *Current opinion in biotechnology* **23**, 791-797 (2012).

114 Darch, S. E., West, S. A., Winzer, K. & Diggle, S. P. Density-dependent fitness benefits in quorum-sensing bacterial populations. *Proceedings of the National Academy of Sciences* **109**, 8259-8263 (2012).

115 Yurtsev, E. A., Chao, H. X., Datta, M. S., Artemova, T. & Gore, J. Bacterial cheating drives the population dynamics of cooperative antibiotic resistance plasmids. *Molecular systems biology* **9** (2013).

116 Allen, R. C., Popat, R., Diggle, S. P. & Brown, S. P. Targeting virulence: can I make evolution-proof drugs? *Nature Reviews Microbiology* **12**, 300-308, doi:10.1038/nrmicro3232 (2014).

117 Kitano, H. Systems Biology: A Brief Overview. *Science* **295**, 1662-1664, doi:10.1126/science.1069492 (2002).
118 Stelling, J. Mathematical models in microbial systems biology. *Current Opinion in Microbiology* **7**, 513-518, doi:10.1016/j.mib.2004.08.004 (2004).
119 Jorgensen, J. H. & Turnidge, J. D. in *Manual of Clinical Microbiology, Eleventh Edition* 1253-1273 (American Society of Microbiology, 2015).
120 Szita, N., Polizzi, K., Jaccard, N. & Baganz, F. Microfluidic approaches for systems and synthetic biology. *Current Opinion in Biotechnology* **21**, 517-523, doi:10.1016/j.copbio.2010.08.002 (2010).
121 Hamon, M. & Hong, J. W. New tools and new biology: Recent miniaturized systems for molecular and cellular biology. *Molecules and Cells* **36**, 485-506, doi:10.1007/s10059-013-0333-1 (2013).
122 Wang, P. *et al.* Robust Growth of Escherichia coli. *Current Biology* **20**, 1099-1103, doi:10.1016/j.cub.2010.04.045 (2010).
123 Tanouchi, Y. *et al.* A noisy linear map underlies oscillations in cell size and gene expression in bacteria. *Nature* **523**, 357-360, doi:10.1038/nature14562 (2015).
124 Cira, N. J., Ho, J. Y., Dueck, M. E. & Weibel, D. B. A self-loading microfluidic device for determining the minimum inhibitory concentration of antibiotics. *Lab on a Chip* **12**, 1052-1059, doi:10.1039/C2LC20887C (2012).
125 Kaminski, T. S., Churski, K. & Garstecki, P. in *Microdroplet Technology* 117-136 (Springer, 2012).
126 Sun, P. *et al.* High-throughput microfluidic system for long-term bacterial colony monitoring and antibiotic testing in zero-flow environments. *Biosensors and Bioelectronics* **26**, 1993-1999, doi:10.1016/j.bios.2010.08.062 (2011).
127 Huang, S. *et al.* Dynamic control and quantification of bacterial population dynamics in droplets. *Biomaterials* **61**, 239-245, doi:10.1016/j.biomaterials.2015.05.038 (2015).
128 Cooperman, E. M. Antibiotics: no panacea. *Canadian Medical Association Journal* (1977).
129 Walters, M. C., Roe, F., Bugnicourt, A., Franklin, M. J. & Stewart, P. S. Contributions of Antibiotic Penetration, Oxygen Limitation, and Low Metabolic Activity to Tolerance of Pseudomonas aeruginosa Biofilms to Ciprofloxacin and Tobramycin. *Antimicrobial Agents and Chemotherapy* **47**, 317-323, doi:10.1128/AAC.47.1.317-323.2003 (2003).
130 Lewis, K. Persister cells, dormancy and infectious disease. *Nature Reviews Microbiology* **5**, 48-56, doi:10.1038/nrmicro1557 (2007).
131 Elhani, D. L'émergence de la résistance aux antibiotiques annonce-t-elle le retour des âges sombres? *Annales de Biologie Clinique*, doi:10.1684/abc.2011.0632 (2011).

132 Bigger, J. W. Treatment of staphylococcal infections with penicillin by intermittent sterilisation. *The Lancet* **244**, 497-500 (1944).
133 Parker, R. F. & Marsh, H. C. Action of penicillin on Staphylococcus. *Journal of Bacteriology* (1946).
134 Eagle, H. The recovery of bacteria from the toxic effects of penicillin. *Journal of Clinical Investigation* (1949).
135 Eagle, H. & Fleischman, R. The bactericidal action of penicillin in vivo: the participation of the host, and the slow recovery of the surviving organisms. *Annals of internal …* (1950).
136 Zhanel, G. G. & Craig, W. A. Pharmacokinetic contributions to postantibiotic effects. *Clinical pharmacokinetics* (1994).
137 Hanberger, H., Nilsson, L. E. & Kihlström, E. Postantibiotic effect of beta-lactam antibiotics on Escherichia coli evaluated by bioluminescence assay of bacterial ATP. *Antimicrobial agents …* (1990).
138 Odenholt-Tornqvist, I. & Löwdin, E. Pharmacodynamic effects of subinhibitory concentrations of beta-lactam antibiotics in vitro. *Antimicrobial Agents and …* (1991).
139 Athamna, A. In vitro post-antibiotic effect of fluoroquinolones, macrolides, -lactams, tetracyclines, vancomycin, clindamycin, linezolid, chloramphenicol, quinupristin/dalfopristin and rifampicin on Bacillus anthracis. *Journal of Antimicrobial Chemotherapy* **53**, 609-615, doi:10.1093/jac/dkh130 (2004).
140 Mizunaga, S. Influence of inoculum size of Staphylococcus aureus and Pseudomonas aeruginosa on in vitro activities and in vivo efficacy of fluoroquinolones and carbapenems. *Journal of Antimicrobial Chemotherapy* **56**, 91-96, doi:10.1093/jac/dki163 (2005).
141 Zhanel, G. G. & Hoban, D. J. The postantibiotic effect: a review of in vitro and in vivo data. *Annals of …* (1991).
142 Odenholt-Tornqvist, I. Studies on the postantibiotic effect and the postantibiotic sub-MIC effect of meropenem. *Journal of Antimicrobial …* (1993).
143 Bundtzen, R. W., Gerber, A. U. & Cohn, D. L. Postantibiotic suppression of bacterial growth. *Review of Infectious …* (1981).
144 Eagle, H. & Musselman, A. D. The slow recovery of bacteria from the toxic effects of penicillin. *Journal of Bacteriology* (1949).
145 Eagle, H., Fleischman, R. & Musselman, A. D. Effect of schedule of administration on the therapeutic efficacy of penicillin: importance of the aggregate time penicillin remains at effectively bactericidal levels. *The American journal of medicine* (1950).
146 Gudmundsson, S. & Einarsson, S. The post-antibiotic effect of antimicrobial combinations in a neutropenic murine thigh infection model. *Journal of …* (1993).

147 Craig, W. A. Post-antibiotic effects in experimental infection models: relationship to in-vitro phenomena and to treatment of infections in man. *Journal of Antimicrobial Chemotherapy* (1993).
148 AliAbadi, F. S. & Lees, P. Antibiotic treatment for animals: effect on bacterial population and dosage regimen optimisation. *International Journal of Antimicrobial Agents* (2000).
149 Dethlefsen, L. & Relman, D. A. in *Proceedings of the National …* (2011).
150 Dethlefsen, L., Huse, S., Sogin, M. L. & Relman, D. A. The Pervasive Effects of an Antibiotic on the Human Gut Microbiota, as Revealed by Deep 16S rRNA Sequencing. *PLoS Biology* **6**, e280, doi:10.1371/journal.pbio.0060280.sd008 (2008).
151 Perez-Cobas, A. E. *et al.* Gut microbiota disturbance during antibiotic therapy: a multi-omic approach. *Gut* **62**, 1591-1601, doi:10.1136/gutjnl-2012-303184 (2013).
152 Tenney, J. H. & Maack, R. W. Rapid selection of organisms with increasing resistance on subinhibitory concentrations of norfloxacin in agar. *Antimicrobial Agents and …* (1983).
153 Gullberg, E. *et al.* Selection of Resistant Bacteria at Very Low Antibiotic Concentrations. *PLoS Pathogens* **7**, e1002158, doi:10.1371/journal.ppat.1002158.s003 (2011).
154 Beam, T. R., Gilbert, D. N. & Kunin, C. M. General guidelines for the clinical evaluation of anti-infective drug products. *Clinical infectious diseases* (1992).
155 Craig, W. A. & Vogelman, B. The postantibiotic effect. *Annals of Internal Medicine* (1987).
156 Li, R. C., Lee, S. W. & Kong, C. H. Correlation between bactericidal activity and postantibiotic effect for five antibiotics with different mechanisms of action. *Journal of Antimicrobial …* (1997).
157 MacKenzie, F. M. & Gould, I. M. The post-antibiotic effect. **32**, 519-537 (1993).
158 zur Wiesch, P. A., Abel, S. & Gkotzis, S. Classic reaction kinetics can explain complex patterns of antibiotic action. *Science translational …* (2015).
159 Stubbings, W. Mechanisms of the post-antibiotic effects induced by rifampicin and gentamicin in Escherichia coli. *Journal of Antimicrobial Chemotherapy* **58**, 444-448, doi:10.1093/jac/dkl225 (2006).
160 Tan, C. *et al.* The inoculum effect and band-pass bacterial response to periodic antibiotic treatment. **8**, 1-11, doi:10.1038/msb.2012.49 (2012).
161 Lopatkin, A. J. *et al.* Antibiotics as a selective driver for conjugation dynamics. *Nature Microbiology*, 1-8, doi:10.1038/nmicrobiol.2016.44 (2016).
162 Grenier, F., Matteau, D., Baby, V. & Rodrigue, S. Complete Genome Sequence of Escherichia coli BW25113. *Genome Announcements* **2**, e01038-01014-e01038-01014, doi:10.1128/genomeA.01038-14 (2014).

163 Wiuff, C. *et al.* Phenotypic Tolerance: Antibiotic Enrichment of Noninherited Resistance in Bacterial Populations. *Antimicrobial Agents and Chemotherapy* **49**, 1483-1494, doi:10.1128/AAC.49.4.1483-1494.2005 (2005).

164 MUIR, M. E. & van HEESWYCK, R. S. Effect of growth rate on streptomycin accumulation by Escherichia coli and Bacillus megaterium. *Journal of general …* (1984).

165 Neidhardt, F. C. *Escherichia coli and Salmonella : cellular and molecular biology*. (ASM Press, 1996).

166 Edmunds, T. & Goldberg, A. L. Role of ATP hydrolysis in the degradation of proteins by protease La from Escherichia coli. *Journal of cellular biochemistry* (1986).

167 Kaplan, R. & Apirion, D. The fate of ribosomes in Escherichia coli cells starved for a carbon source. *Journal of Biological Chemistry* (1975).

168 Zundel, M. A., Basturea, G. N. & Deutscher, M. P. Initiation of ribosome degradation during starvation in Escherichia coli. *RNA* **15**, 977-983, doi:10.1261/rna.1381309 (2009).

169 Damper, P. D. & Epstein, W. Role of the membrane potential in bacterial resistance to aminoglycoside antibiotics. *Antimicrobial Agents and Chemotherapy* (1981).

170 Hancock, R. Uptake of 14G-Streptomycin by Bacillus megaterium. *Journal of General Microbiology* (1962).

171 Hurwitz, C. & Rosano, C. L. Accumulation of label from C14-streptomycin by Escherichia coli. *Journal of Bacteriology* (1962).

172 Bryan, L. E. & Van Den Elzen, H. M. Streptomycin accumulation in susceptible and resistant strains of Escherichia coli and Pseudomonas aeruginosa. *Antimicrobial Agents and …* (1976).

173 Paixão, L. *et al.* Fluorometric determination of ethidium bromide efflux kinetics in Escherichia coli. *Journal of Biological Engineering* **3**, 18, doi:10.1186/1754-1611-3-18 (2009).

174 Viveiros, M. *et al.* Demonstration of intrinsic efflux activity of Escherichia coli K-12 AG100 by an automated ethidium bromide method. *International Journal of Antimicrobial Agents* **31**, 458-462, doi:10.1016/j.ijantimicag.2007.12.015 (2008).

175 Kinoshita, N., Unemoto, T. & Kobayashi, H. Proton motive force is not obligatory for growth of Escherichia coli. *Journal of Bacteriology* (1984).

176 Singh, M., Jadaun, G. & Srivastava, K. Effect of efflux pump inhibitors on drug susceptibility of ofloxacin resistant Mycobacterium tuberculosis isolates. *The Indian journal of …* (2011).

177 Cohen, S. P., Hooper, D. C. & Wolfson, J. S. Endogenous active efflux of norfloxacin in susceptible Escherichia coli. *Antimicrobial agents …* (1988).

178 Lazzarini, R. A. & Dahlberg, A. E. The control of ribonucleic acid synthesis during amino acid deprivation in Escherichia coli. *Journal of Biological Chemistry* (1971).
179 Spivey, J. The postantibiotic effect. *Clinical pharmacy* **11**, 865-875 (1992).
180 Talpaert, M. J., Gopal Rao, G., Cooper, B. S. & Wade, P. in *Journal of Antimicrobial Chemotherapy* Vol. 66 2168-2174 (2011).
181 Marquez, B. in *Biochimie* Vol. 87 1137-1147 (2005).
182 Askoura, M., Mattawa, W., Abujamel, T. & Taher, I. in *Libyan Journal of Medicine* Vol. 6 5870 (2017).
183 Nikaido, H. in *Science* Vol. 264 382-388 (American Association for the Advancement of Science, 1994).
184 Ma, D., Cook, D. N., Hearst, J. E. & Nikaido, H. Efflux pumps and drug resistance in gram-negative bacteria. *Trends in Microbiology* **2**, 489-493 (1994).
185 Mcmurry, L. M. & Oethinger, M. in *FEMS microbiology …* (1998).
186 Okusu, H., Ma, D. & Nikaido, H. in *Journal of Bacteriology* (1996).
187 Kriengkauykiat, J., Porter, E., Lomovskaya, O. & Wong-Beringer, A. in *Antimicrobial Agents and Chemotherapy* Vol. 49 565-570 (2005).
188 Amaral, L., Engi, H., Viveiros, M. & Molnar, J. Comparison of multidrug resistant efflux pumps of cancer and bacterial cells with respect to the same inhibitory agents. *In vivo* (2007).
189 Stavri, M., Piddock, L. J. V. & Gibbons, S. in *Journal of Antimicrobial Chemotherapy* Vol. 59 1247-1260 (2007).
190 Mahamoud, A., Chevalier, J., Alibert-Franco, S., Kern, W. V. & Pages, J. M. in *Journal of Antimicrobial Chemotherapy* Vol. 59 1223-1229 (2007).
191 Poole, K. & Lomovskaya, O. in *Drug Discovery Today: Therapeutic Strategies* Vol. 3 145-152 (2006).
192 Opperman, T. J. & Nguyen, S. T. in *Front. Microbio.* Vol. 6 11086 (2015).
193 Van Bambeke, F. & Lee, V. J. in *Recent patents on anti-infective …* (2006).
194 Lomovskaya, O. & Bostian, K. A. in *Biochemical Pharmacology* Vol. 71 910-918 (2006).
195 Andreu, N. *et al.* Optimisation of Bioluminescent Reporters for Use with Mycobacteria. *PLoS ONE* **5**, e10777, doi:10.1371/journal.pone.0010777.t005 (2010).
196 Prosser, J., Killham, K., Glover, L. & Rattray, E. Luminescence-based systems for detection of bacteria in the environment. *Critical reviews in biotechnology* **16**, 157-183 (1996).
197 Kaki, R. *et al.* in *Journal of Antimicrobial Chemotherapy* Vol. 66 1223-1230 (2011).
198 Ferrell, J., James E. Self-perpetuating states in signal transduction: positive feedback, double-negative feedback and bistability. *Current Opinion in Cell Biology* **14**, 140-148, doi:10.1016/S0955-0674(02)00314-9 (2002).

199 Buchler, N. E. & Cross, F. R. Protein sequestration generates a flexible ultrasensitive response in a genetic network. *Molecular Systems Biology* **5** (2009).
200 Arkin, A., Ross, J. & McAdams, H. H. Stochastic kinetic analysis of developmental pathway bifurcation in phage λ-infected Escherichia coli cells. *Genetics* **149**, 1633 (1998).
201 Huang, C.-Y. & Ferrell, J. E. Ultrasensitivity in the mitogen-activated protein kinase cascade. *Proceedings of the National Academy of Sciences* **93**, 10078-10083 (1996).
202 Markevich, N. I. Signaling switches and bistability arising from multisite phosphorylation in protein kinase cascades. *The Journal of cell biology* **164**, 353-359, doi:10.1083/jcb.200308060 (2004).
203 Gillespie, D. T. Exact stochastic simulation of coupled chemical reactions. *The journal of physical chemistry* **81**, 2340-2361 (1977).
204 Schmidt, B. A. & Horsley, V. Intradermal adipocytes mediate fibroblast recruitment during skin wound healing. *Development* **140**, 1517-1527 (2013).
205 Süel, G. M., Garcia-Ojalvo, J., Liberman, L. M. & Elowitz, M. B. An excitable gene regulatory circuit induces transient cellular differentiation. *Nature Cell Biology* **440**, 545-550, doi:10.1038/nature04588 (2006).
206 Menke, N. B. *et al.* An in silico approach to the analysis of acute wound healing. *Wound Repair and Regeneration* **18**, 105-113 (2010).
207 Iwano, M. *et al.* Evidence that fibroblasts derive from epithelium during tissue fibrosis. *Journal of Clinical Investigation* **110**, 341-350 (2002).
208 Shi-wen, X. *et al.* Focal adhesion kinase and reactive oxygen species contribute to the persistent fibrotic phenotype of lesional scleroderma fibroblasts. *Rheumatology* **51**, 2146-2154 (2012).
209 Smits, W. K., Kuipers, O. P. & Veening, J.-W. Phenotypic variation in bacteria: the role of feedback regulation. *Nature Reviews Microbiology* **4**, 259-271, doi:10.1038/nrmicro1381 (2006).
210 van Sinderen, D. & Venema, G. Comk Acts as an Autoregulatory Control Switch in the Signal-Transduction Route to Competence in Bacillus-Subtilis. *Journal of Bacteriology* **176**, 5762-5770 (1994).
211 Veening, J.-W., Hamoen, L. W. & Kuipers, O. P. Phosphatases modulate the bistable sporulation gene expression pattern in Bacillus subtilis. *Molecular Microbiology* **56**, 1481-1494, doi:10.1111/j.1365-2958.2005.04659.x (2005).
212 Hautefort, I., Proenca, M. J. & Hinton, J. C. D. Single-Copy Green Fluorescent Protein Gene Fusions Allow Accurate Measurement of Salmonella Gene Expression In Vitro and during Infection of Mammalian Cells. *Applied and Environmental Microbiology* **69**, 7480-7491, doi:10.1128/AEM.69.12.7480-7491.2003 (2003).

213 Saini, S., Ellermeier, J. R., Slauch, J. M. & Rao, C. V. The Role of Coupled Positive Feedback in the Expression of the SPI1 Type Three Secretion System in Salmonella. *PLoS Pathogens* **6**, e1001025, doi:10.1371/journal.ppat.1001025.s007 (2010).

214 Diaz. Intrinsic and extrinsic regulation of type III secretion gene expression in Pseudomonas aeruginosa. *Frontiers in Microbiology*, doi:10.3389/fmicb.2011.00089 (2011).

215 Zeng, Q. *et al.* Cell Individuality: The Bistable Gene Expression of the Type III Secretion System in Dickeya dadantii 3937. *Molecular Plant-Microbe Interactions* **25**, 37-47 (2012).

216 Galán, J. E. & Collmer, A. Type III secretion machines: bacterial devices for protein delivery into host cells. *Science* **284**, 1322-1328, doi:10.1126/science.284.5418.1322 (1999).

217 Hapfelmeier, S. & Hardt, W.-D. A mouse model for S. typhimurium-induced enterocolitis. *Trends in Microbiology* **13**, 497-503, doi:10.1016/j.tim.2005.08.008 (2005).

218 Sturm, A. *et al.* The Cost of Virulence: Retarded Growth of Salmonella Typhimurium Cells Expressing Type III Secretion System 1. *PLoS Pathogens* **7**, e1002143, doi:10.1371/journal.ppat.1002143.s011 (2011).

219 Diard, M. *et al.* Stabilization of cooperative virulence by the expression of an avirulent phenotype. *Nature* **494**, 353-356, doi:10.1038/nature11913 (2014).

220 Rice, K. C. & Bayles, K. W. Death's toolbox: examining the molecular components of bacterial programmed cell death. *Molecular Microbiology* **50**, 729-738, doi:10.1046/j.1365-2958.2003.03720.x (2003).

221 Ackermann, M. *et al.* Self-destructive cooperation mediated by phenotypic noise. *Nature* **454**, 987-990, doi:10.1038/nature07067 (2008).

222 Elowitz, M. B., Levine, A. J., Siggia, E. D. & Swain, P. S. Stochastic gene expression in a single cell. *Science*, doi:10.1126/science.1073263 (2002).

223 Fraser, D. & Kaern, M. A chance at survival: gene expression noise and phenotypic diversification strategies. *Molecular Microbiology* **71**, 1333-1340, doi:10.1111/j.1365-2958.2009.06605.x (2009).

224 de Jong, I. G., Haccou, P. & Kuipers, O. P. Bet hedging or not? A guide to proper classification of microbial survival strategies. *BioEssays* **33**, 215-223, doi:10.1002/bies.201000127 (2011).

225 Veening, J.-W. *et al.* Bet-hedging and epigenetic inheritance in bacterial cell development. *Proceedings of the National Academy of Sciences* **105**, 4393-4398 (2008).

226 Beaumont, H. J. E., Gallie, J., Kost, C., Ferguson, G. C. & Rainey, P. B. Experimental evolution of bet hedging *Nature* **461**, 90-93, doi:10.1038/nature08504 (2009).

227 Waite, A. J. *et al.* Non-genetic diversity modulates population performance. *Molecular Systems Biology* **12**, 895, doi:10.15252/msb.20167044 (2016).
228 Gillespie, J. H. Natural selection for within-generation variance in offspring number. *Genetics* (1974).
229 Hamilton, W. D. The evolution of altruistic behavior. *The American Naturalist* (1963).
230 McNamara, J. M. & Houston, A. I. State-dependent life histories. *Nature* (1996).
231 Kramers, H. A. Brownian motion in a field of force and the diffusion model of chemical reactions. *Physica* **7**, 284-304 (1940).
232 Zhou, T., Moss, F. & Jung, P. Escape-time distributions of a periodically modulated bistable system with noise. *Physical Review A* **42**, 3161 (1990).
233 Choi, M. H., Fox, R. F. & Jung, P. Quantifying stochastic resonance in bistable systems: Response vs residence-time distribution functions. *Physical review E* **57**, 6335 (1998).
234 Jung, P. Thermal activation in bistable systems under external periodic forces. *Zeitschrift für Physik B Condensed Matter* **76**, 521-535 (1989).
235 Gardner, T. S., Cantor, C. R. & Collins, J. J. Construction of a genetic toggle switch inEscherichia coli. *Nature* **403**, 339-342 (2000).
236 Varghese, J. & Cohen, S. M. microRNA miR-14 acts to modulate a positive autoregulatory loop controlling steroid hormone signaling in Drosophila. *Genes and Development* **21**, 2277-2282, doi:10.1101/gad.439807 (2007).
237 Arvanitis, D. N., Jungas, T., Behar, A. & Davy, A. Ephrin-B1 Reverse Signaling Controls a Posttranscriptional Feedback Mechanism via miR-124. *Molecular and cellular biology* **30**, 2508-2517, doi:10.1128/MCB.01620-09 (2010).
238 Kramer, B. P. *et al.* An engineered epigenetic transgene switch in mammalian cells. *Nature Biotechnology* **22**, 867-870, doi:10.1038/nbt980 (2004).
239 Greber, D., El-Baba, M. D. & Fussenegger, M. Intronically encoded siRNAs improve dynamic range of mammalian gene regulation systems and toggle switch. *Nucleic acids research* **36**, e101-e101, doi:10.1093/nar/gkn443 (2008).
240 Deans, T. L., Cantor, C. R. & Collins, J. J. A Tunable Genetic Switch Based on RNAi and Repressor Proteins for Regulating Gene Expression in Mammalian Cells. *Cell* **130**, 363-372, doi:10.1016/j.cell.2007.05.045 (2007).
241 Munsky, B. & Khammash, M. Identification from stochastic cell-to-cell variation: a genetic switch case study. *IET Systems Biology* **4**, 356-366, doi:10.1049/iet-syb.2010.0013 (2010).
242 Nevins, J. R. E2F: a link between the Rb tumor suppressor protein and viral oncoproteins. *Science* **258**, 424-429 (1992).
243 Nevins, J. R. Toward an understanding of the functional complexity of the E2F and retinoblastoma families. *Cell Growth and Differentiation* **9**, 585-593 (1998).

244 Yao, G., Lee, T. J., Mori, S., Nevins, J. R. & You, L. A bistable Rb–E2F switch underlies the restriction point. *Nature cell biology* **10**, 476-482, doi:10.1038/ncb1711 (2008).

245 Yao, G., Tan, C., West, M., Nevins, J. R. & You, L. Origin of bistability underlying mammalian cell cycle entry. *Molecular Systems Biology* **7**, 1-10, doi:10.1038/msb.2011.19 (2011).

246 Wong, J. V., Yao, G., Nevins, J. R. & You, L. Viral-mediated noisy gene expression reveals biphasic E2f1 response to MYC. *Molecular cell* **41**, 275-285 (2011).

247 Lee, T. J., Yao, G., Bennett, D. C., Nevins, J. R. & You, L. Stochastic E2F activation and reconciliation of phenomenological cell-cycle models. *PLoS Biology* **8**, e1000488 (2010).

248 Nevins, J. R. E2f - a Link Between the Rb Tumor Suppressor Protein and Viral Oncoproteins. *Science* **258**, 424-429 (1992).

249 Chellappan, S. P., Hiebert, S., Mudryj, M., Horowitz, J. M. & Nevins, J. R. The E2f Transcription Factor Is a Cellular Target for the Rb Protein. *Cell* **65**, 1053-1061 (1991).

250 Nevins, J. R. The Rb/E2F pathway and cancer. *Human Molecular Genetics* **10**, 699-703 (2001).

251 Jung, H., Hsiung, B., Pestal, K., Procyk, E. & Raulet, D. H. RAE-1 ligands for the NKG2D receptor are regulated by E2F transcription factors, which control cell cycle entry. *Journal of Experimental Medicine* **209**, 2409-2422 (2012).

252 Molenaar, J. J. *et al.* Copy number defects of G1-Cell cycle genes in neuroblastoma are frequent and correlate with high expression of E2F target genes and a poor prognosis. *Genes, Chromosomes, and Cancer* **51**, 10-19 (2012).

253 Nevozhay, D., Adams, R. M., Murphy, K. F., Josić, K. & Balázsi, G. Negative autoregulation linearizes the dose–response and suppresses the heterogeneity of gene expression. *Proceedings of the National Academy of Sciences* **106**, 5123-5128 (2009).

254 Cohen, D. Optimizing reproduction in a randomly varying environment. *Journal of Theoretical Biology* **12**, 119-129 (1966).

255 Schaffer, W. M. Optimal reproductive effort in fluctuating environments. *American Naturalist*, 783-790 (1974).

256 Acar, M., Mettetal, J. T. & van Oudenaarden, A. Stochastic switching as a survival strategy in fluctuating environments. *Nature Genetics* **40**, 471-475, doi:10.1038/ng.110 (2008).

257 Thattai, M. & van Oudenaarden, A. Stochastic gene expression in fluctuating environments. *Genetics* **167**, 523-530 (2004).

258 Rosenberg, E., Keller, K. H. & Dworkin, M. Cell density-dependent growth of Myxococcus xanthus on casein. *Journal of Bacteriology* **129**, 770-777 (1977).

259 Contois, D. E. Kinetics of bacterial growth: relationship between population density and specific growth rate of continuous cultures. *Journal of General Microbiology* **21**, 40-50 (1959).
260 Cai, L., Dalal, C. K. & Elowitz, M. B. Frequency-modulated nuclear localization bursts coordinate gene regulation. *Nature* **455**, 485-490 (2008).
261 Ashall, L. *et al.* Pulsatile stimulation determines timing and specificity of NF-κB-dependent transcription. *Science* **324**, 242-246 (2009).
262 Miskov-Zivanov, N., Turner, M. S., Kane, L. P., Morel, P. A. & Faeder, J. R. The Duration of T Cell Stimulation Is a Critical Determinant of Cell Fate and Plasticity. *Science Signaling* **6**, ra97-ra97, doi:10.1126/scisignal.2004217 (2013).
263 Levine, J. H., Lin, Y. & Elowitz, M. B. Functional Roles of Pulsing in Genetic Circuits. *Science* **342**, 1193-1200, doi:10.1126/science.1239999 (2013).
264 Josefowicz, S. Z., Lu, L.-F. & Rudensky, A. Y. Regulatory T cells: mechanisms of differentiation and function. *Annual review of immunology* **30**, 531-564 (2012).
265 Gomez-Rodriguez, J. *et al.* Itk-mediated integration of T cell receptor and cytokine signaling regulates the balance between Th17 and regulatory T cells. *The Journal of experimental medicine* **211**, 529-543 (2014).
266 Pace, V., Bellizzi, D., Giordano, F., Panno, M. L. & Benedictis, G. Experimental testing of a mathematical model relevant to the extrinsic pathway of apoptosis. *Cell Stress and Chaperones* **15**, 13-23, doi:10.1007/s12192-009-0118-9 (2009).
267 Gillespie, D. T. The chemical Langevin equation. *The Journal of Chemical Physics* **113**, 297 (2000).
268 Powell, S. H. *et al.* Once-daily vs. continuous aminoglycoside dosing: efficacy and toxicity in animal and clinical studies of gentamicin, netilmicin, and tobramycin. *Journal of Infectious Diseases* **147**, 918-932 (1983).
269 Avent, M. L., Rogers, B. A., Cheng, A. C. & Paterson, D. L. in *Internal Medicine Journal* Vol. 41 441-449 (2011).
270 Paladino, J. A. in *American journal of health-system pharmacy* (2000).
271 Avorn, J., Soumerai, S. B. & Taylor, W. in *Archives of …* (1988).
272 Glynn, C. M. & Azadian, B. in *Current Anaesthesia & Critical Care* Vol. 16 221-230 (2005).
273 Harbarth, S., Samore, M. H., Lichtenberg, D. & Carmeli, Y. Prolonged Antibiotic Prophylaxis After Cardiovascular Surgery and Its Effect on Surgical Site Infections and Antimicrobial Resistance. *Circulation* **101**, 2916-2921, doi:10.1161/01.CIR.101.25.2916 (2000).
274 Pena-Miller, R. *et al.* in *PLoS Biol* Vol. 11 e1001540 (2013).
275 Slama, T. G. in *Critical Care* (2008).
276 Ventola, C. L. in *Pharmacy and Therapeutics* (2015).
277 Andes, D. & Craig, W. A. in *International Journal of Antimicrobial Agents* (2002).

278 Frimodt-Møller, N. How predictive is PK/PD for antibacterial agents? *International Journal of Antimicrobial Agents* (2002).

279 Scaglione, F. in *International Journal of Antimicrobial Agents* (2002).

280 A Roberts, J. Using PK/PD to optimize antibiotic dosing for critically ill patients. *Current pharmaceutical biotechnology* **12**, 2070-2079 (2011).

281 Liu, P., Müller, M. & Derendorf, H. in *International Journal of Antimicrobial Agents* (2002).

282 Toutain, P. L., del Castillo, J. R. E. & Bousquet-Mélou, A. in *Research in Veterinary Science* Vol. 73 105-114 (2002).

Biography

Jaydeep K Srimani was born in Carbondale, IL, on 21 August 1989. He grew up in Ft. Collins, Colorado and Clemson, South Carolina. He was first exposed to research in high school, when he participated in an REU program in Chemical Engineering at Clemson University. He graduated from DW Daniel High School in 2007 and studied Computer Engineering (with a minor in Biomedical Engineering) as a President's Scholar at the Georgia Institute of Technology in Atlanta, GA. As an undergraduate student, he spent two years working in Prof. May D. Wang's lab (Biomedical Engineering), where he was awarded a President's Undergraduate Research Award, and a Barry M. Goldwater Scholarship for work on web-based tools for distributed genome analysis.

After graduating with highest honors in 2011, he joined the Laboratory of Biological Networks in the Department of Biomedical Engineering at Duke University, under the supervision of Dr. Lingchong You. He was awarded a NIH Kirschstein Predoctoral Fellowship from the Duke Center for Biomolecular and Tissue Engineering in his 2nd year. During his time in graduate school, he completed an internship in the Scientific Computing division at Amyris Biotechnologies in Emeryville, CA under the direction of Dr. Amoolya Singh. His research interests include non-genetic mechanisms of antibiotic resistance and stochastic modeling of biological networks.